TUDelft

Delft University of Technology

Lateral Flows and Sediment Dynamics in a Large Engineered Estuary

Zhou, Z.

DOI
10.4233/uuid:cc6848ff-ee93-4af8-a322-5b27d354da7f

Publication date
2021

Document Version
Final published version

Citation (APA)
Zhou, Z. (2021). *Lateral Flows and Sediment Dynamics in a Large Engineered Estuary*. [Dissertation (TU Delft), Delft University of Technology]. https://doi.org/10.4233/uuid:cc6848ff-ee93-4af8-a322-5b27d354da7f

Important note
To cite this publication, please use the final published version (if applicable).
Please check the document version above.

Lateral Flows and Sediment Dynamics in a Large Engineered Estuary

Lateral Flows and Sediment Dynamics in a Large Engineered Estuary

Dissertation

for the purpose of obtaining the degree of doctor
at Delft University of Technology
by the authority of the Rector Magnificus Prof.dr.ir. T.H.J.J. van der Hagen
chair of the Board for Doctorates
to be defended publicly on
Wednesday, 1 December 2021 at 10:00 o'clock

by

Zaiyang ZHOU

Bachelor of Science in Port Channel and Coastal Engineering,
Ocean University of China, China
born in Yangzhou, China

This dissertation has been approved by the promotors.

Composition of the doctoral committee:

Rector Magnificus,	chairperson
Prof.dr.ir. Z.B. Wang	Delft University of Technology, promotor
Prof.dr. P.X. Ding	East China Normal University, promotor
Prof.dr. D.S. van Maren	East China Normal University, promotor

Independent members:

Dr.ir. B.C. van Prooijen	Delft University of Technology
Prof.dr. M.G. Kleinhans	Utrecht University
Prof.dr. Q. He	East China Normal University
Prof.dr.ir. H.J. de Vriend	Delft University of Technology
Prof.dr.ir. J.C. Winterwerp	Delft University of Technology, reserve member

Prof.dr. Jianzhong Ge of East China Normal University has contributed greatly to the preparation of this dissertation by providing effective guidance, constructive suggestions, and observational data.

The doctoral research has been carried out in the context of an agreement on joint doctoral supervision between East China Normal University, China and Delft University of Technology, the Netherlands.

To my family

Contents

Summary

Estuaries are partially enclosed water bodies where river water mixes with sea water. Estuaries provide important ecological functions which are strongly regulated by estuarine hydrodynamics and sediment dynamics, and also by human interventions. Sustainable management of such systems therefore requires a thorough understanding of the interplay between hydrodynamics, sediment dynamics, and human interventions. However, estuaries are often complex systems influenced by river runoff and coastal hydrodynamics (tide, wind, and wave), which all interact with human interventions on various time and spatial scales. Our understanding of estuaries is still insufficient to understand the response of strongly engineered systems to both human interventions and to natural fluctuations.

Many estuaries worldwide are strongly influenced by a wide range of human interventions, including engineering constructions, deepening, and land reclamations. An example of highly engineered estuaries is the Changjiang Estuary (CE), China. The upstream river discharge and sediment load is strongly influenced by the Three Gorges Dam (TGD), a multi-purpose dam in the Changjiang River aiming at optimizing flood control and irrigation, and generate hydropower. In the North Passage (NP), an outlet and the main navigation channel of the CE, the Deepwater Navigation Channel (DNC) has been constructed to improve channel navigability. The DNC project includes constructions of dikes and groynes, and regular dredging work. These various interventions strongly influence estuarine hydro- and sediment dynamics but take place concurrently, and therefore their individual impact is not straightforward to assess. A better understanding of the impact of these interventions requires systematic analysis of hydrodynamic and sediment transport processes in relation to the interventions.

This dissertation aims to unravel the effect of groynes on lateral flows and sediment transport in a tidal channel-shoal system (i.e. the NP). Groyne fields provide buffer zones, with a salinity lagging behind that in the main navigation channel. The resulting lateral salinity gradients drive lateral density currents, which in turn modify longitudinal salinity gradients in the main channel. These salinity-driven currents also impact the lateral sediment exchange between the main channel and the groyne fields. The effects of groynes on lateral flows and lateral sediment exchange are analyzed using numerical simulations in combination with in-situ observations.

Water-bed sediment exchange processes are investigated in more detail using measurements collected with two tripods deployed in the CE. Measured bed level changes are analyzed by semi-automatically fitting the Krone-Partheniades equations to the bed level data using observations of velocity and sediment concentration. This method provides continuous timeseries of sediment properties related to erosion and deposition. It is demonstrated that the erosion parameters are strongly fluctuating, and not constant as typically assumed in numerical models. Such a

variability needs to be reflected in a model, either by time-varying parameters or including more detailed processes (for example, consolidation). This dissertation introduces a method to obtain a parameter space that includes the values and accuracies of all potential combinations of input parameters, which is important input for morphodynamic models.

To further quantify effects of groynes on hydrodynamics and sediment dynamics, an idealized hydrodynamic model with a single channel with groynes is developed and analyzed. The idealized system has geometric features comparable to the NP, but is set up in such a way that the groyne field aspect ratios (the ratio of the distance between contiguous groynes to the length of groynes) can be systematically investigated. Model results reveal that groynes can influence channel hydrodynamics and local mixing conditions, which influence lateral flows and the longitudinal salt intrusion. Salt intrusion is highest for intermediate aspect ratios, but weaker for very wide or narrow groyne fields. These results highlight the complexity of the hydrodynamics in salt fresh-water transition zones, and specifically the role of human intervention thereon.

Samenvatting

Estuaria zijn deels omsloten waterlichamen waar zoetwater aangevoerd vanuit rivieren mengt met zout zeewater. Estuaria bieden belangrijke ecosysteemdiensten welke sterk beïnvloed worden door de estuariene waterbeweging en sediment transport, maar ook door menselijke ingrepen. Duurzaam beheer van zulke systemen vereist daardoor een grondige kennis van de relatie tussen de waterbeweging, het sediment transport, en deze menselijke ingrepen. Estuaria zijn echter complexe systemen beïnvloed door de rivierafvoer en mariene processen (getij, wind, golven) welke allemaal interacteren met menselijke ingrepen op variërende tijd- en ruimteschalen. Als gevolg hiervan wordt de invloed van menselijke ingrepen in dergelijke estuaria nog onvoldoende begrepen.

Veel estuaria wereldwijd worden sterk beïnvloed door een scala aan menselijke ingrepen, zoals waterbouwkundige constructies, geulverdiepingen, en landaanwinningswerken. Een voorbeeld van een dergelijk estuarium is het Changjiang estuarium (CE) in China. De bovenstroomse rivierafvoer en sedimenttoevoer wordt sterk beïnvloed door de Drie Gorges Dam (TGD), een multifunctioneel reservoir in de Changjiang Rivier gericht op het optimaliseren van irrigatie, mitigeren van overstromingen, en opwekken van elektriciteit. Om de bevaarbaarheid in de North Passage (NP, een van de mondingsgeulen en de belangrijkste vaarweg van de CE) te verbeteren is een vaargeulverbeteringsproject (bestaande uit dijken, kribben en vaargeulverdiepingen) uitgevoerd. De verschillende ingrepen vinden grotendeels gelijktijdig plaats, en daarom is het moeilijk om de individuele bijdrage van deze ingrepen vast te stellen. Een beter begrip van deze ingrepen vereist een systematische studie van de hydrodynamische en sedimenttransport processen in relatie tot verschillende menselijke ingrepen.

De doelstelling van dit proefschrift is om het effect van kribben op dwarsstroming en sedimenttransport in een plaat-geulsysteem (de NP) te kwantificeren. Kribvakken vormen een bufferzone, waarin het zoutgehalte achterloopt op dat in de hoofdgeul. De resulterende zoutgradiënten in de dwarsrichting drijven dwarsstromingen aan, welke op haar beurt zoutgradiënten langs de vaargeul beïnvloeden. Deze zoutgedreven dwarsstromingen beïnvloeden ook de sedimentuitwisseling tussen kribvakken en de vaargeul. Het effect van kribben op dwarsstroming en sedimentuitwisseling in de dwarsrichting worden geanalyseerd met behulp van een numeriek model in combinatie met in situ metingen.

De sedimentuitwisseling tussen bodem en waterkolom wordt in meer detail onderzocht met behulp van metingen verkregen met twee meetframes ingezet in de CE. Gemeten bodemveranderingen worden geanalyseerd door de Krone-Partheniades vergelijkingen semi-automatisch aan te passen aan de bodemdata, gebruik makend van gemeten stroomsnelheden en sedimentconcentraties. Deze methode levert continue tijdsseries van sediment eigenschappen gerelateerd aan

xiii

erosie en depositie. Hiermee wordt aangetoond dat erosie parameters sterk fluctueren en niet constant zijn, zoals vaak voor numerieke modelstudies wordt aangenomen. Een dergelijke variabiliteit zou in een numeriek model verdisconteerd moeten worden, door ofwel tijdsafhankelijke erosieparameters of door het implementeren van complexere processen (zoals bijvoorbeeld consolidatie). Deze dissertatie introduceert een methodiek om een groot aantal parameterinstellingen te verkrijgen met daarin de waarde en nauwkeurigheid van alle mogelijke combinaties van invoerparameters, wat belangrijke invoer is voor numerieke modellen.

Om het effect van kribben op de waterbeweging en sedimentdynamiek in meer detail te kwantificeren, is een geïdealiseerd waterbewegingsmodel van een geul met kribben opgezet en toegepast. Dit geïdealiseerde systeem is qua dimensies en stroming vergelijkbaar met de NP, maar is dusdanig opgezet dat de kribvakverhouding (de ratio van de afstand tussen kribben en de lengte van kribben) systematisch onderzocht kan worden. Modelresultaten laten zien dat kribben een groot effect hebben op de waterbeweging in de geul en lokale menging, en daarmee de dwarsstroming en de zoutindringing. Zoutindringing is maximaal voor gemiddelde kribvakverhoudingen, en zwakker voor relatief grote of juist kleine afstanden tussen de kribben. Deze resultaten illustreren de complexiteit van de waterbeweging in zout-zoet overgangen en in het bijzonder het effect van menselijk ingrepen hierop.

摘要

河口是部分封闭的、存在咸淡水混合的水体。河口具有重要的生态功能，这些功能受到河口水动力、泥沙动力、以及人类活动干预的强烈影响。因此，实现河口区域的可持续发展及有效管理，需要对水动力、泥沙动力、与人类活动影响之间的相互作用有深刻的理解。然而，河口通常又是极为复杂的系统，它受到径流、海岸动力（风、浪、潮）的影响，二者都与人类活动存在不同时间、空间尺度上的相互作用。其中，对于受工程结构重要影响的系统而言，关于其对人类活动与自然要素变化的响应，我们还没有充分的认识。

世界范围内许多河口都受到人类活动的一系列重要影响，包括工程结构建设、航道疏浚、土地围垦等。中国的长江河口就是一个高度工程化河口的示例。长江河口上游建有三峡工程，包含一座集优化洪峰控制、灌溉、发电等目的为一体的大坝，对长江河口的水沙通量产生了显著影响。北槽作为长江河口的重要入海口及主要通航水道，其内实施了深水航道工程以提高通航能力。深水航道工程包括导堤、丁坝的建设以及泥沙疏浚工作。诸如此类的人类干预深刻影响着河口的水沙动力条件，并且这些影响是同时产生的，难以对其进行单独评估。想要更好地理解这些人类活动的影响需要对人类活动干预下的水动力与泥沙输运过程进行系统分析。

本研究旨在揭示丁坝对滩槽系统内侧向流及泥沙输运的影响。坝田区域可以提供一个缓冲区，使得其中的盐度与主槽中的盐度相比具有潮周期内的相位差。由此产生的滩

槽之间的盐度梯度，可能驱动侧向流，产生盐度的侧向交换，并可能进一步改变主槽内纵向上的盐度梯度。由盐度梯度驱动的侧向流对滩槽间的泥沙交换也会产生影响。本文采用数值模型与现场观测相结合的方法对上述影响进行分析。

通过对长江河口内两组由三脚架系统所观测的数据进行分析，本研究还对床面与水体间的泥沙交换过程进行探究。使用实测的流速与悬浮泥沙浓度数据，将实测的床面数据与 Krone-Partheniades 侵蚀淤积模型进行半自动化拟合。该方法能得到泥沙沉降、侵蚀过程中主要参数的连续时间序列。研究表明泥沙的侵蚀参数是显著波动的，区别于通常在数值模型中所采用的常数参数设定。这样的变化性需要在模型中有所体现，通过采用时变参数或引入更精细的过程，例如床面固结模型。本文也提供了一种获取常数参数空间（包含所有潜在的常数参数集及其精确度）的方法。

为了进一步量化丁坝对水沙动力的影响，本文建立了一个单一汉道、具有导堤丁坝结构的理想化模型进行分析。该理想化模型系统有着与北槽相当的空间尺度与地形特征，但同时，该模型的设定具备对丁坝布置的纵横比（相邻丁坝间距与丁坝长度之间的比值）进行系统性研究的特征。模型结果显示，丁坝能够显著影响航道内水动力条件与局地垂向混合强度，并进一步影响径流方向上的盐水入侵程度。中等纵横比的丁坝布局下，盐水入侵最为显著，极大或极小纵横比情况下的盐水入侵较弱。这些结果强调了在河口这一特定的咸淡水交汇区域，水动力的复杂性，以及在此基础上人类活动所产生的多方面重要影响。

1

Introduction

1

1.1. Background

1.1.1. Importance of Estuaries and the Changjiang Estuary

Estuaries, where rivers meet the ocean, are of great importance for human beings. Most of the largest cities are located along estuaries [Ross, 1995]. The typical brackish water in estuaries provide a nursery environment for a vast array of species. As natural habitats for a suite of plants and animals, estuaries have great ecological, economic, and environmental values. Estuaries are affected by multiple dynamics, such as flushing fresh water from the riverine environments and tidal propagation of salt water from the marine environments. The resulting hydrodynamic complexity in combination with its great economic value has triggered broad scientific interest in estuaries.

The Changjiang Estuary (CE, also Yangtze River Estuary) is a mega-scale, river-and-tide-controlled estuary, which connects the Changjiang River with the East China Sea. The Changjiang River is the longest river in China, and the third longest river in the world. During the wet season, the river discharge of this $\sim$ 6300-km long river is up to 70,000 m^3/s. Abundant sediment is carried downstream and distributed over the four outlets of the CE. The annual sediment load was up to 400 million tons before the construction of the Three Gorges Dam (TGD). After closing the TGD, a dramatic decline of sediment load has been observed, reducing the annual mean sediment load to about 140 million tons [Yang *et al.*, 2015]. This large change due to human interventions has been affecting sediment dynamics, morphodynamics, and regulation policies (e.g. follow-up engineering projects and the dredging strategy).

1.1.2. The North Passage: An Artificially Intervened Channel-Shoal System

The CE has four outlets, among which the North Passage (NP) is the main navigation channel. Although the sediment load of the Changjiang River has obviously decreased since the closing of the TGD (as introduced in the previous section), the NP is located within the estuary turbidity maximum (ETM) of the CE and has a very high near-bed suspended sediment concentration (SSC, up to tens of g/L) in the form of concentrated benthic suspension (CBS) [Ge *et al.*, 2018; Lin *et al.*, 2021]. As a result, siltation rates in the NP are very high, which negatively impacts the navigability of the channel. To alleviate this problem, the Deepwater Navigation Channel (DNC) project has been developed. The DNC project contains three phases from 1998 to 2010 [Hu and Ding, 2009], including the construction of 2 dikes and 19 groynes in the NP, as well as capital dredging. The project deepens the NP from about 7 m to 12.5 m, resulting in regular maintenance dredging work of about 75 million $m^3/year$.

The DNC project provides a 12.5 m deep channel (about 350 - 400 m in width). Meanwhile, groynes shelter the shoal areas on both sides and the dredging work does not cover groyne fields, forming a channel-shoal system in the NP. Note that this channel-shoal system is not natural, differing from natural channel shoal systems because (1) its formation is tightly related to human interventions, and (2)

the shoal areas are continuously affected by groynes. Therefore, knowledge about natural channel-shoal systems needs to be extended for such an artificially intervened system. More detailed information on the DNC project is presented in section 3.2.1.

1.2. Objectives and Research Questions

The CE has attracted lots of research interest due to its complexity and economic importance. Mechanisms related to the development of the CE are important for understanding other systems around the world as well, particularly heavily engineered turbid systems. In order to advance our understanding of such heavily engineered, high concentration estuaries, there is a need to better understand the relation between density-driven flows, sediment dynamics, human interventions (particularly groyne fields) and channel siltation.

The aim of this dissertation therefore is:

To quantify salt and sediment dynamics in a heavily engineered estuary, and identify the effect of groynes thereon.

This aim is pursued with the following scientific questions, which form the core of this dissertation:

(1) How do lateral processes contribute to salt and sediment exchange between the main channel and shoal areas in a tidal channel-shoal system?

(2) What is the temporal variability in water-bed exchange processes, and (how) can this variability be parameterized?

(3) How does the impact of groynes in estuarine environments differ from barotropic equivalents, and how do they influence salt intrusion?

These questions are briefly explained as follows.

1.2.1. Lateral Flow and Channel-Shoal Sediment Exchange

Scientific studies on estuaries with channel-shoal systems strongly focus on longitudinal processes such as tidal propagation, estuarine circulation, and salt intrusion. These processes are all important for understanding estuarine dynamics, but insufficient to cover all aspects. For example, the sediment exchange between a main channel and shoal areas influences sediment (re)-distribution and siltation in the navigation channel, and is strongly influenced by lateral processes. Unlike riverine and coastal environments which have fresh water and salt water respectively, estuarine environments are featured by salinity gradients. These salinity gradients drive transverse density currents which complicate channel-shoal exchange processes. Meanwhile, geometric characteristics of the system (for example, bathymetry, channel curvature), tidal dynamics (including interactions with

1

seasonally-varying river discharge), and engineering structures jointly result in spatial and temporal differences of lateral flows and sediment transport.

In this thesis, we combine in-situ observations and numerical models to investigate lateral flows and lateral sediment transport, expecting to provide supplementary information on channel-shoal mass exchange and in particular extend our knowledge about engineering-intervened physical processes in estuaries.

1.2.2. Erosion and Deposition of Sediment

Channel siltation is the result of vertical sediment exchange between the water column and the sediment bed. On the short term, this is crucial for channel navigability and dredging strategies, and on the long term also drives the morphological evolution (including progradation of tidal flats, regime shifts, etc.). Moreover, water-bed exchange is also highly relevant for biological processes and there is an increasing amount of biogeomorphological research [Stallins, 2006; Haussmann, 2011; Naylor, 2005; Van Prooijen et al., 2011].

Water-bed exchange processes are composed of a sediment deposition flux and a sediment erosion flux. The classic Krone-Partheniades framework provides a methodology for quantifying these fluxes and calculating the bed level change. This theoretical framework (including several adaptations, see Ariathurai [1974]; Krone et al. [1962]; Partheniades [1965]; Winterwerp and van Kesteren [2004]) has been applied for nearly 50 years to quantify geomorphic processes. However, there are still some aspects of the sediment exchange processes which remain unclear (for example, whether there should be a critical shear stress for deposition). At the same time, data-based methodologies to derive the input parameters for this framework are very time-consuming and inconsistent (requiring a range of instruments covering different time periods). Therefore, we conducted in-situ observations in the North Passage (2017) and the South Passage (2018), aiming to better understand the erosion and deposition processes in the CE, and improve the usability of the Krone-Partheniades model by optimizing the parameterization process.

1.2.3. Application of Groynes in Estuarine Environments

As introduced in previous sections, estuarine environments have salinity gradients and this characteristic also brings differences from engineering aspect compared to environments without salinity gradients. For example, lateral flows are greatly affected by groynes in estuaries [Zhou et al., 2019, 2021]. Groynes are widely applied to regulate flow velocity and enhance channel navigability (in riverine environments) and protect shorelines (in coastal areas). Scientific research has, however, only addressed the role of groynes in these coastal and riverine environments. However, salinity gradients lead to specific effects of groynes, such as the retention of salt water and the resulting density-driven lateral flows between the main channel and groyne fields. Therefore, knowledge about the effect of groynes and design characteristics (length, width) needs to be extended.

For an estuary with multiple outlets like the CE, it should be noted that large engineering project (for example, the DNC project) can influence the dynamic balance between multiple outlets. Groynes may therefore have both (1) direct and

1

local effects on channel hydrodynamics and (2) broader effects on the whole estuary. These two kinds of effects interact and the interactions hamper a complete understanding of their individual contributions. To focus on the impact of groynes within a particular channel (and exclude the effect of flow distribution over multiple outlets), an idealized single-channel model is developed and applied to understand the effects of groynes on channel hydrodynamics, lateral exchange, and salt intrusion.

1.3. Dissertation Organization

The three research questions are addressed in Chapter 2 - 5. The first question is addressed in two chapters: lateral flows in Chapter 2 and lateral sediment transport in Chapter 3. The content of the various chapters is summarized as follows:

In Chapter 2, results from near-bottom observations with a tripod-system in 2016 are analyzed. A process-based hydrodynamic model is developed to explain the observed intratidal salinity variation and lateral flows in the NP.

In Chapter 3, the hydrodynamic model used in Chapter 2 is extended into a suspended sediment model, to further investigate lateral sediment transport in the NP and quantify effects of groynes on sediment exchange between the main channel and the groyne fields.

In Chapter 4, water-bed exchange is analyzed using two data sets. One was collected in the NP in 2017 and the other was collected in the South Passage in 2018, both with a tripod system. By analyzing these observational data and reproducing the observed bed level changes with the Krone-Partheniades framework, water-bed dynamics and parameter calibration are discussed.

In Chapter 5, an idealized hydrodynamic model is developed to investigate effects of groynes on channel hydrodynamics and lateral flows between the main channel and the groyne fields. By comparisons between numerical simulations, what should be aware of in applicating groynes in estuarine environments is discussed.

Chapter 6 summarizes the work in this thesis with general conclusions, a synthesis and recommendations for further research.

2

Study of Lateral Flow in a Stratified Tidal Channel-Shoal System

Abstract

Lateral flow significantly contributes to the near-bottom mass transport of salinity in a channel-shoal system. In this study, an integrated tripod system was deployed in the transition zone of a channel-shoal system of the Changjiang Estuary (CE), China, to observe the near-bottom physics with high temporal/spatial resolution, particularly focusing on the lateral-flow-induced mass transport. These in-situ observations revealed a small-scale salinity fluctuation around low water slack during moderate and spring tidal conditions. A simultaneous strong lateral current was also observed, which was responsible for this small-scale fluctuation. A high-resolution unstructured-grid Finite-Volume Community Ocean Model (FVCOM) has been applied for the CE to better understand the mechanism of this lateral flow and its impact on salinity transport. The model results indicate that a significant southward near-bed shoal-to-channel current is generated by the salinity-driven baroclinic pressure gradient. This lateral current affects the salinity transport pattern and the residual current in the cross-channel direction. Cross-channel residual current shows a two-layer structure in the vertical, especially in the intermediate tide when the lateral flow notably occurred. Both observation and model results indicate that near-bottom residual transport of water moved consistently southward (shoal to channel). Mechanisms for this intra-tidal salinity variation (ISV) and its implications can be extended to other estuaries with similar channel-shoal features.

2.1. Introduction

As transition zones between riverine and marine environments, estuaries experience a wide range of physical, chemical and biological processes, e.g. suspended material transport, chemical reaction of dissolved ions, variation of biological productivity. These processes influence not only ecology but also have socio-economic impacts because many large cities are located in the vicinity of estuaries [Woodroffe *et al.*, 2006].

Salinity is a significant driver for sediment trapping, e.g. sediment accumulation at the front of salt wedge where the convergence of fresh and saline water occurs [Postma, 1967]. The upstream limit of salt intrusion is an indicator for location of estuary turbidity maximum [Dyer, 1986], the dynamics of which in itself strongly influences the navigability. Moreover, salinity also has an effect on ecology, e.g. its impact on temporal distribution of planktons [Dube *et al.*, 2010].

The long-term, large-scale salt balance is primarily the result of landward transport by estuarine circulation and tidal dispersion [Bowen, 2003; Fischer, 1976] balancing seaward transport by riverine residual flow. These salt transport mechanisms depend on the longitudinal salinity gradient and (in combination with hydrodynamic mixing) give rise to vertical salinity gradients. Vertical salinity gradients may cause salinity stratification which controls the intensity of momentum exchanges from the surface to the bottom [Simpson *et al.*, 1990].

In addition to these longitudinal and vertical processes, lateral processes in estuaries also have effects on mass transport. Cross-channel (lateral) currents are relatively small (about 10% in magnitude) compared to the along-channel currents [Lerczak and Rockwell Geyer, 2004]. However, their influences on dynamics of estuaries may be significant by generating considerable cross-channel gradients in salt, turbidity and other constituents.

Lerczak and Rockwell Geyer [2004] set up a model for an idealized straight estuary. Their results suggest that lateral circulation is stronger during flood tides than ebb tides. This asymmetry is caused by the interaction between lateral circulation, stratification and differential advection by along-channel tidal currents. The flood-ebb asymmetry of lateral flow patterns may lead to an asymmetric cross-sectional shape of a straight channel. However, in a channel which already is asymmetrically shaped, lateral flow will also be affected by bathymetric features, as well as hydraulic structures. Huijts *et al.* [2006] studied the mechanisms for lateral sediment entrapment using an idealized model. They examined mechanisms that could lead to the sediment accumulation, including Coriolis forcing and lateral density gradients. They found that because of the difference of along-channel flow velocity from bed to surface, the intensity of the Coriolis deflection varies from bed to surface. Therefore, vertical circulation in the lateral direction can be induced by the Coriolis deflection. Fugate *et al.* [2007] conducted an observation in upper Chesapeake Bay, USA, focusing on the impact of lateral dynamics on sediment transport. Using a lateral momentum balance, they observed that stronger cross-channel circulation by rotational effects (Coriolis and channel curvature) is larger during the ebb. A modelling study by Zhu *et al.* [2018] in a strongly anthropogenically impacted estuary (the Changjiang Estuary) suggest that lateral circulations are strong near the

main navigation channel, and peak close to slack tide conditions. This has great implications for siltation rates in the channel, in which more than 80 million m3/year (by 2011) needs to be dredged annually [Wang et al., 2015]. This fuels a great interest in the dynamics of lateral flows in general, but in the CE in particular.

Cross-sectional flows influence the salinity, leading to an intra-tidal salinity variation (ISV). Many studies have identified the salinity's response to the longitudinal and vertical process [Dyer, 1986; Bowen, 2003; Simpson et al., 1990; Chen and de Swart, 2018]. However, few observations directly relate salinity fluctuations to lateral flows. Yet, salinity variations may provide an indicator for lateral flows, which is much easier to measure than transverse flows themselves. The objective of this study is to detect evidence for lateral flow using a combination of flow velocity and salinity observations, and quantitatively analyze and explain their driving mechanisms and effects. This paper is organized as follows. Section 2 introduces the study area, methods for observation and data analysis, and the numerical model. Section 3 presents the main results of observations and simulations, focusing on formation of ISV and the mechanism for the lateral flow. Section 4 gives discussion on momentum balance, stratification and mixing, effects of dikes and groynes and the implication of ISV. Main conclusions are summarized in section 5.

2.2. Study Site, Observational Methods and Numerical Model

2.2.1. Study Site

Field observations were carried out in one of the four outlets of the CE (Figure 2.1). The discharge of the Changjiang River, measured at the Datong Gauging Station, is approximately 40,000 m^3/s in wet season, about 10,000 m^3/s in dry season. The mean and maximum tidal ranges are approximately 2.7 m and 4.6 m, respectively, measured at Zhongjun Gauging Station.

The CE is characterized as a channel-shoal system with multiple outlets and shallow shoals. The South Channel (SC), North Passage (NP) and South Passage (SP) are the major tidal channels in the turbidity maximum zone of the CE. The NP is deepened and protected, resulting in the so-called Deepwater Navigation Channel (DNC), aiming at improving the shipping capacity in and out of the CE. The protection works include two 50 km long dikes parallel to the flow, to which 19 groynes perpendicular to the flow are attached (Figure 2.1).

The estuarine turbidity maximum of the CE is located in the North Passage (NP), resulting in strong sedimentation rates [Ge et al., 2018, 2015; Liu et al., 2011]. Many groynes have been buried since the construction of the DNC. This has led to shallow shoals in the groyne region and a deeper main channel in the middle of the NP, forming a typical channel-shoal system. Cross-channel flows have been observed in the NP through observational and numerical studies [Zhu et al., 2018; Liu et al., 2011]. The NP is also the main mixing front of freshwater and saline water, resulting in strong horizontal salinity gradient and vertical stratification [Ge et al., 2018, 2012; Wu et al., 2012].
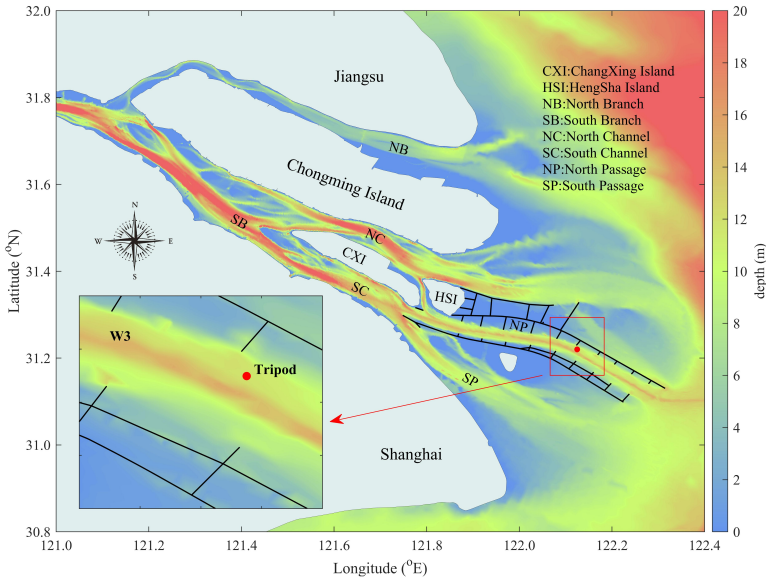
Figure 2.1: Bathymetry of the Changjiang Estuary and adjacent regions. The black lines in the river mouth indicate dikes and groynes around the North Passage. The red dot indicates the measuring site. W3 is the bending corner of the main channel.

2.2.2. Observation Methods

The middle section of the NP, located in the center of the turbidity maximum, was selected to conduct our observations (red rectangle in Figure 2.1). A tripod system was deployed on the north side of the main channel, an area with pronounced saltwater intrusion and a strongly stratified water column [Ge *et al.*, 2018]. The observation site was in the middle of the shallow shoal and the main channel to observe lateral flows between the shoal and the deep channel.

The tripod system was designed to measure flow velocity and direction, salinity, suspended sediment concentration and temperature near the bottom. To achieve this goal, the tripod integrated multiple instruments (Figure 2.2). An upward-looking 600 kHz RDI Acoustic Doppler Current Profilers (ADCP-up) was mounted 1.2 m above the sea bed (abbreviated as 'mab') with a resolution of 0.5 m for each cell. A downward-looking 1200 kHz RDI ADCP (ADCP-down) was placed 1.03 mab to measure velocities from 0.2 to 0.7 mab at high resolution (0.1 m) near the bed. Based on earlier observations [Liu *et al.*, 2011], the ADCP with 1200 kHz sensor frequency works well in the near-bottom area under typical high sediment concentration for this area. A Nortek Acoustic Doppler Vector was mounted at 0.4 mab to measure the near-bed current velocities at a sampling frequency of 16 Hz, which means valid data were collected at the height of about 0.25 mab. The tripod system also included a Point Current Meter (ALEC, JFE ALEC CO., LTD, JAPAN) at 1.45 mab to obtain flow velocities in the blanking range of ADCP-up, a Tide/wave Logger (RBR, RBR Ltd., Canada) at 1.0 mab to record wave conditions and a Conductivity,

2
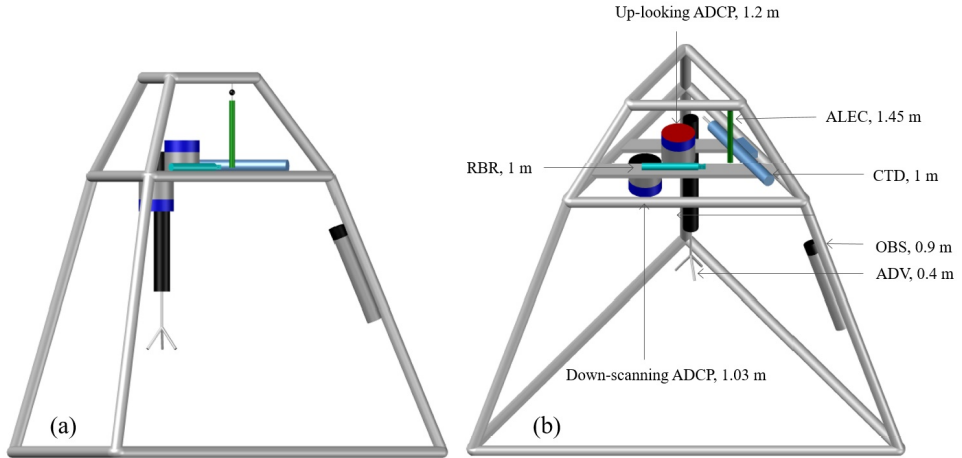
Figure 2.2: Side-view and top-view of the tripod system.

Temperature, and Pressure Recorder (CTD, Sea-Bird Electronics, Inc., USA) at 1.0 mab to record temperature and salinity continuously. An Optical Backscattering Sensor (OBS, D&A Instruments CO, type: 3A, USA) was also fixed to the side edge of the tripod. Detailed configurations of instruments installed on the tripod such as burst interval, sampling duration and sampling frequency are listed in Table 1.

Table 1: Instruments mounted on the tripod and their sampling configurations.

Instrument deployed	Distance above bed (m)	Sampling interval (min)	Sampling configuration	Survey parameter
ADCP-up	1.2	/	120 s	Profile velocity
ADCP-down	1.03 (down)	/	120 s	Profile velocity
ADV	0.25	10	16 Hz (every first 70 s)	Near-bed velocity
RBR	1	10	4 Hz	Wave conditions
ALEC	1.45	2	0.2 Hz (every first 50 s)	Velocity
OBS	0.9	/	100 s	Salinity, temperature, turbidity, and pressure
CTD	1	/	120 s	Salinity, temperature, and pressure

The tripod was deployed on December 6, 2016 (abbreviated as 12/06), in the dry season of the year. The observations lasted for about 12 days, and the tripod was recovered on 12/18, 2016. The 12 days covered a whole period from the neap tide to the spring tide. The neap tide was from 12/07 to 12/09, and the spring tide was on 12/14 - 12/16.

2.2.3. Numerical Model

To resolve the irregular geometries of the channel, shoals and submerged/exposed dikes and groynes, a hydrodynamic numerical model based on the Finite-Volume Community Ocean Model has been applied for the CE (CE-FVCOM). FVCOM is a three-dimensional, unstructured-grid coastal ocean model. This model uses a tri-angle mesh in horizontal directions and a terrain-following sigma-coordinate system with 20 uniform sigma layers in the vertical. Previous observations showed that the water column in the NP is occasionally strongly salinity stratified, and opposite flows form a two-layer flow structure in the vertical [Ge *et al.*, 2018, 2013]. As a mode split model, the adjustment between 3-D internal mode and 2-D external mode could be problematic for capturing this two-layer flow structure [Lai *et al.*, 2010]. Therefore, we use a semi-implicit scheme which is capable of well simulating the two-layer-structure flows.

The geographically unstructured mesh of FVCOM covers the whole CE as well as the inner shelf of the East China Sea, Hangzhou Bay, and Zhoushan Archipelago (Figure 2.3). Different from the original mesh configuration [Ge *et al.*, 2012, 2013], the river boundary in this model is extended to ~600 km upstream Datong Gauging Station to better resolve the river-estuary interaction (Figure 2.3a). It provides flexible resolution from the open boundary in the inner shelf to channels and shoals at the river mouth. The horizontal resolution of this model is down to ~200 m in the channel (Figure 2.3b).
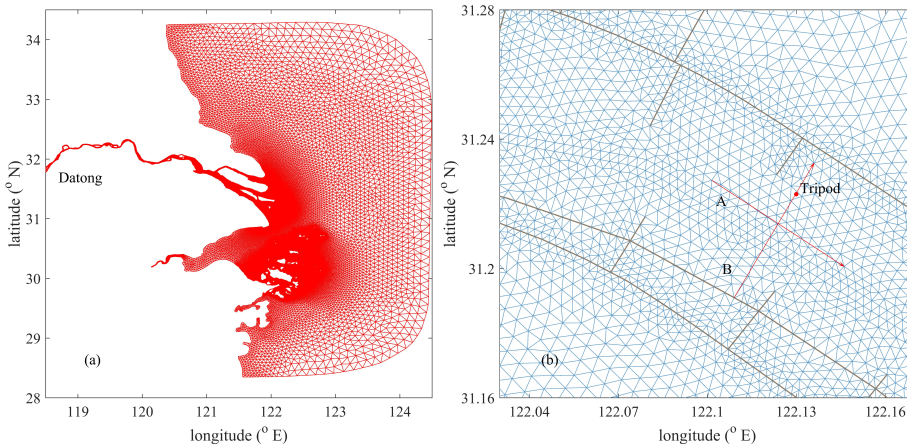
Figure 2.3: (a) Unstructured mesh for the Changjiang Estuary and adjacent regions. (b) An enlarged view within the NP. Section A, B is selected along- and cross-channel sections for analysis.

The model is forced by 8 major astronomical tidal constituents specified at the open boundaries, including four diurnal tides (K_1, O_1, P_1 and Q_1), four semi-diurnal tides (M_2, S_2, N_2 and K_2). The data for the tidal constituent sources are from TPXO 8 [Egbert and Erofeeva, 2002]. Daily river discharge of the CJ (data source: www.cjh.com.cn) is considered at the upstream boundary at Datong Gauging Station. The atmospheric forcing is the ERA-Interim data from the European Centre for

Medium-Range Weather Forecasts (ECMWF) with 0.125° spatial resolution and 3-hour temporal resolution. This model is discretized into 20 uniform terrain-following sigma layers, which provides sufficient vertical resolution for the bathymetry of 5 - 13 m in this channel-shoal system. The time step is set to 10 seconds with a spin-up time of 15 days. For the turbulence scheme, a Mellor and Yamada level-2.5 turbulent closure scheme with Galperin modification is applied [Chen *et al.*, 2003; Galperin *et al.*, 1988; Mellor and Yamada, 1982]. The horizontal and vertical Prandtl number defined as the ratio of turbulent eddy viscosity to the turbulent diffusivity [Chen *et al.*, 2013], are 1.0 and 0.4 respectively.

2.3. Results

2.3.1. General Physics

The main data measured by various instruments of the tripod, including water levels, fixed-point velocity and salinity are shown in Figure 2.4. The whole observation period can be divided into three phases according to the tidal condition: Phase A from 12/07 to 12/11 (neap tidal conditions), Phase B from 12/11 to 12/14 (intermediate tidal conditions) and Phase C from 12/14 to 12/18 (spring tidal conditions).
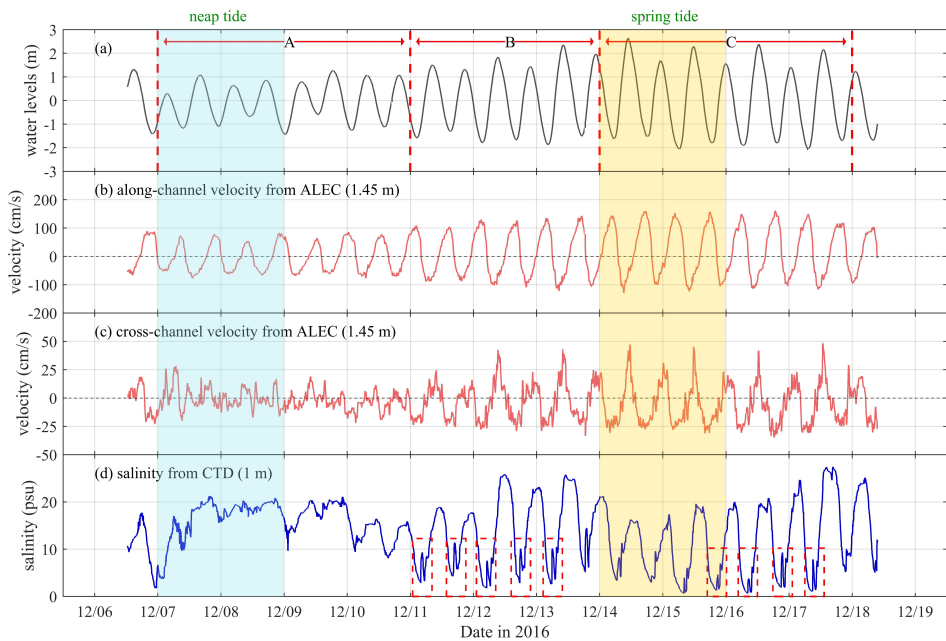
Figure 2.4: Time series of (a) water levels, (b) horizontal along-channel and (c) cross-channel velocity from ALEC, (d) water salinity from CTD by the tripod. An orthogonal coordinate according to channel direction is used for velocity decomposition. For along-channel flow, the positive value indicates direction of about 120 degrees from the north, for cross-channel flow, the positive value indicates direction of about 30 degrees from the north.

The tidal range during neap tides was ~2 m and increased to ~4 m during spring tides (Figure 2.4a). The average bottom current velocity at 1.45 mab during neap tides was 44.5 cm/s, and almost double during spring tides, reaching 86.1 cm/s (Figure 2.4b, c). The maximum current velocity exceeded 150.0 cm/s during ebb tide. The mean flood duration during neap tides was 7.29 h, whereas the mean ebb duration was 5.25 h.

The cross-channel velocity component was irregular during neap tides (Figure 2.4c) with weak-amplitude fluctuation. The maximum cross-channel velocity during neap tides wass ~25 cm/s (06:45 LST on 12/07). During intermediate and spring tidal conditions, the cross-channel velocity had a pronounced flow asymmetry. During intermediate tides, southward cross-channel flow occurred for 57% of time (with the remaining 43% northward flow), increasing to 68% of time during spring tides. Also the average strength of southward flow was greater: 15.1 cm/s during intermediate tides and 17.0 cm/s during spring tides (11.6 cm/s and 15.6 cm/s for northward flow for the respective tidal conditions). Consequently, there is a pronounced (shoal-to-channel) cross-channel velocity component, both in magnitude and duration, resulting from lateral flows.

The bottom salinity remained above ~20.0 PSU for several days with only small oscillations during neap tides. This indicates that the area remains in the range of the salt wedge during neap tides, as observed earlier by [Ge *et al.*, 2018]. During intermediate and spring tidal conditions, an oscillating salinity pattern can be observed, with values ranging from nearly 0 PSU around the low water slack to 30 PSU around the high water slack (Figure 2.4d). In addition, from 12/11 to 12/18 (phases B and C), a series of significant oscillations lasting for about 2 hours with magnitude of about 5 PSU occurred in each trough of salinity curve (Figure 2.4d). We refer to these oscillations as intratidal salinity variations (ISV), and will be elaborated on in more detail in the next section.

2.3.2. Identification of Intratidal Salinity Variation (ISV)

The ISVs were highly consistent with the tidal phase, always occurring during low water slack (marked by red rectangles in Figure 2.4d). During an ISV, the salinity first increases for about 20 minutes, and then drops for about 51 minutes (averaged value of 5 ISVs during intermediate tides). Although the ISVs were identified during intermediate and spring tidal conditions, the amplitude was larger and the duration was longer during intermediate tides. The ISVs disappeared shortly before saline flood currents entered the North Passage close to the observation area. During this period, the upper water column was dominated by ebb currents while the bottom area was dominated by flood currents (Figure 2.5e, h). This typical two-layer current structure occurred during low water slack (between ebb and flood), with weak currents in the whole water column. Importantly, during a period when ISVs occurred (green dashed lines in Figure 2.5f, i), the flow direction was ~210 degrees from the north (Figure 2.5e, h).

The observation indicates the formation of ISV is related to lateral flows. However, this measurement only demonstrates the ISV in a local perspective. It is unable to resolve the horizontal and vertical propagation of the water and salinity

2
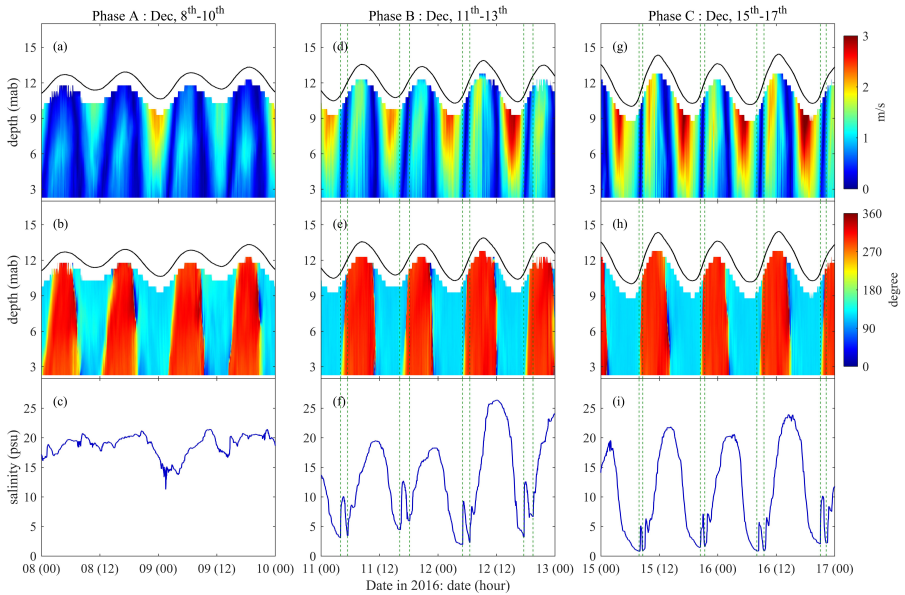
Figure 2.5: Time series of vertical profiles of flow velocity (row 1), flow direction (row 2), near-bed salinity (row 3) during neap tides (left column), intermediate tides (middle column) and spring tides (right column). The green dashed lines mark the occurrence of ISVs.

mass under the effect of the lateral flow. Therefore, the mechanism for the formation of ISV needs to be examined with a numerical model, allowing a more detailed quantitative analysis of the lateral flows.

The applied model (CE-FVCOM) has been fully validated against hydrodynamics, tide and salinity in previous studies [Ge et al., 2015, 2014; Guo et al., 2018a]. For example, averaged M_2 tidal amplitude error ($(H_{model} - H_{observation})/H_{observation}$) at 32 gauge stations in the Changjiang Estuary and adjacent coastal areas is 4% (Table 3 in Ge et al. [2014]). In this study, model results are only compared to our tripod data for further validation. A comparison of near-bed flow velocity, direction and salinity (shown in Figure 2.6) shows that the model captures the magnitude and direction of the upward-looking ADCP (data of the first cell, 2 mab), and the variation of salinity collected by CTD. The overall root mean square errors (RMSEs) for velocity magnitude, velocity direction and salinity are 0.19 m/s, 15.1 degrees and 2.6 PSU, respectively. Even more, the ISVs occurring during intermediate and spring tidal conditions are also well resolved by the model (an example is marked with green dashed box in Figure 2.6c). The magnitude of modelled ISVs is slightly smaller than that of observed ISVs. The semi-implicit scheme used in this study is capable of better simulating the two-layer current structure. It may underestimate the water flux exchange along the groynes compared to the explicit scheme which implements a generalized dike-groyne module, particularly during the flood tide period [Ge et al., 2012]. This may cause an underestimation of salinity in the

groyne-sheltered area and the smaller magnitude of ISVs as well. Since the model predicts the occurrence and correct timing of the ISVs, the model can be used to further explore formation mechanisms in more detail.
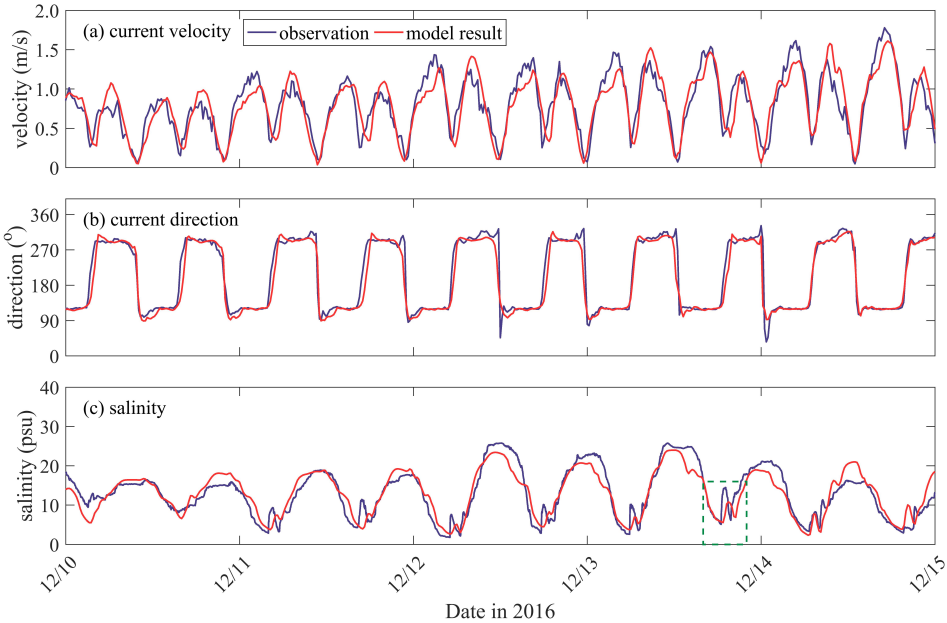
Figure 2.6: Model-data comparison between observed (blue) and simulated (red) results for near-bed tide current velocity (a), current direction (b) and salinity (c) at the observation site. The green dashed rectangle in (c) shows a typical intra-tidal salinity variation (ISV), and this ISV will be discussed in details in the following sections.

2.3.3. Formation and Breakdown of the ISV

To understand the formation and breakdown of ISV, a typical ISV during neap-to-spring transition tides is selected (marked by a green dashed rectangle in Figure 2.6c) for analysis with the numerical model. At the end of ebb, the salinity in the channel (including the observation site, Figure 2.7a) was low while the shoals are more saline. The higher salinity on the shoals generates a near-bed salinity-driven density current peaking at 0.5 m/s (Figure 2.8e, f). The transport of more saline water from the shoals towards the channel leads to an increase in near-bed salinity (Figure 2.7a-c), giving rise to the formation of ISV.

The amount of saline water stored over the shoals is limited, however. The high-salinity patch flows 1.5 km into the channel (Figure 2.8f, g) after which it dilutes or is advected up-estuary (Figure 2.8g-i). During the period of maximum cross-channel flow (Figure 2.8e), the near-surface ebb currents are close to 1 m/s (Figure 2.9e). Such a large velocity gives rise to mixing, which is illustrated with the local salinity distribution. Near the observation point, the near-surface salinity increases (Figure 2.9f-h) when the near-bed salinity decreases (Figure 2.8f-h, 2.9f-h). The salinity

rapidly rises after flow reversal when the saline flood propagates into the channel (Figure 2.9i, Figure 2.7e, f).
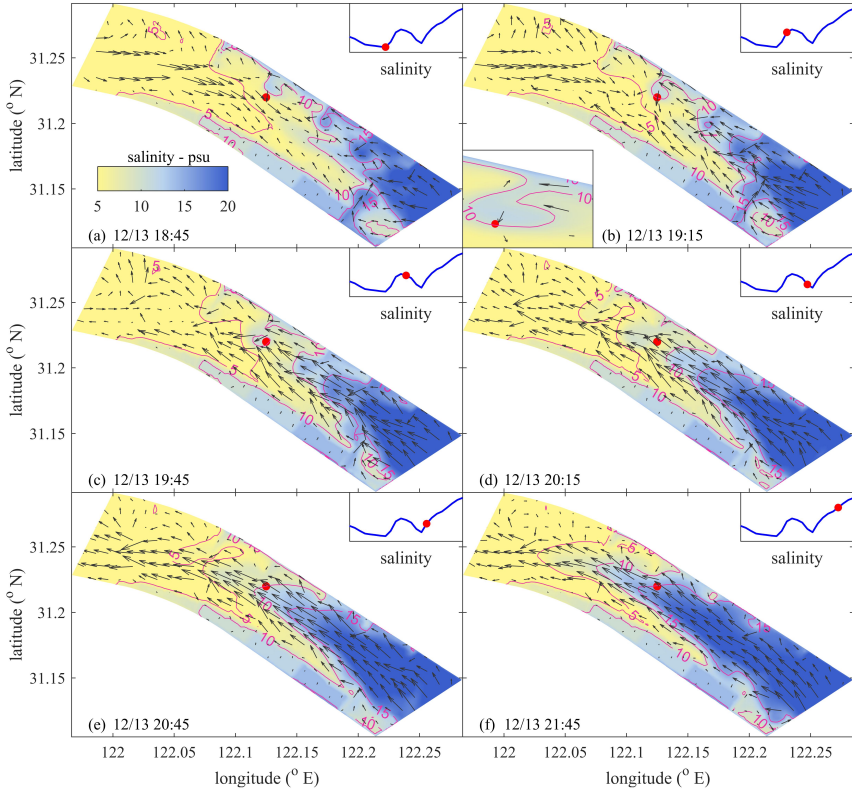
Figure 2.7: Spatial distributions of near-bed salinity and flow velocity at selected times (model result). The red dot indicates the observation site. The up-right inset shows the process of ISV and the red dot shows salinity of the site during this typical ISV period.
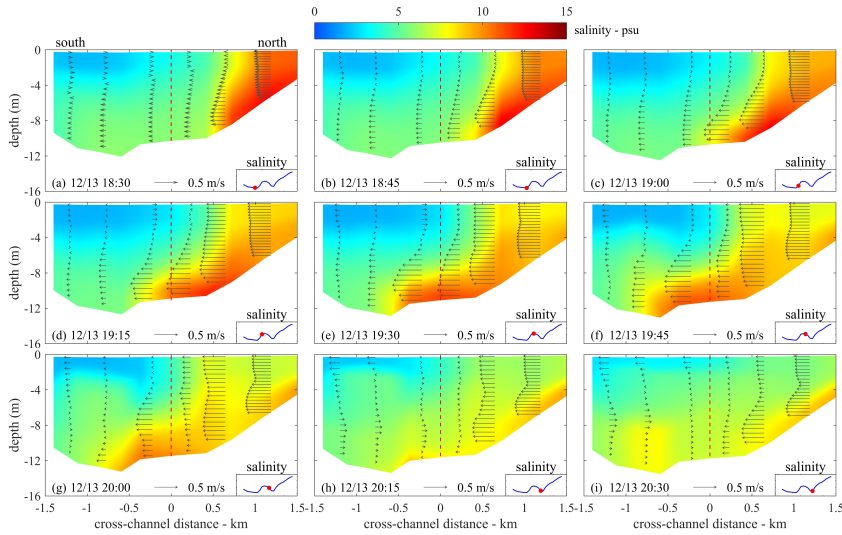
Figure 2.8: Vertical distribution of salinity and cross-channel flow velocity (arrows) at selected times (a typical intra-tidal salinity variation period). Red dashed line indicates the projection position of the observation site in a south-north cross-channel section (section B in Figure 2.3b). The down-right insets show the process of ISV and the red dot shows salinity of the site during this typical ISV period.
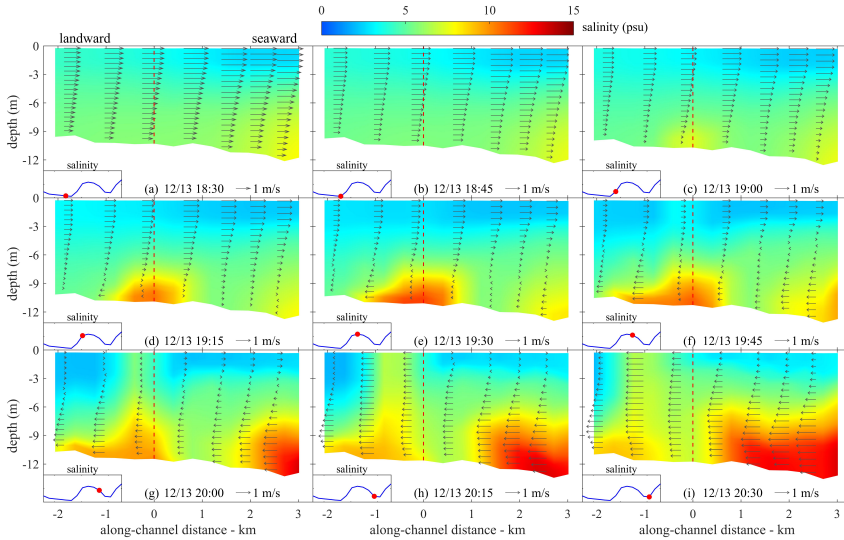
Figure 2.9: Vertical distribution of salinity and along-channel flow velocity (arrows) at selected times (a typical intra-tidal salinity variation period). Red dashed line indicates the projection position of the observation site in a west-east along-channel section (section A in Figure 2.3b). The down-left inset shows the process of ISV and the red dot shows salinity of the site during this typical ISV period.
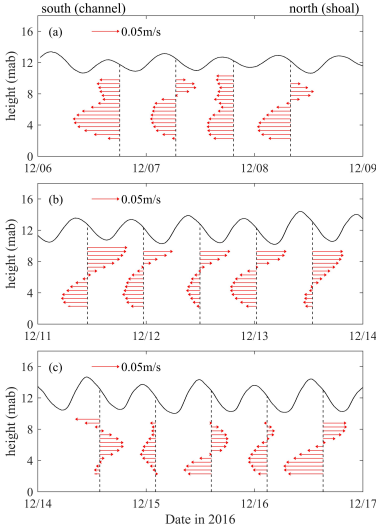
Figure 2.10: Tidally averaged cross-channel residual current calculated from ADCP results in (a) neap tide, (b) intermediate tide and (c) spring tide at the observation site.

Averaged over the tide, the lateral flows discussed above contribute to a tide-averaged cross-channel residual current (Figure 2.10). The variation of this tidally averaged cross-current over the spring-neap tidal cycle can be evaluated with the upward-looking ADCP observations. During the late neap tide and the intermediate tide when pronounced ISV was detected, the cross-channel residual current showed a clear vertical variability (Fig. 10a, b). For the majority of time, the tidally averaged cross-channel component near the bed is directed towards the channel whereas it is directed towards the shoals near the water surface.

2.4. Discussion

2.4.1. Mechanism for the Lateral Flow: Momentum Balance Analysis

Interpretation of the data and numerical model results suggests that the density-induced gradient resulting from the salinity difference between the channel and the shoal is the driving force for the lateral flow. We will further quantify this hypothesis using a momentum balance analysis.

We define the along-channel direction as the x-axis (the positive value indicates a direction of 120 degrees from the north) and the cross-channel direction as the y-axis (the positive value indicates a direction of 30 degrees from the north, away from the main channel), over which the governing equations for horizontal motions are given as follows:

$$\frac{\partial u}{\partial t} + u\frac{\partial u}{\partial x} + v\frac{\partial u}{\partial y} + w\frac{\partial u}{\partial z} - fv = -\frac{1}{\rho}\frac{\partial (P_H + P_a)}{\partial x} + \frac{\partial}{\partial z}\left(K_m\frac{\partial u}{\partial z}\right) + F_x \qquad (2.1)$$

$$\underbrace{\frac{\partial v}{\partial t}}_{A} + \underbrace{u\frac{\partial v}{\partial x} + v\frac{\partial v}{\partial y} + w\frac{\partial v}{\partial z}}_{B} + \underbrace{fu}_{C} = \underbrace{-\frac{1}{\rho}\frac{\partial (P_H + P_a)}{\partial y}}_{D} + \underbrace{\frac{\partial}{\partial z}\left(K_m\frac{\partial v}{\partial z}\right)}_{E} + \underbrace{F_y}_{F} \qquad (2.2)$$

where x, y and z are the horizontal and vertical axes of the Cartesian coordinate; u, v and w are the $x-$, $y-$, and $z-$component velocities, respectively; ρ is density; P_H is hydrostatic pressure; P_a is the air pressure at sea surface; f is the Coriolis parameter and K_m is vertical eddy viscosity coefficient. Here, F_x and F_y represent the

horizontal momentum diffusion terms in the along- and cross-channel directions, respectively.

The air pressure is omitted due to its weak contribution to the local hydrodynamics in the channel-shoal system. The hydrostatic pressure P_H satisfies:

$$\frac{\partial P_H}{\partial z} = -\rho g \;\Rightarrow\; P_H = \rho_0 g \zeta + g \int_z^0 \rho \, \mathrm{d}z \tag{2.3}$$

where g is the gravitational acceleration.

In Eqs 2.1 and 2.2, $A - F$ denote the local acceleration, advection, Coriolis force, pressure gradient, and vertical and horizontal momentum diffusion terms, respectively. The pressure gradient force term includes the barotropic (surface elevation) pressure gradient force and baroclinic (density) pressure gradient force as described in Eq 2.3.

Figure 2.11 shows the vertical distribution of momentum terms of the Coriolis force and baroclinic pressure gradient (BPG) along the selected section B at selected times at before (18:30), right on the crest of (19:30) and after (20:15) a significant ISV on 12/13. The BPG was $\sim -3 \times 10^{-4}$ m/s^2 at 18:30 LST 12/13 in the shoal area (Fig. 11d). The Coriolis force was $\sim -4 \times 10^{-5}$ m/s^2, one order of magnitude smaller than the BPG since tidal currents are weak during low water slack (Figure 2.11a). The BPG and Coriolis force jointly drove the flow southward (from the north shoal to the main channel), generating the lateral current. In this stage, the BPG was the major contributor among all dynamical forces. At 19:30 LST 12/13, the BPG continued to drive the southward lateral flow, counteracted by the Coriolis force because near bottom this Coriolis force was in the northward direction (Figure 2.11b). Similarly, the Coriolis force was one order of magnitude smaller than the BPG. Therefore, this hindrance effect could not substantially inhibit the development of the lateral flow. At the end of the ISV period when flood currents flowed into the channel, and the Coriolis force was in the northward direction in the whole section (Figure 2.11c), the BPG in the deep channel increased and had a northward component because of the movement of saline water (Figure 2.11f). Later, BPG in the deep channel would continue to increase due to seawater intrusion.

The momentum term due to flow curvature is also estimated. Eqs 2.1 and 2.2 are written in Cartesian coordinate, which do not contain separate momentum term induced by channel curvature. The momentum equation can be written in curvilinear coordinate as follows [Chant, 2010]:

$$\frac{\partial u_n}{\partial t} + u_s \frac{\partial u_n}{\partial s} - \frac{u_s^2}{R} + f u_s + g \frac{\partial \eta}{\partial n} - \frac{\partial \tau}{\partial z} = 0 \tag{2.4}$$

where s, n, z represent main-flow, lateral and vertical directions, u_s, u_n are velocity components in s, n directions, R is the radius of curvature, f is the Coriolis parameter, η is water level, τ is stress. In Eq 2.4, $\frac{u_s^2}{R}$ is momentum term of channel curvature, which is also named centrifugal acceleration. The longitude and latitude information of the north dike is transferred into a Cartesian coordinate, using a map projection method. Then the new position of the north dike in the Cartesian
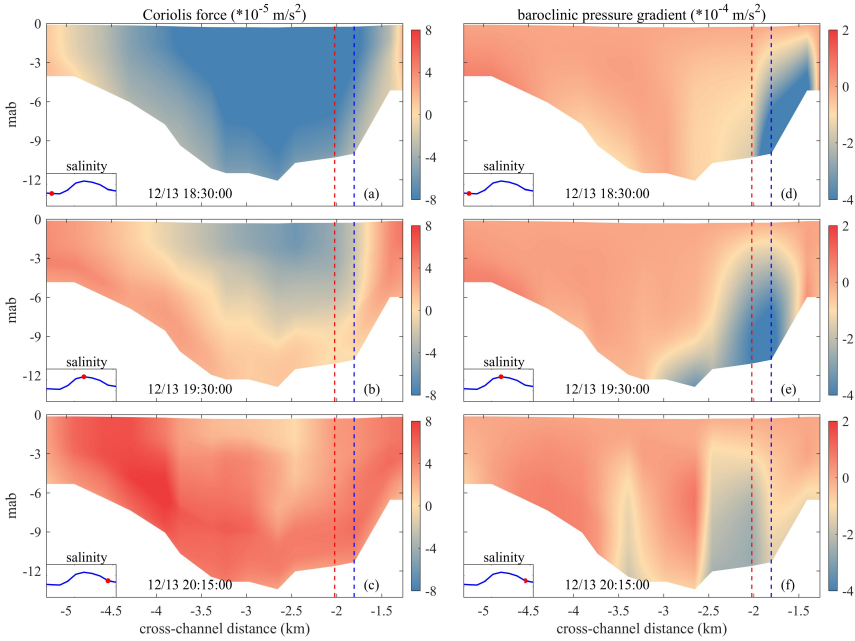
Figure 2.11: Tidally averaged cross-channel residual current calculated from ADCP results in (a) neap tide, (b) intermediate tide and (c) spring tide at the observation site.

coordinate is fitted with a quadratic curve to calculate R. For cross-channel section B (Figure 2.3b) which passes the observation site, $R \approx 49.7$ km, maximum magnitude of u_s was about 1.9 m/s (Figure 2.5b), thus maximum value of $\frac{u_s^2}{R}$ was about 7.3×10^{-5} m / s^2. At the beginning of ISV (18:30 LST 12/13), u_s was about 0.2 m/s, and the effect of channel curvature was several orders of magnitude smaller than that of the BPG. Therefore, the baroclinic pressure gradient caused by the horizontal salinity gradient was the main driving force for the formation of the lateral flow.

Closer to the channel bend (Figure 2.1), $R \approx 28$ km, and here curvature effects could be larger. During the ebb tide, the maximum value of $\frac{u_s^2}{R}$ is about 1.3×10^{-4} m / s^2, towards the outside of the channel. While the Coriolis force is about -1.1×10^{-4} m / s^2. These two forces were close and the joint effect is small. However, during the flood tide, maximum centrifugal acceleration is about 1.0×10^{-4} m / s^2 while the Coriolis force is about 1.3×10^{-4} m / s^2. The combined effect of channel curvature and Coriolis force (about 2.3×10^{-4} m / s^2 in total) is comparable to that of the baroclinic pressure gradient which generates the lateral flow. In the other word, this combined effect could also lead to an opposite lateral flow during flood tide period close to the river bend.

Because u_s in the channel curvature term is squared, this term always has the same sign within a whole tidal cycle. It may therefore strengthen or weaken the

Coriolis term in different stages of a tidal cycle, giving rise to tidal asymmetry in lateral flows during flood and ebb tide [Chant, 2010]. In many cases, lateral flow or lateral circulation could be dominated by the centrifugal acceleration for a period in a tidal cycle [Kim and Voulgaris, 2008; Lacy and Sherwood, 2004; Nidzieko *et al.*, 2009] as the radius of curvature R is much smaller than that in our study. Although R is relatively large and the curvature induced term appear to be less important than other terms, variation of R leads to different lateral circulation patterns in different cross-channel sections of the North Passage. In this study, the maximum joint effect of Coriolis term and centrifugal term is still smaller than the BPG when ISV was generated, indicating the significance of the trapped saline patch in the shallow shoal and the intensity of this lateral flow.

2.4.2. Stratification and Mixing

Differential advection of the water mass leading to ISV greatly influences stratification and mixing process in the channel-shoal system. During the ISV period, the cross-channel and along-channel salinity distribution and velocity showed a pronounced vertical variability (Figure 2.8, Figure 2.9). To what extent feedback mechanisms exist between salinity-induced stratification and the flow is further investigated with the gradient Richardson number (R_i):

$$R_i = -\frac{g}{\rho_w} \frac{\partial \rho / \partial z}{\left[(\frac{\partial u}{\partial z})^2 + (\frac{\partial v}{\partial z})^2 \right]} \tag{2.5}$$

where ρ_w is water density, $\frac{\partial \rho}{\partial z}$ is density gradient, u, v are velocity components in $x-$, $y-$direction. The water column stratifies when R_i exceeds 0.25. Therefore $\log_{10}(R_i/0.25)$ is used as an index for the degree of stratification (Figure 2.12), with positive values indicating stratifying conditions). The density of water did not always increase from the surface to the bottom, resulting in negative values of R_i which give rise to the blank areas in Figure 2.12 when taken as a logarithm. As explained earlier, the saline water remaining in the shallow areas flowed downslope at the end of the ebb due to horizontal density differences, giving rise to the ISV. As a result of this density current, the near-bed channel gradually became more stratified (Figure 2.12c) by differential advection of salinity. During the peak of the ISV (Figure 2.12c), the larger part of the water column was salinity-stratified. However, the layer very close to the bed had a weak stratification (Figure 2.12c). This is because of the large gradient of velocity in the near-bed area due to the friction (Figure 2.8e).

The gradient Richardson number (R_i) indicates the stratification at a specific height in the whole vertical column while the bulk Richardson number (R_{ib}) provides information of the whole water column (bottom to surface). R_{ib} can be calculated as [Hoitink *et al.*, 2011; Lewis, 1997]:

$$R_{ib} = \frac{gD\Delta\rho}{\rho_w \left| \overrightarrow{u_s}^2 \right|} \tag{2.6}$$
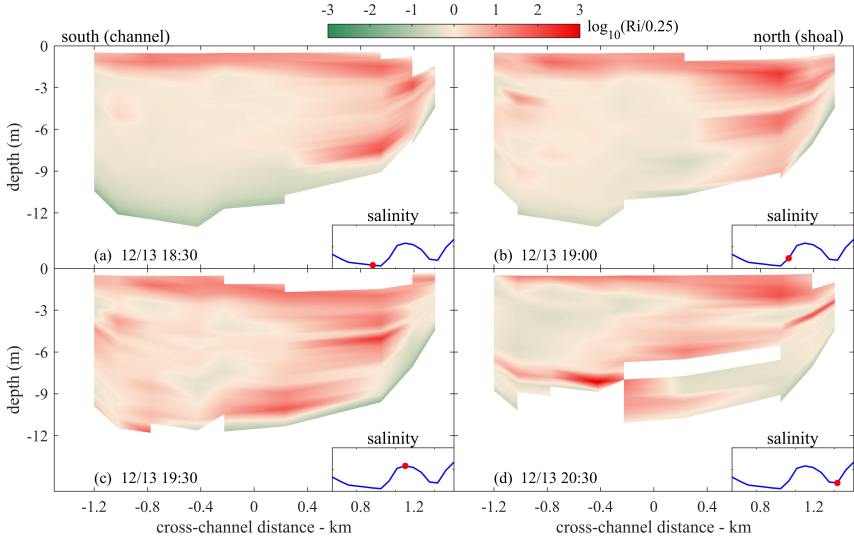
Figure 2.12: Distribution of $\log_{10}(R_i/0.25)$ in cross-channel section B (a) before the ISV, (b) in the increasing stage of ISV, (c) at the peak of ISV and (d) at the end of the ISV. The zero position in $x-$axis indicates the position of the observation site in the section. The down-right inset shows variation of salinity, and the time-stamp salinity at the site.

where D is the water depth, $\Delta\rho$ is the density difference between surface and bottom, $\overline{\rho_w}$ is the averaged density of the water column, $\overrightarrow{u_s}$ is the horizontal velocity at the surface. The gradient Richardson number of different layers and the bulk Richardson number are shown in Figure 2.13. Turbulent kinetic energy (TKE) per unit mass is also used for further interpretation of vertical mixing. TKE can be calculated using the high-frequency velocity data collected by ADV as:

$$TKE = \frac{1}{2}(\overline{u'^2} + \overline{v'^2} + \overline{w'^2}) \tag{2.7}$$

where u', v' and w' are velocity fluctuations of the streamwise, lateral and vertical components and the over-bar denotes time-averaging values.

Green, blue and red dashed lines in Figure 2.13 indicate the start, peak (salinity maximum) and end of the ISV, respectively. Note that Figure 2.13a is based on model results while Figure 2.13b, c are based on results of the tripod observation. Therefore, a small time lag of ISV process between these two methods can be found in Figure 2.13 (vertical dashed lines are different in three sub-graphs). Shortly before the start of the ISV (green dashed lines), the near-bottom R_i and R_{ib} were below 0.25 (Figure 2.13a), indicating well-mixed condition. Both the time-variation in near-bed salinity ($\mathrm{d}sal / \mathrm{d}t$, Figure 2.13c) and vertical salinity variation (Figure 2.8a) were small. All information therefore suggests a steady, well-mixed water column near the end of the ebb. During the first stage of the ISV (between green and blue dashed lines), the salinity and R_{ib} increased rapidly (Figure 2.13). R_i at 1.5 mab showed a different variation from R_i at 0.5 and 1.0 mab. At 1.5 mab, there
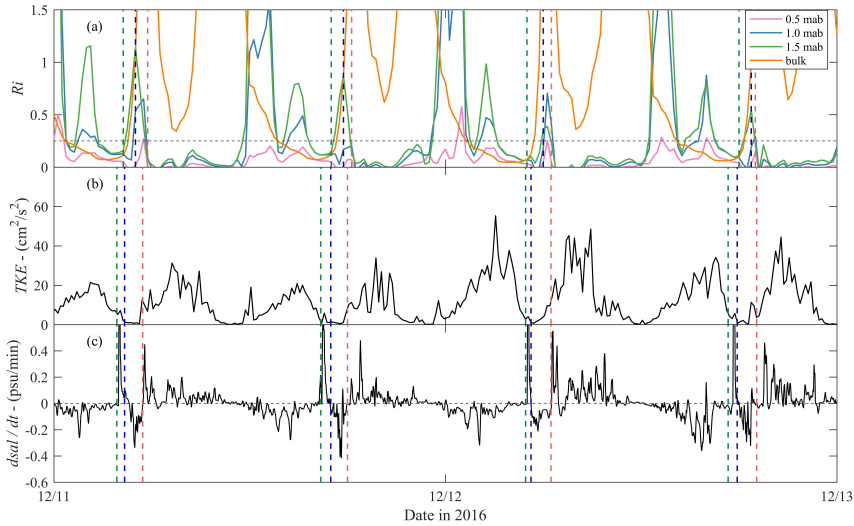
Figure 2.13: Time series of (a) gradient Richardson number at 0.5 mab (pink), 1.0 mab (blue), 1.5 mab (green) and bulk Richardson number (orange), (b) turbulent kinetic energy (TKE) at the observation site, (c) rate of salinity change in time. Green and blue dashed lines indicate the increasing stage in the ISV, blue and red dashed lines indicate the decreasing stage in the ISV.

was a pronounced stratification as it was close to the interface between water in the salinity patch and ambient water. During the decreasing stage of the ISV (between blue and red lines), the whole water column (as indicated with the bulk Richardson number) remained stably stratified ($R_{ib} > 0.25$). The near-bed gradient Richardson numbers suggest a non-stratified water column, but this was because the halocline was located higher up in the water column. The observation that the water column was stratified during the decline of the ISV suggests that longitudinal advection (and not mixing) was the main mechanism responsible for the salinity decrease. Well-mixed conditions ($R_{ib} < 0.25$) re-established halfway the flood, during periods of high TKE.

2.4.3. Effects of Dikes and Groynes

The investigated tidal channel was surrounded both towards the south and north with dikes and overflowing groynes (Figure 2.1). Although the main parts of the groynes from the tip are submerged by sediment deposition, the remaining parts near dikes are still exposed during low tide, which shapes the groyne-sheltered area as a semi-enclosed region. The groynes create nearly stagnant water masses, and therefore strengthen differential advection of salt water. As a result, these groynes may greatly contribute to the transverse flows (and therefore ISV).

The effect of groynes is quantified by rerunning the model with one groyne (nearest to the observation site) removed. As a result, the ISV is no longer predicted at the observation site (Figure 2.14a). The bottom salinity distribution clearly shows
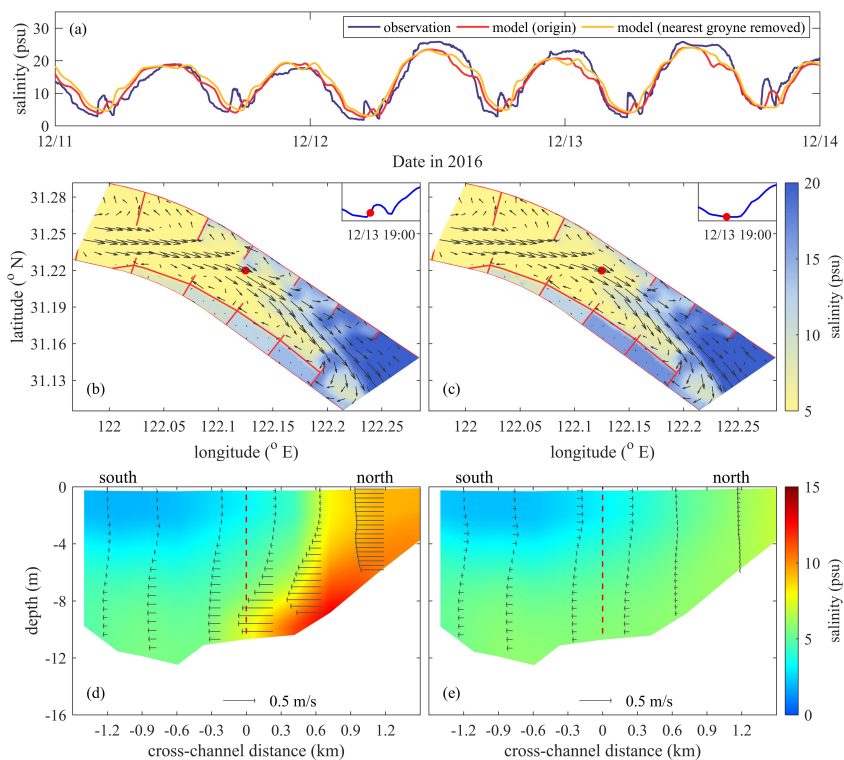
Figure 2.14: Model-data comparison with groyne-removed case added (a), comparison between original case (b, d) and groyne-removed case (c, e) at the same time in bottom salinity distribution (b, c) and vertical salinity distribution (d, e).

that no high-salinity water is trapped in the north shoal without the groyne (Figure 2.14c). This is also clear in vertical salinity distribution in the cross-channel section and cross-channel velocity is much smaller than the original case (Figure 2.14e). For downstream areas where groynes are still present, salinity is still influenced by the groynes (Figure 2.14c).

The numerical model results suggest that the groyne fields north of our observation site contribute much stronger to the generation of ISV's than their southern counterparts. Due to the retention effect all along the northern groynes lateral flows developed, and the salinity varied over the tidal cycle (Figure 2.7). This was not true, however, for the southern groynes. The southern groynes were connected by an additional along-estuary dike (Figure 2.14b) which limited exchange flows between the groyne fields and the estuary. As a result, their salinity remained fairly constant in time (Figure 2.7) and cross-channel flows did not develop from the south (Figure 2.8).

The impact of groynes on lateral flows reported here has, to our knowledge, not been published elsewhere in the scientific literature, but constitutes an important contribution. Many researchers have reported groynes' impacts on flow hydrodynamics [Brevis et al., 2014; McCoy et al., 2008; Sukhodolov, 2014] and mass exchange [McCoy et al., 2007; Uijttewaal et al., 2001; Weitbrecht et al., 2008]. These studies do not include salinity-induced density effect which is closely related to groynes. Groynes are used throughout the world to channelize flow, preventing siltation rates in fairways maintained to provide access to ships. Lateral flows may significantly contribute to near-bed sediment dynamics and siltation rates, and therefore resulting in the exact opposite effect for which the groynes were originally designed. As a result, comprehensive understanding of the impact of such engineering works are required for sustainable development of human-impacted estuaries.

2.4.4. Implications of ISV in Other Studies

Earlier studies in the North Passage of the Changjiang Estuary also identified the existence of ISV, but was not paid much attention to. Song et al. [2013] conducted a quadrapod observation at the slightly south of the deep channel. They observed a similar intra-tidal salinity variation during the low water slack (in their Figure 2a). They used velocity skew and flux skewness to examine the lateral sediment transport, identified a net sediment transport from the south groyne to the deep channel with an opposite lateral transport from the north to the south side of the channel in near-bottom area (below 1 mab). This opposite lateral flow and the ISV was likely generated with the same mechanisms discussed in our study. We believe that the ISV in their study was also generated by saline water trapped in the north groyne-sheltered area as this saline water mass could move across the deep channel to where Song et al. [2013] conducted the observation. Actually, the ISV in their study should be a further dispersion of ISV generated from the north shoal and that is why the magnitude of ISV at their observation site was much weaker. The lateral flow discussed in our study should be taken into account when considering sediment transport in the North Passage, as its movement affects the whole deep

channel in the cross-channel direction. This will improve the knowledge of severe siltation issues in the channel.

ISV was also detected in other estuaries. Ralston *et al.* [2012] deployed fixed instruments frame in the channel and on the shoal of Hudson River estuary, which also revealed clear evidence for ISV (in their Figure 3a). The bottom salinity measured in the channel also varied within the tidal cycle during low water slack, and was also the result of lateral flows. They concluded their lateral flow was primarily related to topography features in a channel-shoal system. We believe that more estuaries and channels all over the world are characterized by lateral flows resulting in ISV's albeit that the responsible mechanism (in our case the baroclinic pressure gradient, in Ralston's case the topography) may differ.

The ISV directly gives a strong indication for lateral flows in a channel-shoal system. ISV can be a simple indicator of lateral flow and lateral processes which should be considered when investigating the hydrodynamics and sediment dynamics of estuaries with extensive shoals. Actually, the ISV is just one typical feature under the modulation of lateral flow. Besides, particular small-scale fluctuation in other variables (for example temperature) also occurs concurrently with ISV. Generally speaking, these small-scale fluctuations in multiple variables all indicate the importance of the lateral flow caused by many different reasons in a tidal channel-shoal system.

2.5. Conclusions

In this study, a tripod system integrated with multiple instruments was deployed in the North Passage of the Changjiang Estuary to measure lateral flow and its impacted salinity transport. Observation results revealed periodic formation of intra-tidal salinity variation during low water slack. The tripod observations indicated the intra-tidal salinity variation (ISV) was generated by a near-bed lateral flow from the shallow shoal to the deep channel. A high-resolution unstructured-grid model for the Changjiang Estuary has been applied to simulate this lateral flow and the salinity transport. The numerical simulation showed that the high-salinity water trapped over the shoal was transported to the deep channel during ebb tide. The momentum balance analysis based on model results identified the density-induced baroclinic pressure gradient was the dominant physical mechanism for the generation of this lateral flow. Cross-channel residual current had a consistent near-bed shoal-to-channel component, which was closely connected with the shoal-to-channel lateral flow. Salinity transport also showed a southward net transport pattern.

This mechanism produced intra-tidal peaks in salinity and influenced pattern of stratification and mixing in the cross-channel section. Strong stratification occurred with and enhanced by the lateral flow, which can potentially affect sediment behavior (for example hindered settling) and modulate the pattern of sediment transport.

The ISV can be a signal of active lateral process in a tidal estuary, especially in a human-impacted channel-shoal system. Our simulations show that dikes and groynes greatly influence the flow field in the channel and the retention effect of groynes predominantly contributes to this lateral flow. This conclusion reminds us of more caution when designing such engineering structures. The findings reported

here provide a key element for future work on sedimentation issues in general, but in the North Passage in particular, since our work suggests that groynes generate a residual current directed from the shoals to the channel.

In particular, the role of salinity-induced currents on sediment dynamics as well as sediment-induced density effect on lateral flows needs to be further investigated. Since the results reported in this study were observed and simulated under dry-season freshwater discharge from the upstream Changjiang, caution should be taken when applying these results to wet season when freshwater discharge can be three to four times larger. Additional observations and model simulations are needed in that case.

3

Study of Lateral Sediment Transport in a Channel-Shoal System

Abstract

Lateral flows redistribute sediment and influence the morphodynamics of channel-shoal systems. However, our understanding of lateral transport of suspended sediment during high and low water slack is still fairly limited, especially in engineered estuaries. Human interventions such as dike-groyne structures influence lateral exchange mechanisms. The present study aims to unravel these mechanisms in a heavily-engineered, turbid channel-shoal system in the Changjiang Estuary, using a high-resolution unstructured-grid three-dimensional model and in-situ observations. Analysis of model results reveals two typical transport patterns during slack water conditions, i.e. shoal-to-channel transport during low water slack and channel-to-shoal transport during high water slack. A momentum balance analysis is carried out to explain mechanisms driving the lateral transport of suspended sediment during high water slack, revealing the importance of lateral pressure gradients, Coriolis force, and the curvature-induced term. Groyne fields play a crucial role in sediment transport, especially during low water slack. A model scenario in which one groyne is removed reveals that groyne fields strongly influence lateral sediment transport. The decomposition of the sediment transport flux reveals that the turbidity maximum is shaped by a balance between seaward advection by residual flows, and landward transport by tidal pumping and gravitational circulation. Within the turbidity maximum, sediment is laterally redistributed by lateral flows during slack water conditions, greatly influencing estuarine channel morphology.

3.1. Introduction

Sediment transport in estuaries directly influences the bed level which in turn impacts the navigability of shipping channels. Sediment dynamics also influence estuarine ecology, for instance through water clarity (and therefore primary production, providing the base of the food chain) and habitat suitability (especially on the intertidal areas) - see Wood [1997]. In many systems worldwide, estuarine sediment dynamics are increasingly modified by changes in river and sediment discharges [Guo *et al.*, 2018b; Syvitski, 2005; Walling and Fang, 2003] or more local interventions [Wang *et al.*, 2015], requiring a thorough understanding of transport processes.

The estuarine suspended sediment concentration (SSC) is highest in the Estuarine Turbidity Maximum (ETM). ETMs result from longitudinal (along-channel) sediment convergence, i.e. converging sediment transport generated by combined effects of residual estuarine circulation, tidal dynamics, and sediment erosion and deposition [Dyer, 1988; Officer, 1981]. Estuarine circulation is the combined effect of gravitational circulation [Postma, 1967], internal tidal asymmetry [Jay and Musiak, 1994] due to tidal straining [Simpson *et al.*, 1990], lateral tidal residual flows [Lerczak and Rockwell Geyer, 2004] and river flow; the relative importance of each component is highly variable. Residual transport by time lag effects, such as settling lag and scour lag [Postma, 1961], is the result of sediment properties (settling velocity, critical shear stress for erosion) in combination with asymmetries in the hydrodynamics (time-varying or spatial asymmetries). ETMs are abundant worldwide, and have been studied in great detail - see de Nijs and Pietrzak [2012], McSweeney *et al.* [2016] or Burchard *et al.* [2018] for examples and more detailed references. Nevertheless, sediment transport in systems that have complex ETM dynamics or extremely high SSC, especially when strongly influenced by groyne fields, is still poorly understood. Ralston *et al.* [2012] demonstrated through use of in-situ observations and a numerical model that the sediment flux in a channel-shoal system can be strongly laterally segregated. The shoals can serve as pathways for seaward sediment flux and the channel can support the landward flux. However, this laterally varying, longitudinal transport pattern may differ substantially in channel-shoal systems which are impacted by dikes and groynes, for example the North Passage of the Changjiang Estuary.

In addition, the role of lateral flows (cross-channel flows) in sediment transport are increasingly recognized. Although lateral flow normally has a much smaller magnitude, its impact on momentum balance and transport of particles cannot be neglected [Lerczak and Rockwell Geyer, 2004; Dronkers, 1996]. Lateral flow, caused by lateral depth variation, channel curvature, and Coriolis acceleration among others, drives and traps sediment [Huijts *et al.*, 2006]. These mechanisms reinforce or counteract each other [Kim and Voulgaris, 2008], enhancing the complexity of lateral flow and sediment transport. Chen *et al.* [2009] used a hydrodynamic model to explore the influence of wind effect on lateral circulation in stratified and unstratified conditions. They concluded that the wind direction could change the direction of lateral sediment flux (from channel to shoals for down-estuary winds). Chen and de Swart [2018] concluded that the longitudinal variation of lateral flow drives

trapping of sediment in the North Passage. Their work primarily addressed tide-averaged effects of lateral flow and lateral trapping of sediment. However, there is also a need to investigate the intratidal variation in sediment transport processes in greater detail.

Groynes are often constructed in the coastal zone [Kristensen et al., 2016; Scott et al., 2016], protecting shorelines from erosion problems. They are also widely applied in rivers, tidal inlets, and navigation channels to mitigate deposition problems. Most of our knowledge about groynes is primarily based on zero-density-gradient conditions. Ouillon and Dartus [1997] set up a three-dimensional model to simulate a shallow turbulent flow around a groyne in a rectangular channel. Uijttewaal et al. [2001] explored exchange process between a groyne field and the main stream in a riverine condition. They observed two types of exchange related to two-dimensional flow, and mentioned a small three-dimensional effect which could cause a net outward flow at the free surface. However, salinity-induced density gradients which are widespread in estuarine environments can greatly impact groyne-related three-dimensional effects, such as lateral circulation, stratification, and near-bed transport of high-concentration water mass. Zhou et al. [2019] reported that near-bed lateral flows were strengthened by retention of high-salinity water during ebb tides. This lateral flow greatly influenced lateral transport processes, as evidenced by a pronounced intratidal salinity variation near the deep channel. Nevertheless, our understanding of the effect of groyne fields in estuarine environments is still very limited. On the other hand, Luan et al. [2018] concluded that the existence of dikes and groynes caused attenuation of currents, decrease of bed shear stress, and enhanced deposition in the groyne-sheltered area. Therefore, the reported lateral flow and abundant deposition in the groyne-sheltered shoal jointly highlight a need for research on lateral transport of suspended sediment and effects of groynes.

The objective of the current work is therefore to quantify and analyze the influence of lateral flows, with attention to the effect of groynes on sediment transport. For this purpose, we investigated the North Passage of the Changjiang Estuary. The North Passage is very turbid, suffering from high siltation rates [Ge et al., 2018], and subject to lateral flows strengthened by an extensive groyne system [Zhou et al., 2019]. Earlier work [Ge et al., 2018; Liu et al., 2011; Song et al., 2013] revealed the occurrence of fluid mud in the Changjiang Estuary (particularly in the North Passage). Most of these earlier analyses are based on single-point observations which fail to capture the complex spatial dynamics of such high-concentration layers. Therefore, in this study we use a sediment transport model, which is validated against field data collected using a tripod system, to investigate the lateral transport of suspended sediment. This paper is organized as follows. The study site, observational methods and applied model are described in section 3.2. The model results are presented in section 3.3, followed by a more in-depth analysis of transport mechanisms (section 3.4). Discussion and conclusions are summarized in section 3.5 and 3.6, respectively.

3.2. Study Site, Observational and Numerical Method

3.2.1. Study Site

The North Passage is the main navigation channel among four outlets of the Changjiang Estuary (Figure 3.1). To enhance shipping capacity, the Deepwater Navigation Channel (DNC) project has been conducted in the North Passage. The depth of the main channel is maintained at 12.5 meters and the channel is protected by combination of dikes and groynes [Ge *et al.*, 2012]. The DNC project includes 2 long dikes with 19 groynes attached to these 2 dikes. Before the DNC project, the water depth in the main channel was only about 7 meters (below the local minimum theoretical tidal level, similarly hereinafter). The project has three phases and the channel has been deepened from 7 meters to 12.5 meters (350 - 400 meters in width) after all phases [Hu and Ding, 2009]. Impermeable dikes are designed near the mean tidal level to block the tidal current, and groynes are designed to increase flow velocity and maintain water depth in the channel [Ge *et al.*, 2012]. In summary, the design of this project has three aims, (1) increasing the water depth to fulfill the demand of ocean shipping (dredging and deepening), (2) preventing sediment transport into the North Passage (dikes), and (3) increasing sediment erosion in the main channel (groynes). In 2016, the south dike was heightened to about 1.9 m above the minimum theoretical tidal level. Most of the north dike was heightened to about 3.4 m above the minimum theoretical tidal level, which becomes a road nowadays. This supplementary engineering work significantly blocked the overtopping flow, making the North Passage a laterally closed system.

The North Passage suffers from extremely high siltation rates, varying between 60 and 80 million $m3/year$ [Wang *et al.*, 2015]. Large amounts of sediment also deposited in the relatively sheltered groyne fields, forming the present-day channel-shoal system. Most dredging work is conducted within the main channel of curved region between Groyne N4 and N7 (Figure 3.1). In 2016, about 35 million m^3 of fine sediment was dredged in this area and most of the sediment was used for land reclamation. The median grain size of suspended sediment is 7 - 11 μm [Guo and He, 2011]. In the model used in this study, dikes and groynes are treated as 'impermeable walls' which means there are no overtopping flows across these structures. This treatment of dikes and groynes is reasonable as the whole south dike has been heightened and most of the north dike has been heightened.

This channel-shoal system is affected by both fluvial and tidal forcing. According to data from the Datong Gauging Station, the average water discharge of the Changjiang River is about 40,000 m^3/s in the wet season, with the maximum exceeding 70,000 m^3/s, and about 10,000 m^3/s in the dry season. Reduction of sediment supply due to the upstream Three Gorges Dam (TGD) project is significant and its influences on morphodynamics are profound [Luan *et al.*, 2016; Yang *et al.*, 2014a]. Along the coast of the East China Sea, semi-diurnal tides are dominant with a mean tidal range of about 2.7 m.

3
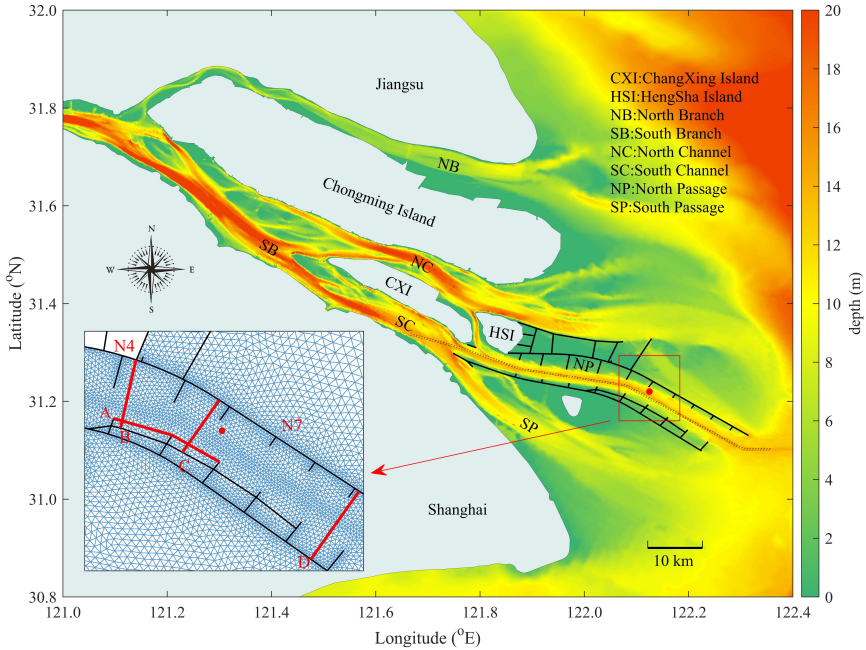
Figure 3.1: Bathymetry of the Changjiang Estuary and adjacent regions. Black lines in the river mouth represent dikes and groynes around the North Passage. Two dashed lines indicate the deep channel. Red dot indicates the measuring site. Zoomed-in sub-figure shows the unstructured mesh used in the model and four red lines indicates four transects for further analysis. The measuring site is 2.26 km from the north dike, 1.05 km from the nearest groyne tip.

3.2.2. Observations

A tripod frame was deployed on the river bed (about 10 m below the local minimum theoretical tidal level) north to the deep channel in the North Passage (Figure 3.1). The tripod location (between the north shoal and the main channel) was determined by the aim of detecting channel-shoal sediment transport and exploring effects of groynes (north groynes are longer). The side slope of this location is about 1:1000, indicating tripod observations will not be affected by the slope. The tripod integrated two RDI Acoustic Doppler Current Profilers (ADCPs), a Nortek Acoustic Doppler Vector (ADV), a Point Current Meter (ALEC, JFE ALEC CO., LTD, JAPAN), a Tide/wave Logger (RBR, RBR Ltd., Canada), a Conductivity, Temperature, and Pressure Recorder (CTD, Sea-Bird Electronics, Inc., USA), and an Optical Backscattering Sensor (OBS, D&A Instruments CO, type: 3A, USA). The height of OBS turbidity sensor was 0.9 m above the bed and the temporal resolution was 100 seconds. Water turbidity detected by the OBS was calibrated to acquire suspended sediment concentration (SSC) at our laboratory with sediment samples collected at the measuring site. The same calibration process was introduced in detail in Ge *et al.* [2018]. Caution should be taken if the OBS is used in an extremely high SSC environment (this limit depends on the performance of a specific

OBS and can be found during the calibration), which may cause ambiguity problem at concentrations exceeding 10 g/L (i.e. a low optical output could mean a low or high concentration). However, this problem did not exist during our observation as the maximum SSC was up to 10 g/L, and the relation between OBS output and SSC can be described by a piecewise regression function. Detailed configuration of this tripod observation can be found in Zhou *et al.* [2019].

Data collected by the tripod (Figure 3.2) included water levels, single-point current velocity (decomposed in along- and cross-channel directions), near-bed salinity, and SSC collected over a 12-day period starting from December 6th, 2016 (abbreviated as 12/06). The whole observation was divided into three phases (Figure 3.2f) based on hydrodynamic conditions: Phase A represents neap tidal conditions (12/07 ~ 12/11), Phase B represents intermediate tidal conditions (12/11 ~ 12/14), and Phase C represents spring tidal conditions (12/14 ~ 12/18).
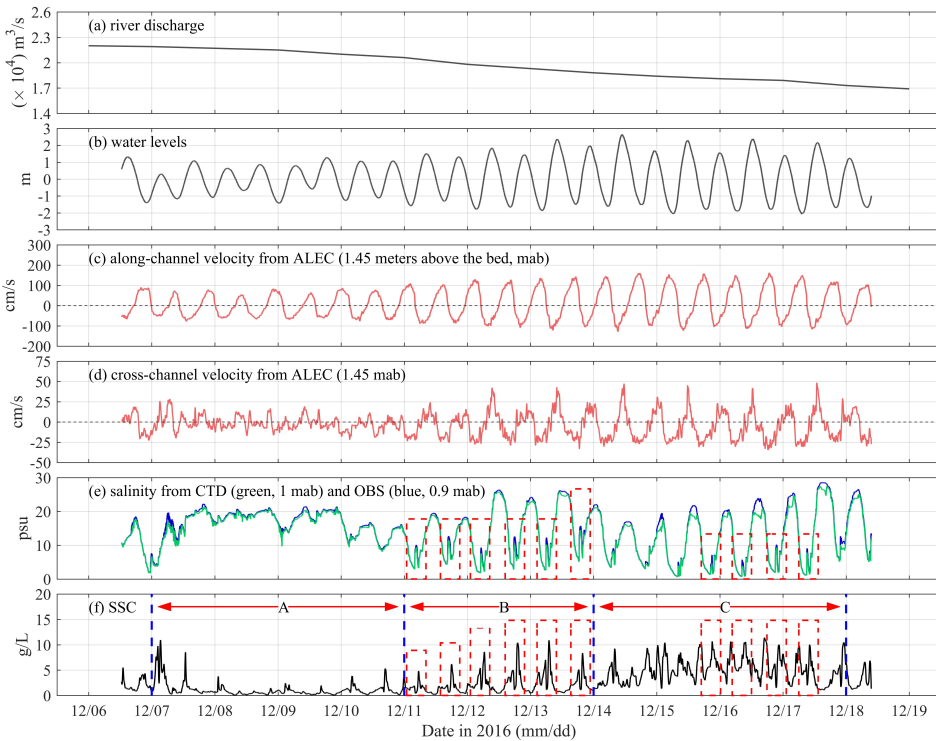
Figure 3.2: Time-series of (a) river discharge, (b) water levels, (c) horizontal along-channel and (d) cross-channel velocity monitored with ALEC, (e) salinity from CTD and OBS, and (f) suspended sediment concentration from OBS (at 0.9 m above the bed). For the along-channel flow, the positive value indicates direction of about 120 degrees from the north, for cross-channel flow, the positive value indicates direction of about 30 degrees from the north. For other locations, ebb currents (downstream) are positive in along-channel direction, currents from south shoal to north shoal (normal to ebb currents) are positive in cross-channel direction.

River discharge during this period was decreasing from 2.3 to $1.7 \times 10^4 \ m^3/s$

(Figure 3.2a). The relatively low river discharge in dry season indicates the dominance of tidal forcing. Tidal form factor (F) calculated with observed data at the measuring site is 0.247 ($F = (K_1 + O_1)/(M_2 + S_2)$), using amplitude of each constituent, indicating semi-diurnal tides. The tidal range (based on the water depth measured by the OBS pressure sensor) increased from about 2 m at neap tide to about 4 m around spring tide (Figure 3.2b). During neap tide conditions, the along-channel bottom velocity peaked at -77 to 83 cm/s (Figure 3.2c, ebb currents positive), increasing to -129 to 160 cm/s during spring tide. Along-channel velocities showed clear tidal variation, indicating effects of groyne-induced eddies were very limited for longitudinal flows in the deep channel (otherwise there would be lots of irregular fluctuations in the along-channel velocity curve rather than such a clear tidal variation). The cross-channel velocity was similarly strengthened during spring tide (Figure 3.2d). However, the cross-channel flow also developed a residual flow component, with negative flows (south shoal to north shoal positive) lasting longer, especially in the period before spring tide (Phase B). The cross-channel velocities could be affected by groyne fields, as groynes have a retention effect of salinity during ebb tide. The retention effect could consequently form a density gradient between the north shoal and the main channel, resulting in a lateral flow pattern. This is explained in detail in section 3.3.1. It should be noted that this lateral flow/transport process is not directly affected by groyne-induced eddies as these eddies mainly exist within groyne fields [Ge et al., 2012; Uijttewaal et al., 2001]. During neap tide the salinity was higher, suggesting more pronounced salinity intrusion (Figure 3.2e). Salinity data acquired by CTD and OBS showed good consistency, both depicting the intratidal salinity variation during low water slack (LWS, and HWS for high water slack). The intratidal salinity variation lasted for about 1.5 hours with a 5-psu salinity oscillation [Zhou et al., 2019]. After neap tides, SSC greatly increased with clear periodic peaks (Figure 3.2f). Six SSC peaks with a similar intratidal variation pattern occurred during Phase B, the averaged SSC was 2.1 g/L. During Phase C, the averaged SSC was 5.0 g/L, four times larger than that of Phase A (1.1 g/L).

The SSC variation during Phase B showed a clear bimodal structure (Figure 3.2f) which corresponded to the intratidal salinity variation (Figure 3.2e). For the intratidal salinity variation, salinity first increased and then decreased, forming a sub peak in the trough. The SSC showed an opposite variation, i.e. it first decreased and then increased, forming a bimodal structure in the main peak. The intratidal salinity variation results from lateral salinity transport [Zhou et al., 2019]. The synchronous but exactly opposite variation of salinity and SSC indicates the formation of the bimodal structure of SSC is related to similar lateral transport process. The water mass transported during this process had high salinity but low SSC, leading to the opposite variation of salinity and SSC - this will be explained in section 3.3.1.

3.2.3. Numerical Model: Model Description and Validation

A three-dimensional suspended sediment transport model has been developed using the Finite-Volume Community Ocean Model (FVCOM) for the Changjiang Estuary (CE-FVCOM). FVCOM is an unstructured-grid coastal ocean model. In hor-

izontal directions, a triangle mesh is used; in the vertical, a terrain-following sigma coordinate system (20 equidistant sigma layers) is prescribed. In a previous study [Zhou et al., 2019], a hydrodynamic model with semi-implicit scheme was set up, which well captured the two-layer structure flows and the complex intratidal salinity variation in the North Passage. This application has been extended with a sediment module (FVCOM-SED, [Ge et al., 2015; Wu et al., 2011]).

The suspended load model satisfies an advection-diffusion equation [Chen et al., 2013]:

$$\frac{\partial C_i}{\partial t} + \frac{\partial u C_i}{\partial x} + \frac{\partial v C_i}{\partial y} + \frac{\partial (w - w_i) C_i}{\partial z} = \frac{\partial}{\partial x}\left(A_h \frac{\partial C_i}{\partial x}\right) + \frac{\partial}{\partial y}\left(A_h \frac{\partial C_i}{\partial y}\right) + \frac{\partial}{\partial x}\left(K_h \frac{\partial C_i}{\partial z}\right) \quad (3.1)$$

where C_i is the concentration for sediment i; A_h, K_h represent the horizontal and vertical diffusion coefficients, respectively; w_i is the settling velocity for sediment i; u, v, w are velocity components in $x-$, $y-$ and $z-$directions.

At the bottom, the net sediment flux is the difference between deposition and erosion [Chen et al., 2003; Zheng et al., 2003]:

$$-K_h \frac{\partial C_i}{\partial z} - w_i C_i = E_i - D_i, \ z = -H \quad (3.2)$$

where K_h is the vertical eddy viscosity; H is the depth. The erosion rate E_i is calculated as:

$$E_i = \Delta t Q_i (1 - P_b) F_{bi}\left(\frac{\tau_b}{\tau_{ce}} - 1\right) \quad (3.3)$$

where Q_i denotes the erosive flux; P_b represents the bottom porosity; $F_b i$ is the fraction of sediment i in the bottom; τ_b, τ_{ci} are the bottom shear stress and critical shear stress of sediment i.

This sediment model considers single fraction of sediment with D_{50} of 0.008 mm. Flocculation is not considered in this model, as salt flocculation may play a minor role in the Changjiang Estuary [Song et al., 2013; Guo and He, 2011]. The model is initialized with one meter of sediment in the bed, with a settling velocity of 0.5 mm/s. Hindered settling is modelled using:

$$w_{set} = w_0 \cdot scale \quad (3.4)$$

where w_0 is initial settling velocity, scale is the reduction scale which is set to 0.3. This adjustment for settling velocity operates in the lower 2 layers when the SSC is larger than 2.5 g/L. On the river boundary, the sediment concentration of the river discharge is specified as 0.3 g/L.

Waves are computed using a SWAN model forced with ERA-Interim data from the European Centre for Medium-Range Weather Forecasts. Detailed data source and parameter information are listed in Table 2.

The CE-FVCOM model has been validated against hydrodynamics in previous studies [Zhou et al., 2019; Ge et al., 2015, 2014; Guo et al., 2018a]. Compared to length of groynes (1 ~ 2 km) and groyne fields (~5 km), grid resolution (~200 m) is able to resolve detailed processes, for example, groyne-induced eddies [Ge

Table 2: Data source and model settings.

Data source		
	wind	ERA-Interim data European Centre for Medium-Range Weather Forecasts
	river discharge	www.cjh.com.cn, $1.7 - 2.3 \times 10^4$ m^3/s (Figure 3.2a)
	tidal forcing	TPXO 8 [Egbert and Erofeeva, 2002]
Settings		
	discretization	finite volume, semi-implicit scheme
	grid resolution	minimum: ~200 m in the North Passage
	vertical layer	20 equidistant sigma layers
	internal time step	10 secs
	number of time steps used to ramp the model from the initial field	5000
	vertical Prandtl number	0.4
	horizontal Prandtl number	1.0
	sponge layer at the open boundary	0.0003
	grain size	0.008 mm
	initial settling velocity	0.5 mm/s
	initial bed thickness	1 m
	initial bed porosity	0.5

3

et al., 2012]. Validation of flow velocity, flow direction, and salinity is given in Figure 3.3a-c, respectively. The OBS-measured SSC is used to further validate simulated SSC. A correlation coefficient is computed to quantify the agreement between the model and the data:

$$CC = \frac{cov(X,Y)}{std(X) \cdot std(Y)} \tag{3.5}$$

$cov(X,Y)$ is the covariance of variables X and Y, $std(X)$ is the standard deviation of X. The correlation coefficients of bottom flow velocity, direction, salinity, and SSC are 0.88, 0.96, 0.90, and 0.55, respectively.

The correlation coefficient of SSC is lower than that of the hydrodynamic variables because near-bed sediment dynamics are governed by complex processes and uncertainties in the bed properties. Nevertheless, the main characteristics of SSC are captured by the model, such as the bimodal structure and the pronounced peak around LWS (Figure 3.3d). The bimodal structure of SSC corresponds to the intratidal salinity variation - see the green box in Figure 3.3c - which has been attributed to lateral flows in earlier work [Zhou et al., 2019].
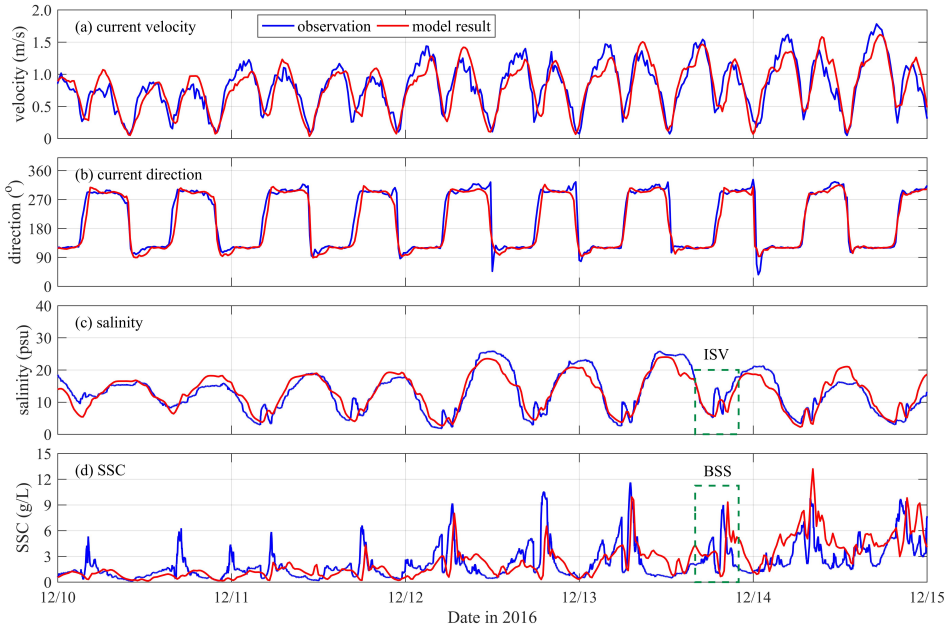
Figure 3.3: Model-data comparison between observed (blue) and simulated (red) results for near-bed current velocity (a), current direction (b), salinity (c), and suspended sediment concentration (d) at the measuring site. The green dashed boxes show a typical intratidal salinity variation and bimodal structure of SSC during LWS, which will be explained in more detail in Figure 3.4. 'ISV' and 'BSS' denote intratidal salinity variation and bimodal structure of SSC.

3.3. Lateral Transport of Suspended Sediment

3.3.1. LWS: Low-Concentration Flows from North Shoal to Channel

The lateral transport during a bimodal-structure-of-SSC period (as identified in the previous section) is investigated in more detail using the numerical model. For this purpose, a typical bimodal structure of SSC observed and modelled on 12/13 - see Figure 3.3d, was selected for detailed analysis. Figure 3.4 shows the near-bottom distribution of SSC during LWS. Near the end of ebb, bottom SSC in the main channel was higher as weak hydrodynamic conditions in the shoal area (marked with white box in Figure 3.4a) provided an environment for sediment to settle (Figure 3.4a). Meanwhile, due to the retention effect of groynes, a high-salinity water mass was trapped in the north groyne fields, forming a high-salinity and low-SSC condition on the north shoal. Instantaneous salinity and SSC of the observational site were 3.8 PSU and 4.3 g/L. Mainly due to the density gradient, a shoal-to-channel bottom lateral flow was generated. The formation of this lateral flow has been introduced in detail in Zhou et al. [2019]. This lateral flow transported saline but low-SSC water to the deep channel, leading to an increase in salinity and a decrease in SSC at the observational site (top-right panel in Figure 3.4b): the

first stage of the intratidal salinity variation and bimodal structure of SSC. At 06:30, 2-g/L SSC contour went through the observational site (Figure 3.4c).
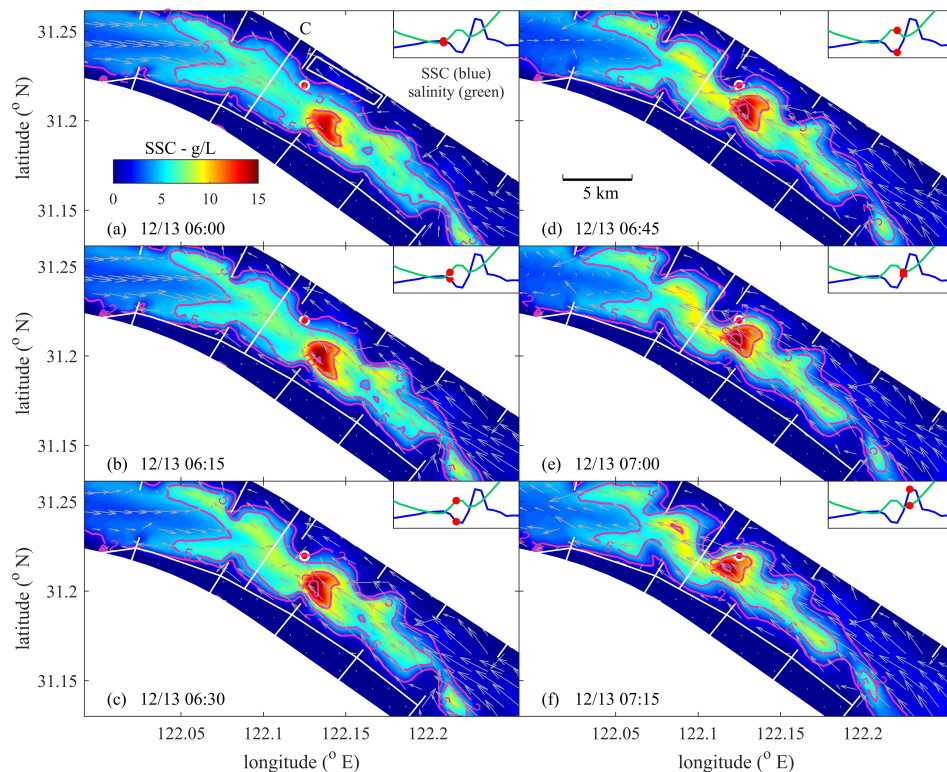
Figure 3.4: Spatial distributions of near-bed SSC at selected times (model result). The red dot indicates the observational site. The up-right inset shows the salinity (green) and SSC (blue); the red dot corresponds to the time of map plot corresponding to the inset. Arrows are near-bed velocities, indicating different stages in the bimodal-structure-of-SSC period. SSC contours of 2, 5, and 10 g/L are given with purple solid lines. The white rectangle in panel (a) indicates the north shoal area.

Near the bed, suspended sediment was mostly transported in the upstream direction due to flood currents. The high-concentration suspended sediment, in which the maximum SSC exceeded 10 g/L, was advected upstream, causing rapid increase of SSC at the observational site (Figure 3.4f). This implies that lateral flows were important for the decrease of SSC in the bimodal structure, the subsequent flood current governed the increase in SSC. The high suspended sediment concentration developed during LWS, due to sediment settling under weak hydrodynamics. This patch could be transported about 10 km upstream to the measuring site. During this process, increasing flow velocities gave rise to vertical mixing [Zhou *et al.*, 2019], this high-concentration suspended sediment could spread to upper layer in the water column. It partly contributes to the ETM formation in the North Passage.

Although small amounts of suspended sediment were directly carried by the

lateral flow from the north shoal, the lateral flow was still important for lateral transport of suspended sediment. This will be explored in more detail in section 3.4.5 (Figure 3.12), together with the discussion about the impact of groynes. In the following section, we expand our analysis to the full tidal cycle in order to explain the origin and fate of the sediment patch.

3.3.2. HWS: Sediment Transport from Channel to South Shoal

During the ebb tide, SSC was highest in the deep channel, and was characterized by a band-like shape (Figure 3.5a). This high-SSC pattern was strengthened by strong ebb currents, developing into a broader high-turbidity band with higher concentration (Figure 3.5b). During LWS, the near-bed sediment concentration attained its maximum while at the same time the regular SSC shape deformed into a wave-like, patchy structure (Figure 3.5c, d). We attribute this deformation to the salinity-driven lateral flows described in section 3.3.1. As these lateral flows originated from high-salinity waters trapped in the groyne fields, the wavelength of these SSC patches corresponded to the length of the groyne fields (~5 km).

During the flood tide (Figure 3.5d-f), the wave-like high SSC reverted to a longitudinal uniform patch, shaped by strong flood currents in the channel (Figure 3.5e). An important feature is that the high-turbidity band was transported to the south shoal (Figure 3.5f) during HWS. The southward transport mechanism is elaborated in detail in section 3.4.3. This transport pattern can be integrated with lateral transport during LWS, attracting more attention to slack-water processes and dynamics. The high-concentration sediment was subsequently transported back to the main channel (Figure 3.5g) and continually transported seaward (Figure 3.5h) by the ebb currents, forming the longitudinal tidal oscillation of the high-concentration suspended sediment in the North Passage.

In summary, during the observation period, two important processes took place, i.e. lateral transport of salt and sediment during LWS (section 3.3.1) and sediment transport to the south shoal during HWS. These lateral exchange mechanisms are very important for the fate of the suspended sediments in the fairway, potentially contributing to net siltation rates.

3.4. Sediment Transport Mechanisms

In this section, by means of a sediment flux decomposition method and a momentum balance analysis, mechanisms for longitudinal and lateral transport of suspended sediment are investigated. In addition, effects of longitudinal sediment transport on sediment convergence in the channel, and effects of lateral sediment transport on deposition rate are also discussed.

3.4.1. Residual Sediment Flux

To explore the relative importance of various physical processes in more detail, the residual sediment flux per unit width is calculated and decomposed following

3
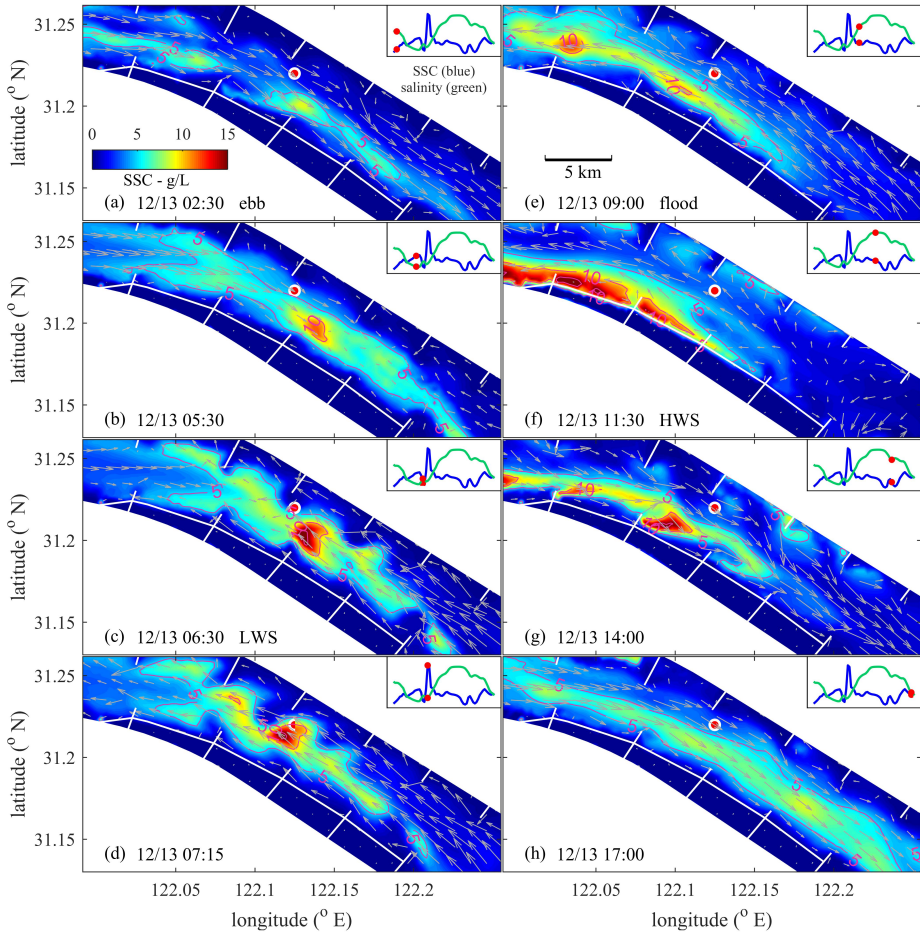
Figure 3.5: Spatial distributions of near-bed SSC in a complete tidal cycle (model result). The red dot indicates the observational site. The up-right inset shows variation of SSC and salinity. Arrows are near-bed velocities, indicating different stages in the tidal cycle. SSC contours of 5 and 10 g/L are given with purple solid lines.

[Dyer, 1988]:

$$\frac{1}{T}\int_0^T\int_0^h uc\,\mathrm{d}z_0 = \frac{1}{T}\int_0^T\int_0^1 huc\,\mathrm{d}z\mathrm{d}t$$

$$= \underbrace{h_0\overline{u_0c_0}}_{T_1} + \underbrace{\langle\overline{u_t}h_t\rangle\overline{c_0}}_{T_2} + \underbrace{\langle h_t\overline{c_t}\rangle\overline{u_0}}_{T_3} + \underbrace{h_0\langle\overline{u_tc_t}\rangle}_{T_4} + \underbrace{\langle h_t\overline{u_tc_t}\rangle}_{T_5} + \underbrace{h_0\overline{u_0'c_0'}}_{T_6} + \underbrace{h_0\langle\overline{u_t'c_t'}\rangle}_{T_7} \tag{3.6}$$

where h is water depth; z is relative depth, $0 \le z \le 1$; u is current velocity; c is sediment concentration; T denotes period of tidal cycle; subscript '0' means tidally averaged whereas 't' means tidally fluctuating; overbars denote depth averages and quotation marks denote a depth-depending term; angled brackets denote tidal averages.

T_1 is the mean flow induced transport, i.e. transport due to Eulerian flow; T_2 is transport due to Stokes drift; together T_1+T_2 represents advection transport. T_3, T_4, T_5 are tidal pumping terms [Uncles et al., 1985a]; T_6 is the transport resulting from vertical circulation which can be interpreted as salinity-driven estuarine circulation; T_7 is transport resulting from lag effects in settling and mixing.

This methodology was applied to decompose sediment fluxes in the North Passage in along- and cross-channel directions. Note that the flux calculated using this method is the vertical integrated flux at a specific location, making point results sensitive to a local variability in SSC and velocity. To avoid local variability, we used results of all locations along specific transects (B, C, and D) where the depth > 10 m. With a typical channel depth of 12.5 m, the depth criterion of 10 m can provide a sufficiently large amount of locations representing deep channel dynamics. The sediment fluxes of the deep channel in both along- and cross-channel directions are shown in Figure 3.6. The jaggedness in Figure 3.6 is related to diurnal inequality in tidal forcing.

From transect B to D, the along-channel flux T_1 (related to processes that have longer timescales than the tide, for example, the river discharge) was dominant (Figure 3.6a-c). The magnitude of T_1 was maximal at spring tide (12/14 ∼ 12/17) and decreased in the seaward direction (from transect B to D). Although the other advection term (T_2, Stokes drift) was directed landward, the total advection flux was seaward (Figure 3.6a-c). Tidal pumping (terms T_3, T_4 and T_5) generated landward sediment transport in the upstream transects B and C, but was not large in the most seaward transect D. The seaward transport due to tidal pumping in section D was because of coupled asymmetry of stratification, sediment resuspension, and tidal currents [McSweeney et al., 2016]. The water column was well mixed during the ebb tide and the stratification was enhanced from the end of LWS throughout the flood tide [Zhou et al., 2019]. As a result, during the ebb tide, more sediment was transported compared to the flood tide due to stronger current velocities, more suspension (because of stronger near-bed velocities), and longer settling time (because of more pronounced vertical mixing). Therefore, asymmetric stratification and current velocities jointly generated an ebb-driven flux. In transect D, landward transport primarily resulted from vertical circulation (T_6). In transects B and C, tidal pumping and vertical circulation both contributed to landward sediment transport.

3
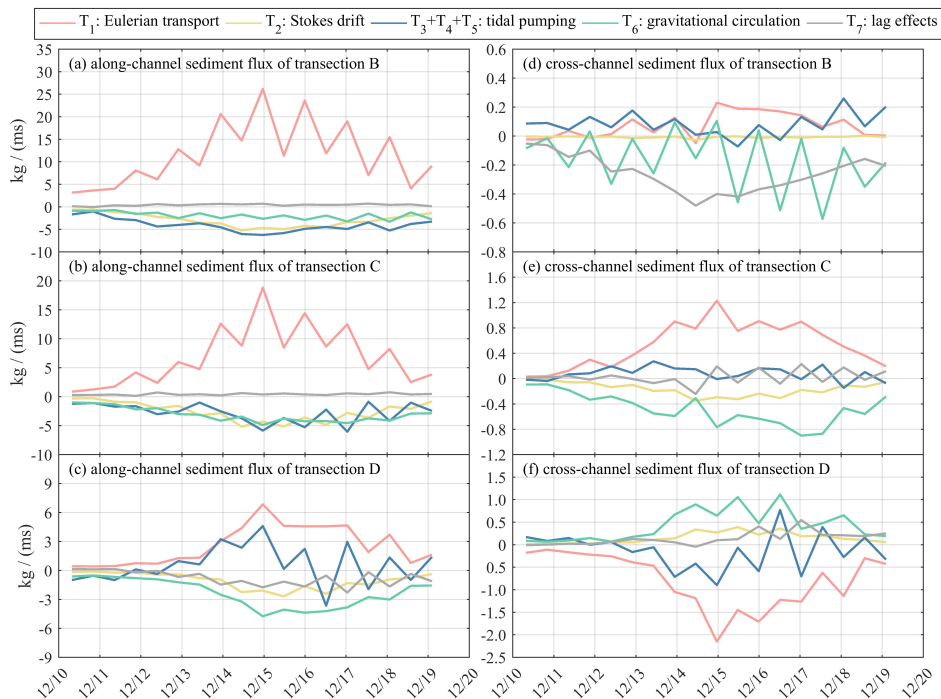
Figure 3.6: Along-channel (left column) and cross-channel (right column) residual sediment flux per unit width of transect B (row 1), C (row 2), and D (row 3). For along-channel flux, positive value indicates seaward transport; for cross-channel flux, positive value indicates transport from the south shoal to the north shoal.

Lag effects (T_7) constitute a minor contribution.

The combined effect of these mechanisms is seaward transport driven by advection in the upstream transect B and landward transport driven by tidal pumping and estuarine circulation in transects C and D (Table 3). This sediment convergence leads to deposition, which will be elaborated in more detail in section 3.4.2.

In the main channel, the cross-channel flux was dominated by advection and vertical circulation in transects C and D (Figure 3.6e, f and Table 3), indicating the important role of lateral circulation in the deep channel. In transect B, T_7 was important (Figure 3.6d), indicating the role of lag effects in settling and mixing, i.e. lag effects of suspended sediment responding to vertical velocity variation [Dyer, 1988]. This different mechanism at transect B may be related to the channel curvature. The curvature radiuses of transects B and C are about 28 and 50 km, respectively, leading to a 2 times larger curvature induced momentum term (and resulting in different lateral flow structures) at transect B than C [Zhou et al., 2019]. For transects B and C (located in the channel bend), vertical circulation (T_6) resulted in a sediment flux towards the south shoal. Nevertheless, in transect D, T_6 was directed towards to the north. An important reason is position of transect D is close

Table 3: Decomposed sediment flux per unit width in along-channel and cross-channel directions on three transects (unit: $kg/(m \cdot s)$).

	$T_1 + T_2$	$T_3 + T_4 + T_5$	T_6	T_7	sum
B_{along}	8.81	-4.04	-1.92	0.43	3.28
C_{along}	4.40	-2.77	-3.13	0.44	-1.06
D_{along}	1.51	0.59	-2.33	-0.77	-1.00
B_{cross}	0.07	0.08	-0.17	-0.26	-0.27
C_{cross}	0.37	0.08	-0.48	0.03	0
D_{cross}	-0.64	-0.13	0.43	0.14	-0.21

Zero value in this table is because of approximation.

3

to the seaward limit of salt wedge during the ebb tide. Therefore, although the north groyne field also had a retention effect as the groyne field near the observational site, however, the density gradient between the north shoal and the main channel was small. The regular southward lateral flow did not occur in transect D. Advection balanced the vertical circulation in transect C, whereas it exceeded the vertical circulation term in transect D. Combined, transport was directed southward in transects B and D, but negligible at transect C.

3.4.2. Sediment Accumulation in the North Passage

In this section, we further estimate the sediment accumulation in the North Passage resulting from longitudinal transport. The cumulative sediment transport (unit: kg) through a transect is calculated as:

$$T = \sum_{t_0}^{t} c \cdot vel_n \cdot b \cdot d \tag{3.7}$$

where vel_n represents the cross-transect velocity; b, c, d are width, SSC, and height of each computational cell; t_0 and t denote the start and end time of the calculation. Here we define velocity in the ebb current direction as positive, thus mass increasing of sediment (unit: kg) of an area enclosed by transect P (landward) and Q (seaward) can be estimated as:

$$M = (T_P - T_Q) \tag{3.8}$$

$M > 0$ indicates there is net sediment accumulation (mass increasing) in this area. The area between transect B and C (abbreviated as S_{BC}) is the curved area of the channel, where sediment was trapped during the whole observation period (Figure 3.7). Within in the 10-day period, the net sediment accumulation was about 3.3 million tons. S_{CD} is the straight part of the channel, which was losing sediment from 12/12 to 12/15, then recovering between 12/15 and 12/18. Overall, this area lost 0.8 million tons of sediment in the 10-day period (Figure 3.7). The whole section
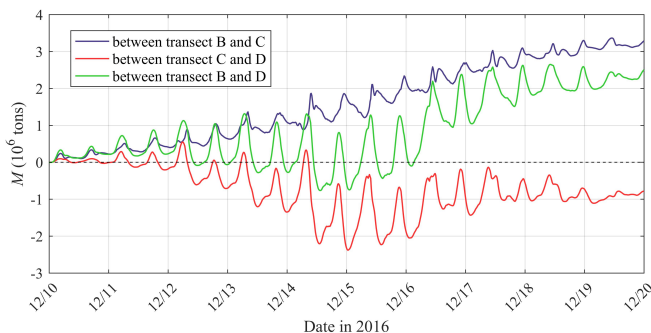
Figure 3.7: Sediment mass accumulated in the three areas enclosed by transect B, C (blue line), transect C, D (red line), and transect B, D (green line).

S_{BD} suffered from net sediment accumulation, mostly happened in the curved part of the channel.

The computed converging sediment mass can be compared to dredging data, to further evaluate the accuracy of the model. The density of dredged sediment is about $500 \sim 1000 \, kg/m^3$ [Fettweis et al., 2006], which means that in 10 days about $2.5 \sim 5$ million m^3 accumulated. This corresponds to $91 \sim 182$ million $m^3/year$ when linearly extrapolated (assuming the dredging work aims at maintaining the depth of the channel). This is more than the dredging amount in 2016 between transects B and D (about 44 million m^3) but provides a reasonable order of magnitude, which is also a validation of this model. The overestimation may be the result of storm conditions [Hu et al., 2009; Nowacki and Ganju, 2018] occurring during the modelled period, with a strong north wind from 12/13 onwards leading to a maximum (observed) significant wave height exceeding 0.8 m. Strong wind and its induced wave height are important for sediment re-suspension and transport outside the channel, which is subsequently transported back into the channel. Additionally, a short modelled period (as in our case) insufficiently accounts for feedback mechanisms between the flow and the bed: when deposition rates are too large the flow velocities become larger, and less sediment deposits. More sediment accumulation in the curved part (between transect B and C) compared to the straight part (between transect C and D) indicates different influence of groynes in the curved or straight part of the channel, requiring more research on the groyne layout. Here we do not compare sediment accumulation to bed level changes from bathymetry surveys, because (1) we lack in-situ observation of intratidal bed level changes, (2) bathymetry surveys cannot reflect actual sediment accumulation as the frequency of dredging work (daily to monthly) is higher than frequency of bathymetry surveys (seasonally to yearly).

3.4.3. Slack-water Dynamics

Model results presented in section 3.3.2 revealed a clear pattern of sediment transport to the south shoal during HWS, particularly around the curved part

of the channel. Here, we further analyze the driving mechanisms for this channel-to-shoal transport through a momentum balance analysis. The governing equation for the lateral flow is:

$$\underbrace{\frac{\partial v}{\partial t}}_{A} + \underbrace{u\frac{\partial v}{\partial x} + v\frac{\partial v}{\partial y} + w\frac{\partial v}{\partial z}}_{B} + \underbrace{fu}_{C} = \underbrace{-\frac{1}{\rho}\frac{\partial (P_H + P_a)}{\partial y}}_{D} + \underbrace{\frac{\partial}{\partial z}\left(K_m\frac{\partial v}{\partial z}\right)}_{E} + \underbrace{F_y}_{F} \quad (3.9)$$

where x, y and z represent along-channel, cross-channel and vertical directions in the Cartesian coordinate; u, v and w are components in x, y, and z axes, respectively; ρ is density; P_H is hydrostatic pressure; P_a is the air pressure; f is the Coriolis parameter and K_m is vertical eddy viscosity coefficient; F_y represent the horizontal momentum diffusion terms in y direction. The hydrostatic pressure P_H satisfies:

$$\frac{\partial P_H}{\partial z} = -\rho g \;\Rightarrow\; P_H = \rho_0 g\zeta + g\int_z^0 \rho\,\mathrm{d}z \quad (3.10)$$

where g is the gravitational acceleration. In Eq 3.9, $A - F$ are local acceleration, advection, Coriolis force, pressure gradient, vertical diffusion, and horizontal diffusion. The Coriolis force and pressure gradient terms on transect B are shown in Figure 3.8, with positive values indicating flows from the deep channel to the north shoal. The density effect of sediment was not included in this model, neither in this momentum balance analysis.
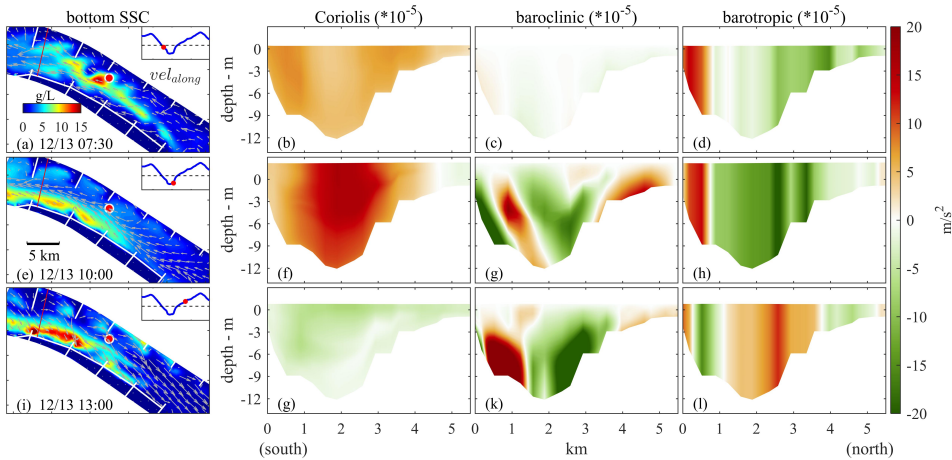
Figure 3.8: Momentum balance analysis of transect B (Figure 3.1). Coriolis term (b, f, g), baroclinic pressure gradient term (c, g, k), and barotropic pressure gradient term (d, h, l) of early stage of flood tide (a), late stage of flood tide (b), and early stage of ebb tide (c). The red line represents transect B and the red dot is the observational site. The up-right inset shows along-channel velocity to indicate stage in a tidal cycle, positive values denote downstream (ebb) currents.

To unravel driving forces for southward sediment transport during HWS and its movement back to the main channel during the early ebb tide, we select three typical moments for analysis (first column in Figure 3.8).

During the early stage of flood tide (Figure 3.8a), the Coriolis force term (with a magnitude of $4 \sim 6 \times 10^{-5}\ m/s^2$ in the main channel) was towards the north shoal on transect B (marked with red line in Figure 3.8a). The total pressure gradient force was weaker in the channel, with a value of $-1 \sim -4 \times 10^{-5}\ m/s^2$. At this moment, as the flood current had not affected transect B, the salinity (also density) was laterally uniform, and therefore the baroclinic pressure gradient was weak (Figure 3.8c). The barotropic pressure gradient was the main contributor (Figure 3.8d), because the flood currents deflected to the north shoal and raised the water level on the north side.

Later in the flood tide (Figure 3.8e), the total pressure gradient force reached $-3 \times 10^{-4}\ m/s^2$ in the deep channel, while the Coriolis force was about $1 \sim 2 \times 10^{-4}\ m/s^2$. The difference between these two terms was around $10^{-4}\ m/s^2$, which is able to generate a lateral flow in this channel [Zhou *et al.*, 2019]. This explains the sediment transport to the south shoal during HWS. Moreover, the combined baroclinic and barotropic pressure gradient terms contributed equally to the strong momentum towards the south (Figure 3.8g, h).

During the early stage of ebb tide (Figure 3.8i), a high-SSC water patch on the south shoal started to move back to the main channel, driven by a high positive pressure gradient on the south shoal (about $3 \times 10^{-4}\ m/s^2$). Furthermore, the baroclinic pressure gradient was the main contributor to the pressure gradient term (Figure 3.8k) as the salt had been transported to the south and the density effect of salinity was more important than the lateral difference of water level.

To demonstrate the importance of the baroclinic pressure gradient (i.e. the salinity-induced density effect), we simulated a barotropic scenario in which salinity of sea water was set to zero. Model results shows the distribution of bottom SSC (Figure 3.9a) did not have the same wave-like, patchy structure found in the original case (Figure 3.9c), supporting our earlier conclusion (in section 3.3.2) that the wave-like structure resulted from salinity-driven density currents. More importantly, the sediment transport to the south shoal during HWS also weakened (Figure 3.9b) compared to the original case (Figure 3.9d). This difference resulted from the baroclinic pressure gradient. However, the distribution of bottom SSC still showed a weak southward deflection (Figure 3.9b) because of the channel curvature and configuration of groynes.

Because transect B is in the channel bend, curvature-induced momentum (de-fined as $\frac{u_s^2}{R}$ in a curvilinear coordinate system) could be important. Here, u_s is the longitudinal velocity magnitude and R is the radius of curvature. For transect B, R is about 28.7 km in the deep channel. The maximum flood current velocity was about 1.6 m/s at the bottom and 2.2 m/s at the surface. This term was about $8.9 \times 10^{-5} \sim 1.7 \times 10^{-4}\ m/s^2$ from the bottom to the surface during flood maxi-mum, towards the north side of the channel. The vertical differences of this term could result in a clockwise (originating from the flood current) lateral circulation and enhance the southward transport of sediment in the bottom layer. This explains the weak southward deflection in Figure 3.9b.

The curvature-induced centrifugal force was strongest during maximum flood and declined with the decrease of the flood current. During HWS, this term was
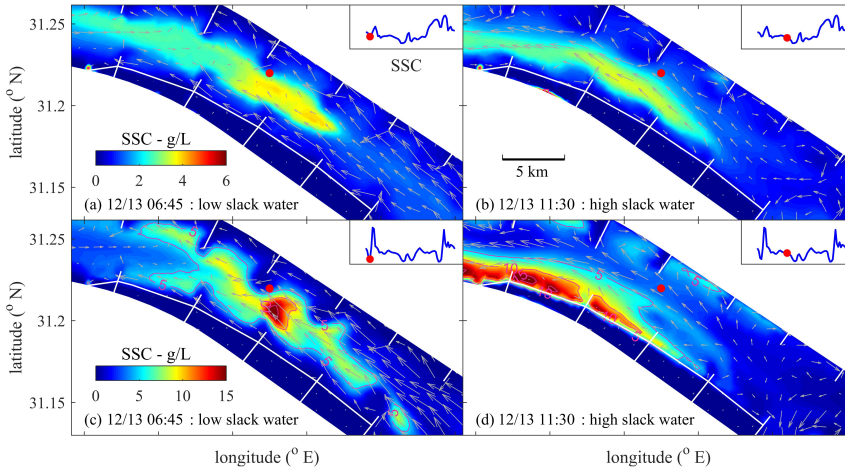
Figure 3.9: A comparison between a barotropic scenario (a, b) and the original (baroclinic) scenario (c, d, same with results in Figure 3.4 and 3.5. Spatial distributions of near-bed SSC and flow velocity during LWS (a, c) and HWS (b, d) in the new non-salinity scenario (a, b) and the original scenario (c, d). Arrows are near-bed velocities, indicating different stages in the tidal cycle. SSC contours of 5 and 10 g/L are given with purple solid lines. The red dot is the observational site.

small because of the weak current, however, its accumulated effect during the whole flood tide still contributed to the near-bed southward sediment transport. In summary, the southward sediment transport during HWS was mainly caused by the combined baroclinic and barotropic pressure gradient. This southward lateral transport is further illustrated for transect A (Figure 3.10). The averaged lateral transport flux indicates an overall transport from the deep channel to the south shoal. For example, the averaged flux from 12/13 to 12/14 was about -0.82 $kg/(m \cdot s)$. During this period, the maximum flux towards the south shoal was about -4.9 $kg/(m \cdot s)$, which was about 2.6 times the maximum flux towards the deep channel (about 1.9 $kg/(m \cdot s)$). The maximum flux towards the south shoal all occurred during HWS (Figure 3.10), in agreement with our emphasis on southward transport of suspended sediment during this period. Subsequent effects of the southward transported suspended sediment are investigated in the following section.

3.4.4. Deposition during HWS

Computed bed level changes reveal that the channel eroded during peak flow conditions, whereas deposition prevailed during slack tide conditions (Figure 3.11). It also shows that deposition was persistent in the groyne fields (to the south as well as to the north). However, most striking is the accumulation rate of sediments on the south shoal during HWS (Figure 3.11b).

Pronounced southward lateral transport results from the barotropic and baroclinic pressure gradients (Section 3.4.3). In this section we investigate deposition potential in more detail and discuss the effect of the southward sediment transport

3
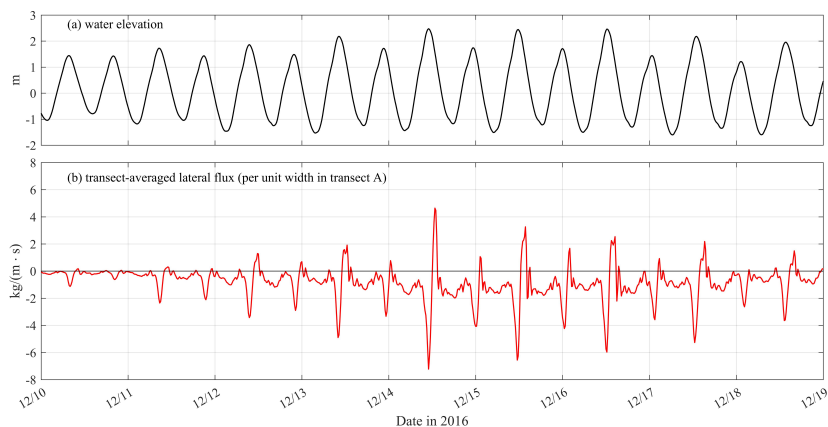
Figure 3.10: Water elevation (a) at a site (122.0945° E, 31.2082°N) in transect A (the along-channel transect that encloses two groyne fields on the south shoal in Figure 3.1 and transect-averaged lateral transport flux of suspended sediment in transect A (b), positive value indicates transport from the south shoal to the north shoal.
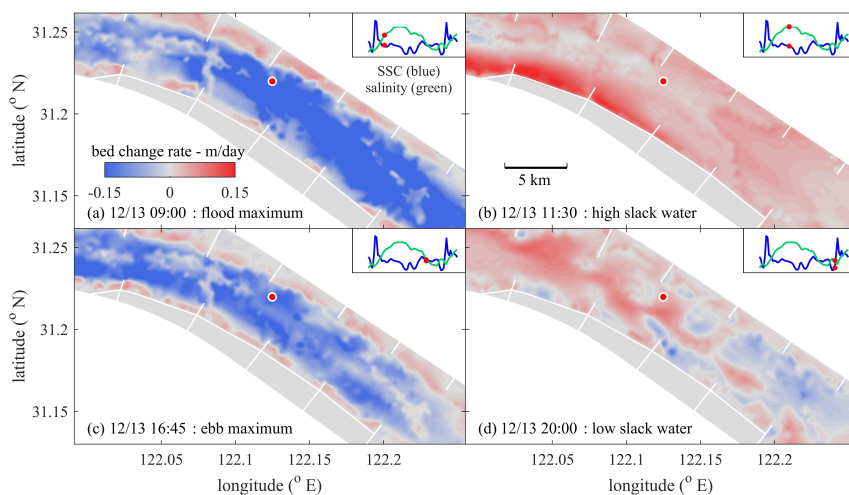
Figure 3.11: Distribution of bed level change rate (m/day) in the channel. Positive values (red) indicate deposition. The up-right inset shows variation of SSC and salinity.

during HWS. Sediments are kept in suspension by turbulent motions, and especially for sediments with a considerable settling velocity, absence of turbulence leads to rapid deposition of sediments. Even more, steep sediment concentration gradients suppress turbulent mixing, which leads to faster settling, in turn further decreasing turbulent mixing [Winterwerp, 2001, 2006]. We therefore analyze the water column stability with a Bulk Richardson number. The bulk Richardson number R_{ib} is calculated as:

$$R_{ib} = \frac{gD\Delta\rho}{\rho_w \left|\overrightarrow{u_s}^2\right|} \tag{3.11}$$

where D represents water depth; $\Delta\rho$ denotes bottom-surface density difference; $\overline{\rho_w}$ is vertically averaged density; $\overrightarrow{u_s}$ is surface current velocity. Figure 3.12 shows the result of $\log_{10}(R_{ib}/0.25)$, positive values indicating stratifying conditions.
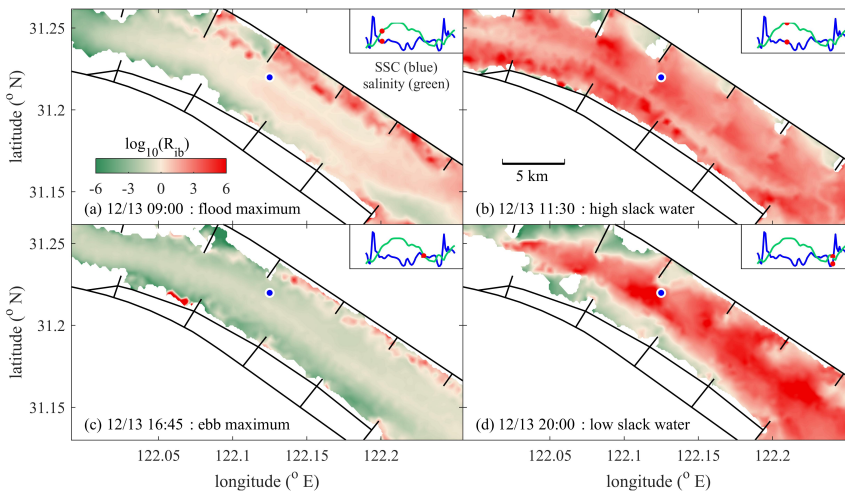
Figure 3.12: Distribution of bulk Richardson number ($log_{10}(R_{ib}/0.25)$) in the channel. The up-right inset shows variation of SSC and salinity. The blue dot is the observational site. The blank area is because of negative R_{ib} when converted to a logarithm.

During peak flood flow, the whole water column was slightly stratified in the main channel (Figure 3.12a), whereas stronger stratification dominated over the north shoal. During HWS (when sediment was transported to the south shoal - see Figure 3.5f), the area with high deposition rates (Figure 3.11b) was highly stratified (Figure 3.12b), showing a high probability of enhanced sediment accumulation on the south shoal. During the ebb maximum, the main channel showed a well-mixed condition due to great surface current velocity (Figure 3.12c). During LWS, the main channel was dominated by strong stratification (Figure 3.12d), and the stratification showed a patched-like pattern, i.e. stratification was stronger in the main channel and weaker in groyne fields.

Sediment was regularly transported southward during HWS (showed in section 3.3.2 and explained in section 3.4.3. Although during early ebb, part of the sediment

would be transported back to the main channel, modelled bed level changes and water column stability still indicate the deposition potential and accumulation effect due to this transport pattern.

3.4.5. Effect of Groyne Removal

The decomposed residual transport terms (section 3.4.1) illustrated the importance of lateral circulation (term T_6 in Figure 3.6d-f) to lateral transport of suspended sediment, especially at transect C. Transect C is close to a north groyne and is heavily affected by the regular lateral flow during LWS. To demonstrate the influence of groynes, the nearest groyne to the observational site was removed in the model. Earlier work (Figure 14 in Zhou *et al.* [2019]) showed that such removal strongly reduced lateral flow during LWS. By keeping or removing the nearest groyne, we therefore have two cases with (case 0) or without (case 1) lateral flow during LWS, which can be used to quantify the effect of this groyne-induced impacts on lateral flow and sediment transport. Removing all groynes would greatly influence the overall flow patterns, leading to substantial change in longitudinal processes, and these longitudinal changes also influence lateral flows and sediment transport. However, removing one single groyne helps to keep the overall flow field and allows detailed analysis of effects of groynes on lateral processes. Besides, since the retention effect of groynes on salinity is not obvious on the south side (Figure 3.13a), the south groyne removed case is not conducted in this study. The removed groyne is about 1.52 km, and it is connected with 8 grid cells. This grid resolution is enough to resolve effects of this groyne.

In this section, near-bottom residual sediment flux at the observational site is calculated for case 0 and case 1 to explore effect of this lateral flow on sediment transport pattern, following [Uncles *et al.*, 1985b]:

$$\langle u \cdot c \rangle = u_0 c_0 + \langle u_t c_t \rangle \tag{3.12}$$

where definition of bracket, subscript '0' and 't' are the same with that defined in Eq 3.6. $u_0 c_0$ denotes the advection transport due to residual flow, $\langle u_t c_t \rangle$ is transport due to tidal pumping.

In the along-channel direction, advective transport becomes weaker when the groyne is removed (case 1) although transport patterns for these two cases is similar (Figure 3.13c). This is because the groyne has the effect of regulating flows, which could enhance current velocity and benefit advective transport. However, as only one groyne is removed in case 1, the impact of this adjustment is relatively local, and will not cause substantial difference to the overall flow field, especially to the longitudinal currents, supporting the reason for removing one single groyne. Differences of tidal effects term between case 0 and case 1 are also not important for the same reason. The influence of only one single groyne becomes important, however, in the cross-sectional direction (Figure 3.13d). Values of the advective transport term increases for case 1, indicating a decrease of north-shoal-to-channel residual transport. For case 0, the advective transport is negative for the most time; while in case 1, half of tidal cycles have a positive advective term, i.e. an opposite flux (channel-to-shoal). This effect is also observed in the tide-induced
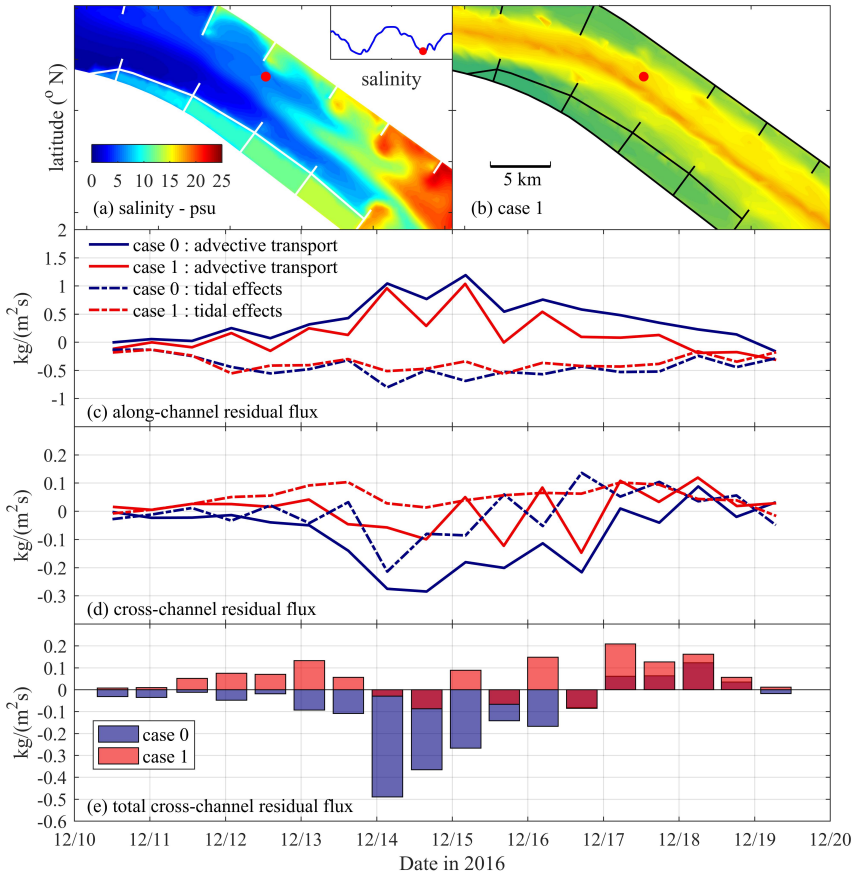
Figure 3.13: Numerical cases setting and single-point residual sediment flux, case 0: standard case with near-bed salinity distribution during low water slack (a); case 1: the groyne nearest to the observational site is removed, marked with white rectangle (b); decompositions of residual flux at the observational site in along-channel (c) and cross-channel (d) direction; and difference of cross-channel residual flux between case 0 and case 1 (e). The positive value in (c) indicates direction of about 120 degrees from the north, the positive value in (d) indicates direction of about 30 degrees from the north.

transport term (Figure 3.13d), which is significantly increased by the adjustment of the groyne. With one groyne removed, the tide-induced transport is positive for most of the period, indicating a continuous channel-to-shoal residual transport. Removing one groyne could reduce effects of groynes on narrowing the channel and strengthening currents, leading to tidal flow easier to flush into the groyne field. The net effect of this groyne adjustment on total cross-channel residual flux ($\langle u \cdot c \rangle$) is shown in Figure 3.13e. After the nearest groyne is removed, the north-shoal-to-channel residual transport decreases, and in some tidal cycles the residual transport even changes in direction. This result shows effects of groynes on lateral transport of suspended sediment and these effects include the lateral flow during LWS and the consequent effect on lateral sediment transport.

The lateral flow develops close to the north groynes and seems to be site specific. However, this process is important near every north groyne in the straight part of the channel, and therefore the total effect is significant. On the other hand, the lateral flow during LWS is caused by salinity retention in the groyne fields, and this retention effect is determined by groyne dimensions, including the length, height of groynes, and distance between them. In this study, the retention effect is observed in the north part of the channel. However, we believe it can also occur near south groynes if their length is increased. Moreover, the radius of the channel is also important for the asymmetric features between north and south shoals. These hypotheses will be investigated in future studies.

3.5. Discussion

Numerous studies about siltation issues have been conducted, focusing on (1) mechanisms for longitudinal convergence of sediment, including ETM dynamics [Burchard *et al.*, 2018]; (2) lateral circulation and consequently induced sediment trapping [Chen *et al.*, 2020; Yang *et al.*, 2014b]; (3) vertical processes in sediment dynamics, including settling and resuspension [Ge *et al.*, 2018; Dankers and Winterwerp, 2007]. This research provides some new information about sediment transport, which is important to deposition issues in a highly-silted channel-shoal system. We report and stress the importance of lateral transport of suspended sediment during HWS and LWS (section 3.3) in the North Passage, and explain the driving mechanism (section 3.4.3) and deposition potential (section 3.4.4) of sediment transport during HWS. For LWS conditions, we explain the formation of bimodal structure of SSC (section 3.3.1) and demonstrate the effect of this lateral transport on residual flux (section 3.4.5). Except for slack-water dynamics, knowledge about impact of groynes is also extended. The presence of groynes significantly affects lateral flows, distribution of high-concentration suspended sediment, and lateral transport patterns (section 3.3.1 and section 3.4.5). Removing one groyne can reduce the lateral flow and sediment transport flux at the observational site during LWS. However, removing multiple groynes may change the overall flow dynamics in the North Passage and South Passage, and therefore determining the overall effect of groynes on transport requires additional research.

Lateral transport of suspended sediment and mass exchange have been studied extensively as part of earlier work. Geyer *et al.* [1998] unraveled a channel-to-

shoal transport mechanism related to lateral salinity gradient caused by differential advection of the longitudinal salinity gradient. Additionally, Huijts *et al.* [2006] applied a two-dimensional idealized model and emphasized the importance of lateral density gradients which usually induce more sediment transport than Coriolis force in estuaries. The present study further supports the importance of lateral salinity gradient to sediment transport, and particularly focuses on lateral salinity gradient during high and low water slack. Zhou *et al.* [2019] reported a salinity-induced density gradient and the lateral flow thereon due to retention of high-salinity water by groynes. This companion study further investigated the lateral sediment transport due to this lateral flow during LWS, and also expanded findings to lateral process during HWS, extending our understanding of slack-water dynamics. Slack-water dynamics are important because the weak hydrodynamics during slack water conditions are suitable for sediment settling and deposition, which can greatly influence channel morphology. Bed level change rate demonstrates that large amount of sediment deposition could occur on shoals during high and low water slack. Therefore, findings presented here provide important insights into siltation issues in channel-shoal systems.

Groynes are most commonly used in low-land rivers and coastal zones, but they are also used in estuaries for example, the Changjiang Estuary, the Ems estuary [van Maren *et al.*, 2015], and the Weser estuary [Hesse *et al.*, 2019]. These systems are all confronting severe siltation. However, in none of these areas the role of groynes in relation to lateral exchange mechanisms has been thoroughly investigated. Groynes are designed to accelerate the flow in navigation channels, thereby reducing channel siltation. The work presented here suggests that the role of groynes is much more complex in stratified estuarine environments, as (1) salinity gradients can complicate the effect of groynes and (2) existence of groynes can affect salinity gradients. Therefore, their design in estuarine environments may need to be revisited. Although our findings indicate a groyne-induced mechanism that can enhance the lateral transport of suspended sediment from the north shoal to the main channel, it is only one of the potential effects of groynes. Other effects are also important and may have opposite influences on sediment transport. For application and evaluation of groynes in estuaries, more studies are needed.

3.6. Conclusions

By means of in-situ observations and a validated high-resolution unstructured-grid sediment transport model, this paper studies the lateral transport of suspended sediment in a tidal channel-shoal system. The model also demonstrates the effect of groynes on hydrodynamics and sediment dynamics.

The model results showed that high-concentration suspended sediment layer with the maximum SSC exceeding 10 g/L occurred in the channel. In the longitudinal direction, the ETM resulted from convergence of sediment by river flow on one hand, and a combination of tidal pumping and estuarine circulation (both equally important) on the other hand. During the late stage of flood tide, the high-concentration suspended sediment layer moved from the channel towards the south shoal, resulting in highly-stratified conditions on the south shoal. A momen-

tum balance analysis revealed that this southward flow and sediment transport was primarily driven by the pressure gradient force. Sediment was deposited on the south shoal because of strongly stratified conditions, leading to suppression of turbulent mixing. During LWS, the existence of groynes triggered a north-shoal-to-channel lateral flow. These sediment transport mechanisms operating during HWS and LWS highlight the importance of slack-water dynamics when addressing on siltation issues in channel-shoal systems. River discharge was in the range of $1.7 \sim 2.4 \times 10^4 \ m^3/s$ (continuously decreasing during the study period), the effects of this fluvial component were limited during the dry season. However, the fluvial component can greatly impact tidal dynamics and riverine sediment supply in the wet season.

Our results also showed that groynes are important for lateral sediment transport in this system. Groynes can show retention effects on salinity during the ebb tide. By affecting the flow field and the salinity distribution, groynes can lead to a shoal-to-channel lateral flow and enhance lateral sediment transport, impacting the sediment re-distribution in the cross-channel direction. This mechanism plays a role in $4 \sim 5$ groyne fields on the north side of the North Passage. Findings in this study indicate a new mechanism for groyne-induced enhancement of lateral transport of suspended sediment from the north shoal to the main channel. Groynes are widely used all over the world for preventing siltation rates in navigation channels (riverine most). Yet, the impact of groynes on hydrodynamics and sediment issues, especially in estuarine environments where salinity gradient is widespread, still need to be further investigated.

4

Using Field Observations to Estimate Erosion and Deposition Fluxes

Abstract

The Krone-Partheniades (K-P) framework has been used for decades for simulation of the morphological evolution of a water-bed interface. The input parameters for the K-P equations are obtained from a limited number of time-consuming field observations, and are usually considered as temporally constant. In this study, continuous erosion and deposition fluxes are estimated based on field observations and converted into time-varying K-P input parameters. For this purpose, two in-situ observations with a tripod system were conducted in the North Passage and the South Passage of the Changjiang Estuary (China). Detailed analysis of the data using the K-P equations provides the variability of the erosion and deposition parameters, and their mutual dependence. Assessing their mutual dependence provides a visual representation of the performance of the K-P model in its parameter space, indicating all possible parameter sets for the bed level simulation. However, in-situ observations also indicate the limitation of a primitive K-P formula with constant parameters, i.e. it cannot reflect the observed change of sediment erodibility. This limitation is especially important when simulating bed level changes in time scales from tidal cycles to episodic high energy events, reflected for example in a continuous deposition observed in the South Passage in 2018. The proposed method is used to explain the reason for this limitation, and provides an example to optimize the constant erosion parameters.

4.1. Introduction

The well-known Krone-Partheniades (K-P) bed level change model and its varied versions [Ariathurai, 1974; Krone et al., 1962; Partheniades, 1965; Winterwerp and van Kesteren, 2004] provide a theoretical framework for quantifying erosion and deposition processes, which is widely applied to quantify bed level changes in cohesive sediment environments. Some aspects of the K-P model are still open for discussion, for example, Sanford and Halka [1993] and Winterwerp [2007] suggests that deposition should always take place, i.e. the Krone equation is incorrect; while the setting of a deposition threshold is also widely used and achieved good results in bed level change models [Lumborg, 2005; Zhu et al., 2014, 2017]. Despite these different opinions, the simple set of equations provide a robust methodology to analyze bed level dynamics. As such they are widely applied in numerical models to quantitatively describe the morphodynamics of muddy environments. These studies have greatly enhanced our understanding of water-bed exchange, but accurately reproducing or predicting bed level changes remains challenging. This is related to three problems: (1) the assumption of constant input parameters, (2) the difficulty in measuring these input parameters, and (3) and optimization via model calibration does not result in a unique set of the input parameters.

The complexity of most physical environments implies that the parameters in the K-P formula related to erosion and settling are variable in time. Numerical models applying the K-P equations usually assume constant input parameters [de Nijs and Pietrzak, 2012; Sanford and Halka, 1993; Dijkstra et al., 2019; van Maren et al., 2009] although they can be spatially varied [Ge et al., 2015] or time-varying by applying a consolidation model [Sanford, 2008; Winterwerp et al., 2018; Zhou et al., 2016]. Use of a consolidation model requires a large amount of additional model input parameters related to the geotechnical properties of the sediment, which also further complicates their simple application. Disregarding consolidation models (for their extensive input data requirement) the simple approach of constant input parameters violates the reality of time-varying sediment and bed properties. Moreover, when investigating bed level response to episodic high energy events, for example, river flood or storm events, net bed level changes become so large that the variability of sediment properties (within the bed) becomes more important. In these cases, constant parameters may not suffice.

The second problem is that obtaining accurate input data for numerical models is time-consuming, and only a limited number of observations can be conducted for parameter determination. Furthermore, data on deposition and erosion fluxes are obtained using different methodologies which may cause disunity of parameters. Numerous studies have been conducted to measure and estimate settling velocity of sediment in the field or in laboratories (e.g. Dyer et al. [1996]), including measurements with settling tubes [Jones and Jago, 1996], acoustic backscatter systems [Maa and Kwon, 2007] often with LISST instruments [Fugate and Friedrichs, 2002; Williams et al., 2004], and video camera systems [Fennessy et al., 1994; Manning and Dyer, 1999; Sternberg et al., 1996; van Leussen and Cornelisse, 1996]. Based on in-situ or laboratory data, some empirical or semi-empirical formulas for settling velocity have been proposed [Cheng, 2009; She et al., 2005]. However, due to

the inadequate data and discrepancies between laboratories and natural environments, it is still difficult to obtain accurate sediment settling velocity [Ahrens, 2000; Nasiha and Shanmugam, 2018]. Moreover, flocculation processes and hindered settling can greatly impact settling velocity [Winterwerp, 2011], which are difficult to reproduce in laboratories. Erosion parameters are measured with a range of methodologies, for example, using sediment samples to measure water content and estimate the erosion threshold [Zhu et al., 2017; Shi et al., 2018] with equation proposed by [Taki, 2000]. In-situ erosion measurements are logistically very difficult to conduct (especially in deep water), and erosion parameters based on sediment samples typically provide a bulk erosion parameter without any temporal variation. As a result of the complexities in obtaining erosion and deposition flux parameters, timeseries of simultaneous erosion and deposition parameters cannot be derived from conventional techniques.

A third problem especially encountered during numerical model setup is the equifinality (or non-uniqueness) of the deposition and erosion flux parameters - see van Maren and Cronin [2016]. Multiple parameter sets of erosion and deposition may exist, each of which providing comparable net bed level changes, but with different response to extreme conditions or intratidal variability. Equifinality increases the uncertainty and decreases the reliability of models. However, the impact of this non-uniqueness on the applicability of the K-P model is rarely studied in the literature.

In this study, we conducted in-situ observations with a near-bed tripod system in the North Passage (Jul, 2017) and the South Passage (Jan, 2018) of the Changjiang Estuary. These two data sets show different trends of bed property variations, which are helpful to obtain a more all-sided understanding of water-bed exchange. Based on observations, we (1) develop a method to estimate erosion and deposition fluxes simultaneously, (2) evaluate the validity of constant parameters in the K-P model and optimize the parameters, and (3) propose a visualization method to provide the parameter space which includes all possible parameter sets.

4.2. Study Site and Methodology

4.2.1. Study Site

The Changjiang Estuary is a meso-tidal estuary, dominated by irregular semi-diurnal tides with a mean tidal range of about 2.7 m. The average wet season river discharge is about 40,000 m^3/s but may exceed 70,000 m^3/s during flood events. Due to the construction of the Three Gorges Dam (TGD) in 2003, the sediment load from the Changjiang River at Datong has declined from about 420 million tons per year in 1950 - 2002 (pre-TGD) to about 150 million tons per year in 2003 - 2010 (post-TGD) (Dai and Lu [2014], data soure: CWRC, http://www.cjh.com.cn/). The main navigation channel in the estuarine turbidity maximum (ETM) zone of the Changjiang Estuary is the North Passage (NP). Although the sediment load is reduced by construction of the TGD, the suspended sediment concentration (SSC) in the NP can still be up to tens of kg/m^3 in the form of concentrated benthic suspension [Ge et al., 2018]. High current velocities in the flood season and high SSC
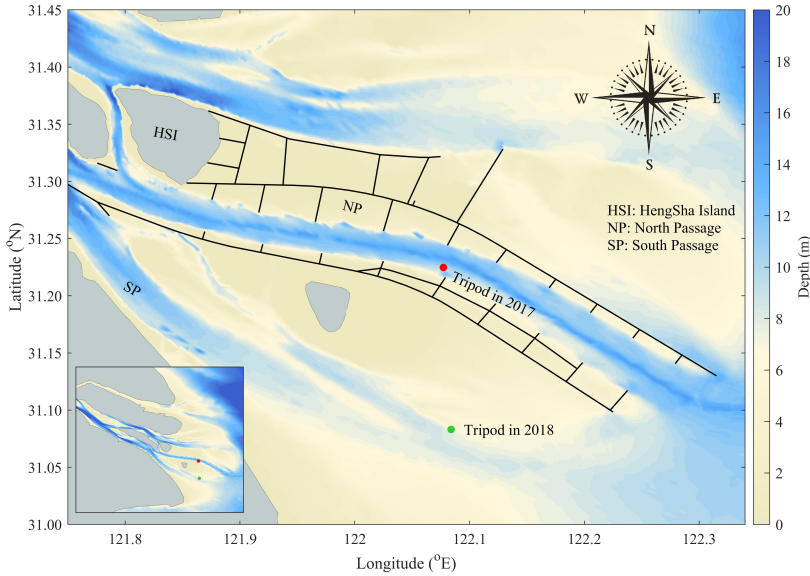
Figure 4.1: Bathymetry of the North Passage and adjacent regions. Black lines in the river mouth represent dikes and groynes around the North Passage. Red dots indicate the measuring site in 2017 (primary data set); green dots indicate the measuring site in 2018 (additional data set). The inset shows the bathymetry of the whole Changjiang Estuary.

result in active sediment exchange between the bed layer and the water column hence large bed level changes. In contrast, the South Passage (SP) is shallower, and experiences relatively weaker flow velocities in the dry season, probably resulting in slow bed level changes. The different hydrodynamic conditions and bed level dynamics of these locations provide the opportunity for comparative investigation on bed level dynamics within the K-P model framework. Therefore, observations were conducted with a tripod system in the NP and SP (Figure 4.1), in July, 2017 (wet season) and January, 2018 (dry season), respectively.

The seabed of NP and SP mainly consists of fine sediment. In particular, medium grain sizes (D_{50}) of the two observational sites in this study are between 20 - 50 μm with a high clay content of about 20 - 30 % [Ge et al., 2020]. The seabed is even more fine-grained seaward of the two observational sites ($d_{50} < 10$ μm with a clay content > 35 %).

4.2.2. In-situ Observation

Field observations were conducted from 07/02 (mm/dd) to 07/15 (2017) in the NP, and 01/15 – 01/28 (2018) in the SP, using a tripod system (Figure 4.2). The average water depth (measured by pressure sensor of OBS) at these two sites was about 10.3 m and 8.4 m, respectively. The tripod system integrated a D&A Optical Back-scattering Sensor (OBS) for turbidity, salinity, and depth (pressure) observations, two RDI Acoustic Doppler Current Profilers (ADCPs) for current ve-
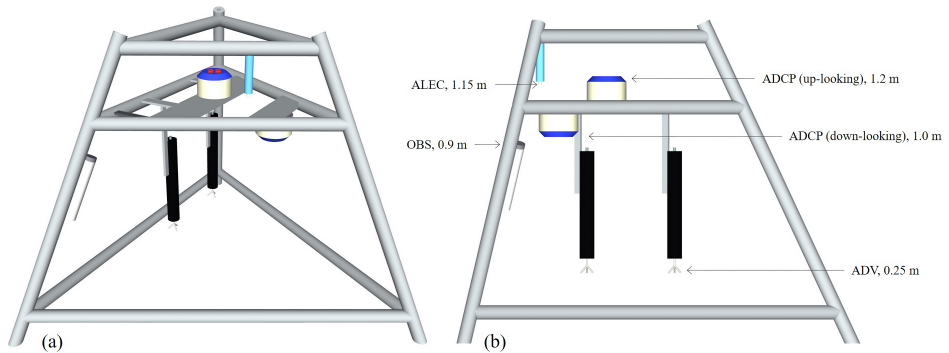
Figure 4.2: Top view (a) and side view (b) of the tripod system in the 2017 observation. In the 2018 observation, the same tripod was used with height of OBS sensor adjusted to 0.4 m above the bed.

locity observations (the up-looking ADCP can also measure waves), a JFE ALEC Point Current Meter (ALEC) to measure current velocities in the blanking range of the two ADCPs, and two Nortek Acoustic Doppler Vectors (ADVs) for current velocity and bed level observations. Figure 4.2 shows the deployment of instruments on the tripod system. For the observation in 2018, the sensor of the OBS was lowered to about 0.4 meters above the bed and the ALEC had a malfunctioning battery, and therefore did not obtain any data. The surface layer of the bed sediment was sampled to calibrate the OBS. Turbidity data measured by the OBS was converted into SSC data based on a calibration curve obtained from laboratory experiments. Detailed configurations of the tripod instruments are listed in Table 4.

Table 4: Instruments mounted on the tripod and their sampling configurations.

Instrument deployed	Distance above bed (m)	Sampling interval (min)	Sampling configuration	Survey parameter
ADCP-up	1.2	/	120 s (1 hour for wave observation)	Profile velocity, waves
ADCP-down	1.0 (down)	/	120 s	Profile velocity
ALEC	1.15	2	0.2 Hz (every first 50 s)	Velocity
ADVs	0.25	10	16 Hz (every first 70 s)	Near-bed velocity
OBS	0.9	/	100 s	Salinity, temperature, turbidity, pressure

The ADV recorded the distance between the probe and the bed (D), and therefore a relative bed level (RBL) can be defined as:

$$RBL_{observed} = \overline{D} - D \qquad (4.1)$$

where the overbar denotes the time-averaged value. RBL calculated with Eq 4.1 shows the variation of bed levels, with an increasing trend indicating deposition

and a decreasing trend indicating erosion. River discharge was observed at Datong Gauge Station (located about 600 km upstream). We used this discharge data with a 5-day delay due to the transmission period of the river flow to our observational sites. Note that there was a flood event during the observational period in 2017. Results of observations are presented in section 4.3.1.

4.2.3. K-P Model Framework

In this study, we used the following equations to calculate erosion and deposition rates (unit: $[kg/(m^2 s)]$) [Ariathurai, 1974; Krone *et al.*, 1962; Partheniades, 1965; Whitehouse *et al.*, 2000]:

$$\frac{dM_e}{dt} = \begin{cases} m_e \left(\frac{\tau - \tau_{ce}}{\tau_{ce}} \right), & \tau > \tau_{ce} \\ 0, & \tau \leqslant \tau_{ce} \end{cases} \tag{4.2}$$

$$\frac{dM_d}{dt} = -c_b w_{s,b} \tag{4.3}$$

where m_e and τ_{ce} are erosion parameter and critical shear stress for erosion, respectively; $w_{s,b}$ is settling velocity; τ represents bed shear stress and c_b denotes bottom sediment concentration. The unit of m_e is $[kg/(m^2 s)]$. The bed shear stress τ is calculated with both the Grant-Madsen method [Madsen, 1994] and the turbulent kinetic energy (TKE) method. Both methods provided similar results (see Appendix A.1), and because of the better continuity of data collected by ADCP compared to the ADV we apply results of the Grant-Madsen method hereafter. c_b is the near-bed suspended sediment concentration (unit: $[kg / m^3]$) measured with the (calibrated) OBS, and $w_{s,b}$ is the near-bed settling velocity (unit: [m/s]) corrected for hindered settling using [Dankers *et al.*, 2007]:

$$w_{s,b} = w_{s,0} \frac{(1 - \phi)^m (1 - \phi_p)}{1 + 2.5\phi} \tag{4.4}$$

where $w_{s,0}$ is the initial settling velocity for a single sediment grain in still water; $\phi = c_b/c_{gel}$ is the volumetric sediment concentration; $\phi_p = c_b/\rho_s$ is the volumetric primary particle concentration, ρ_s is the density of sediment 2650 kg/m^3; m represents non-linear effects for which we use m = 2, and c_{gel} is specified as 250 kg/m^3 [Ge *et al.*, 2015]. The cumulative relative bed level (from t_0 to T) can be computed by integrating the erosion and deposition rates at each time step:

$$RBL_{simulated} = \sum_{t_0}^{T} \left(\frac{dM_e}{dt} + \frac{dM_d}{dt} \right) \Delta t / \rho_d \tag{4.5}$$

where ρ_d is the dry density, assuming as 1,300 kg/m^3 [Milliman *et al.*, 1985]; Δt is the time step. The K-P model is therefore driven by measured values for c_b and τ, while m_e, τ_{ce}, and $w_{s,0}$ ($w_{s,b}$) remain to be determined.

4.2.4. Estimation of Erosion and Deposition Fluxes

As clarified in the previous section, to estimate deposition and erosion fluxes, first we need to determine the erosion and deposition parameters, i.e. m_e, τ_{ce}, and $w_{s,b}$. Here we propose a methodology to obtain these three parameters simultaneously, with which erosion and deposition fluxes can be further calculated.

Over a user-specified time window of length T and within a user-defined range of unknown input parameters (m_e, τ_{ce}, and $w_{s,0}$), a large number of K-P model realizations are executed. The number of model realizations is a multiplication of the number of variations in m_e, τ_{ce}, and $w_{s,0}$, representing all possible combinations of the unknown input parameters. Within the time window, the predicted bed level ($RBL_{simulated}$) of all model predictions is compared with the measured bed level changes ($RBL_{observed}$) using a correlation coefficient R^2 (Root Mean Square Error (RMSE) is also checked - see Figure 4.10). The parameter set with the highest correlation coefficient is defined as the most representative parameter set (Figure 4.3) within the evaluated time window T. The time window then shifts forward in time with ΔT to run the model for the same amount of input parameter combinations. Note that $\Delta T < T$, resulting in a more gradual change in input parameters compared to a simple piecewise segmentation with the time window T. To maximize the consecutiveness of input parameters, ΔT equals to temporal resolution of the observational data. The resulting time-varying K-P model input parameters are subsequently used to compute timeseries of the erosion and deposition flux.

Two aspects of the model require specific attention: the length of running window T and the equifinality of parameters. The length of the running window determines for how long the parameters are representative. The window length cannot be too short because of (1) the stochastic nature of transport processes and (2) the frequency of measurement output. The stochastic nature introduces a certain natural variability of bed level changes, and therefore the window length must be sufficiently long to generate a realistic set of RBL not influenced by random noise. Secondly, output for measured data is available at hourly intervals (some at higher frequency, but the data with the lowest temporal resolution, i.e., waves measured by the up-looking ADCP, is limiting the resolution of the whole data set here). To compute a meaningful correlation, a sufficiently large number of observations must be available within each window T. Furthermore, a short time window will also aggravate the second issue, i.e., equifinality of the input parameters. However, when T is too long, relevant information is averaged out.

Equifinality is the concept that within a model system multiple input parameter sets exist which generate the same outcome. Applied to the K-P framework, equifinality arises from (1) the balance between the deposition flux ($w_{s,0}$) and the erosion flux (τ_{ce} and m_e) in the net bed level change, and (2) the balance between τ_{ce} and m_e in defining the erosion flux. Multiple parameter sets can therefore lead to equivalent levels of R^2, and small changes in R^2 may lead to frequent and irregular switching from one parameter set to another. This irregular switching in input parameters resulting from non-uniqueness can be minimized by using a longer running window T. The best model fit is therefore a balance between an overly averaged solution and a rapidly alternating solution resulting from equifinality. The
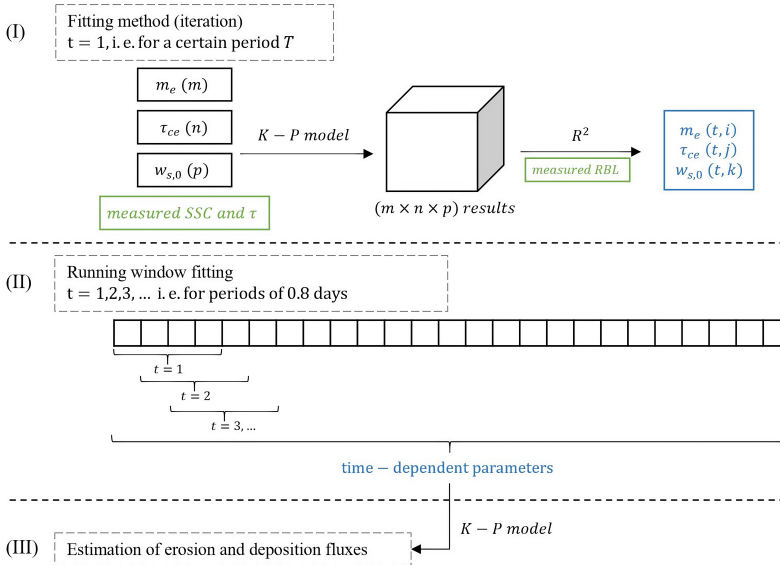
Figure 4.3: Schematized procedure for data fitting. The general approach (I) is to compute a large number of possible relative bed levels (RBL), realized with a range of K-P model settings by varying τ_{ce}, m_e, and/or $w_{s,0}$, and fit these to observed RBL using an R^2. Then the approach is repeated with a running window fitting method (II), providing a timeseries of freely varied input parameters. These time-varying parameters are subsequently used to compute erosion and deposition fluxes (III).

effect of the time window was tested using T = 0.5, 0.8 and 1.0 days, corresponding to 13, 20, and 25 samples per window. Time window of 0.8 days provided the best compromise between overly averaged and too variable results (based on the 2017 data set, not shown in this paper).

4.3. Results

4.3.1. Observations in 2017

The river discharge increased during the observational period, reaching 70,000 m^3/s on 07/10 (nearly twice the average wet season discharge) - see Figure 4.4a. The tides changed from neap to spring tidal conditions (Figure 4.4b), with a peak flood current velocity (Figure 4.4c, d) increasing from 46 (neap) to 101 cm/s (spring) and a peak ebb current velocity increasing from -74 (neap) to -183 cm/s (spring) (Figure 4.4c, d, measured at about 1.15 m above the bed). The river discharge strengthened the ebb current velocity after spring tide (07/08), leading to prolonged ebb-dominant conditions. The observed salinity varied between 0 and 23 PSU (Figure 4.4e). During high-discharge conditions, the salinity decreased to about 0 PSU during the ebb tide, which influences flocculation and therefore the sediment settling velocity. The settling velocity of sediments in the Changjiang
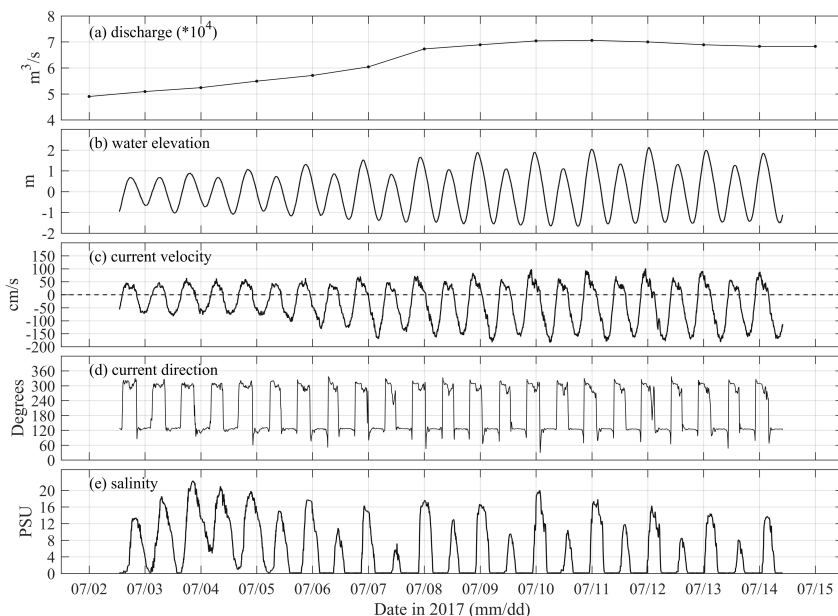
Figure 4.4: Observed variables: (a) discharge (Datong Gauge Station), (b) water elevation (OBS), (c) current velocity (ALEC), (d) current direction, and (e) salinity (OBS). The positive values of current velocity denote flood currents.

Estuary has been observed to increase when salinity exceeds 4 PSU [Jiang *et al.*, 2002], and therefore the salinity variation may be important for tidal variability in the settling velocity. However, salinity is not the only factor that can affect settling velocity: in the Changjiang Estuary SSC can have larger impact on settling velocity than salinity [Wan *et al.*, 2015]. Turbulent shear is also important for flocculation and settling velocity change, with higher turbulent shear typically decreasing the floc size and settling velocity. As tripod-mounted instruments are inconclusive on the mechanisms potentially controlling the settling velocity. We limit ourselves to the temporal variation in the settling velocity, rather than separate effect induced by SSC, salinity, or turbulence.

The SSC had four main peaks per day (Figure 4.5a), formed during 2 flood maximums and 2 ebb maximums of the semi-diurnal tides. Detailed mean SSC values of the different periods are provided in Table 5. The SSC was higher during and after spring tide, resulting from either advection (due to higher river discharge) or resuspension (due to higher bed shear stress) (Figure 4.4a and Figure 4.5b). The bed shear stress was up to 2.5 N/m^2 during maximum ebb of spring tide (Figure 4.5b). Compared to spring tidal conditions, the bed shear stress was low ($< 0.5\ N/m^2$) during neap tidal conditions. This pronounced difference resulted in different patterns of bed level changes (the RBL measured by two ADVs, Figure 4.5c). These two data sets showed good agreement in patterns of RBL, although the absolute values were not the same. At 12:08 07/03, there was a break in the ADV-2 data,
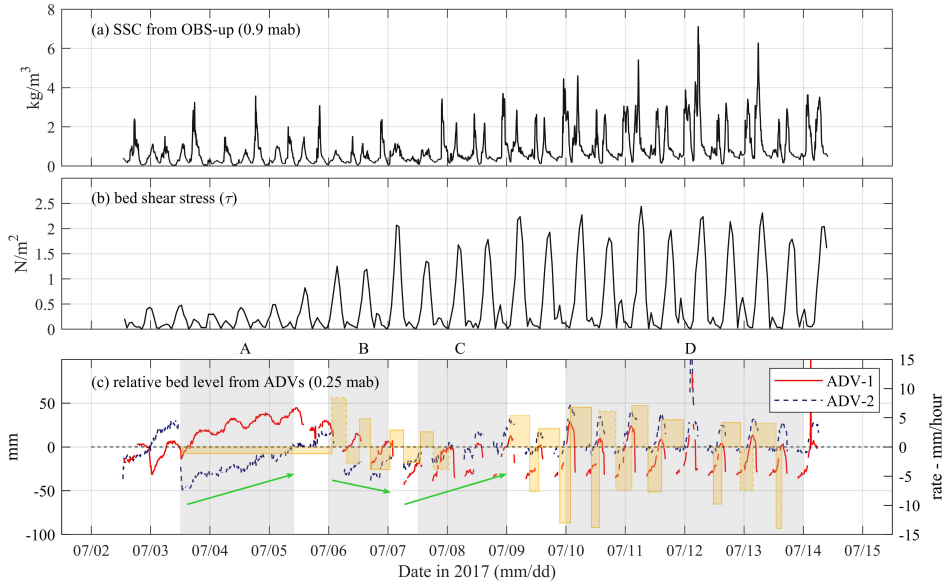
Figure 4.5: Observed and calculated variables in 2017 observation: (a) suspended sediment concentration, (b) bed shear stress, and (c) relative bed level (left y-axis) and erosion/deposition rates (right y-axis, in yellow bars, positive values denote erosion). See panel (c) for the periods of stage A, B, C, and D.

which we attribute to mass movement of sediment. Except for this disturbance, other characteristics for example the intratidal variation were comparable. No bed levels were detected by ADVs at the end of each erosion period (especially from 07/10 to 07/14). This may have been caused by reflection of the acoustic signal against a more solid bed layer underlying softer surface sediment because acoustically highly reflective materials can cause very large return signals and pollute the water column (Nortek AS, 2018). This hypothesis is supported by the normalized RBL, correlation, and noise amplitude from ADV raw data - see Appendix A.2 in the supporting information. These data gaps occurred at a consistent level (around -40 mm in Figure 4.5c), indicating a non-erodible layer at this depth.

The results from ADV-1 (red line in Figure 4.5c) are used as the primary measured data set in the following analysis. In addition to the intratidal variation mentioned above, four stages with very clear characteristics could be observed (Figure 4.5c), i.e. deposition during neap tide (A), erosion (B), deposition during spring tide (C), and a stage with large variation but little net change (D).

Period-averaged erosion and deposition rates are presented in Figure 4.5c with yellow bars. In stage A, the overall deposition rate was low (-1.1 mm/hour) but persistent. Erosion rates were higher than deposition rates during stage B, resulting in an overall erosion trend. For stage C, it is hard to distinguish the start and end moment of erosion or deposition period due to the blank areas of ADV data. Therefore, no detailed erosion or deposition rate is given. In stage D, the duration

Table 5: Information for stage-based analysis.

Stage	Time	Tidal condition	Mean SSC (kg/m^3)	Main pattern of RBL
A	07/03 12:00:00 - 07/05 10:00:00	neap	0.54	deposition
B	07/06 00:00:00 - 07/07 00:00:00	moderate to spring	0.46	erosion
C	07/07 12:00:00 - 07/09 00:00:00	spring	0.72	deposition
D	07/10 00:00:00 - 07/14 00:00:00	moderate to neap	1.21	large variation, small net change

4

of erosion periods was longer than that of the following deposition periods. This was because periods of strong hydrodynamic conditions were long, resulting from the river flood event. On the other hand, a large amount of suspended sediment (high SSC) lead to high deposition rates, jointly resulting in a large variation of bed level but with very small net change. During the whole observation, the erosion rate was about 5 - 10 mm/hour and the deposition rate was about 7 - 15 mm/hour.

4.3.2. Observations in 2018

The river discharge was much lower and continuous (between $1.3 - 1.6 \times 10^4$ m^3/s) during this dry season, indicating stable and limited effects of discharge on both hydrodynamics and sediment dynamics (Figure 4.6a). Tidal conditions changed from spring to neap tide (Figure 4.6b), with more or less equal flood and ebb velocities (Figure 4.6c, d) resulting from the low river discharge. Current velocities were in the range of -100 - 100 cm/s during spring tide and about -60 - 60 cm/s during neap tide. The salinity was in the range of 16 - 25 PSU (Figure 4.6e), with pronounced tidal variations during spring tide (before 01/18). The salinity was more constant during in-between spring and neap tide (01/19 - 01/22), and decreased towards neap tidal conditions (after 01/22).

The SSC was less than 1.0 kg/m^3, i.e., much lower than that during the 2017 observations (Figure 4.7a). The spring to neap tide transition resulted in a decrease of the bed shear stress (Figure 4.7b). Although the D_{50} and the clay component of the observational sites in 2017 and 2018 were similar [Ge et al., 2015], the different hydrodynamic conditions resulted in totally different erosion and deposition patterns. The RBL was continuously increasing (Figure 4.7c), with a gradually decreasing rate of net deposition. Assuming the settling velocity was constant (little change in river discharge conditions), the fairly constant SSC in Figure 4.7a should result in a fairly constant deposition flux. This suggests that the erosion flux gradually increased during this period. This is physically realistic as the erodibility of surface layer of bed sediment can be expected to increase in time as progressively more sediment deposits, with fresh deposits being more easily re-suspended (despite the decrease in the bed shear stress).
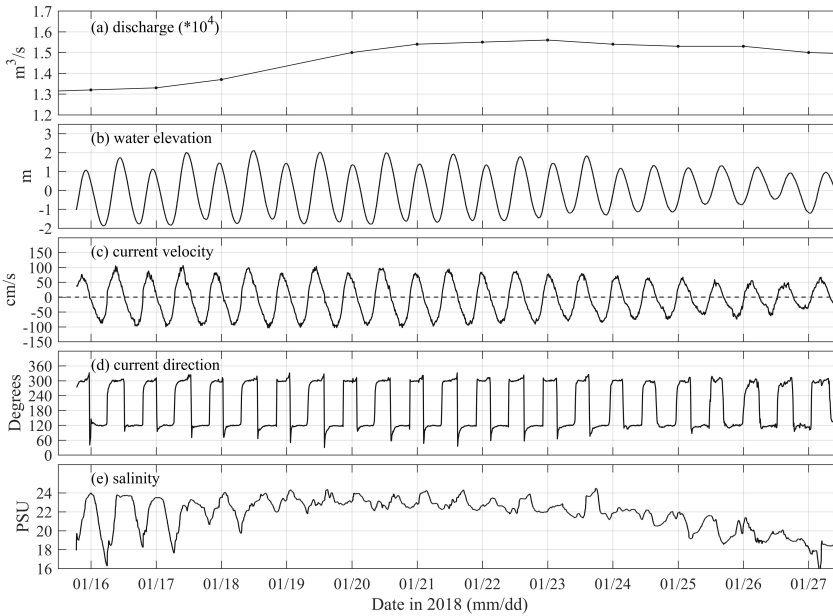
Figure 4.6: Observed variables: (a) discharge (measured at Datong Gauge Station), (b) water elevation (OBS), (c) current velocity (ADV), (d) current direction, and (e) salinity (OBS). The positive values of current velocity denote flood currents.

4.3.3. Erosion and Deposition Fluxes

The RBL can be well reproduced when allowing the fitting parameters to vary over time (see Figure 4.8a for the 2017 data set). However, free fitting results in large variability of the input parameters (Figure 4.8b - d). The $w_{s,0}$ was mainly in the range of 1 - 3 mm/s; τ_{ce} was mostly concentrated between 0.05 - 0.15 N/m^2; m_e showed a larger variability in the range of $1 - 6 \times 10^{-4}$ $kg / (m^2 s)$ which was in agreement with the typical range $0.1 - 5 \times 10^{-4}$ $kg / (m^2 s)$ in Winterwerp *et al.* [2012]. Even though these values typically remain within a realistic range (partly resulting from the user-defined range of these parameters), the variability itself is not always realistic. The frequent switching of free-fitted parameters was the result of equifinality-induced uncertainties, i.e. multiple parameter combinations providing comparable solutions, with very similar correlation (see section 4.3.4). Therefore, an additional result is also presented in Figure 4.8 using constant parameters over the evaluation period. This result is an example of equally good constant parameter sets, detailed method to determine the realistic constant parameters will be given in section 4.3.4. The reproduced RBL with constant parameters captured main patterns of bed level changes in 2017.

The bed level change observations in 2018 suggest the erosion and deposition patterns were not constant (decreasing deposition despite a reduction in bed shear stress with comparable SSC), implying that the RBL cannot be reproduced with a constant parameter set. This will be demonstrated in section 4.3.4 and the physical
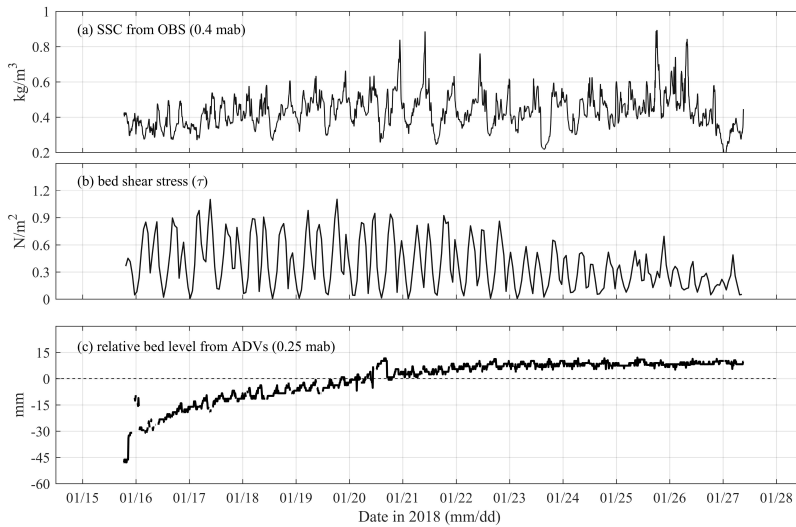
Figure 4.7: Observed and calculated variables in 2018 observation: (a) suspended sediment concentration, (b) bed shear stress, and (c) relative bed level.

mechanisms for erosion and deposition patterns in 2018 will be explored in more detail in section 4.4.1. For the analysis of erosion and deposition fluxes hereafter, we will only focus on the constant and time-varying parameters obtained for 2017.

The best-fit time-varying and constant parameters were used to compute the time variation in erosion and deposition fluxes (Figure 4.9). Despite the substantial difference in bed level change (Figure 4.8a), the differences between erosion and deposition fluxes calculated with constant or time-varying parameters were relatively small in variation patterns (Figure 4.9). Maximum erosion and deposition fluxes were about 0.01 $kg/(m^2 s)$. The erosion flux increased from neap to spring tidal conditions (Figure 4.9a), due to stronger flow velocities while the deposition flux simultaneously increased as near-bed SSC was higher during spring tide (Figure 4.9b). The synchronous increase of both erosion and deposition fluxes indicated more dynamic water-bed exchange in spring tidal conditions, leading to larger bed level fluctuation, but without a pronounced change in the net bed level.

For given measured bed level change and other input variables (e.g. bed shear stress, SSC), the erosion flux is influenced by both τ_{ce} and m_e, while the deposition flux is only determined by $w_{s,0}$. As the bed level change computed with time-varying parameters can be considered as a best fit, the accuracy of the fluxes computed with constant parameters can be evaluated by correlating them with the fluxes computed with time-varying parameters. As a result, the R^2 is relatively high (0.85 for the erosion fluxes, and 0.65 for the deposition fluxes), with the computed fluxes mainly differing in their peak values. The high similarity of fluxes between constant and time-varying parameters supports the use of not only time-varying, but also constant parameters for flux estimation. However, an important question
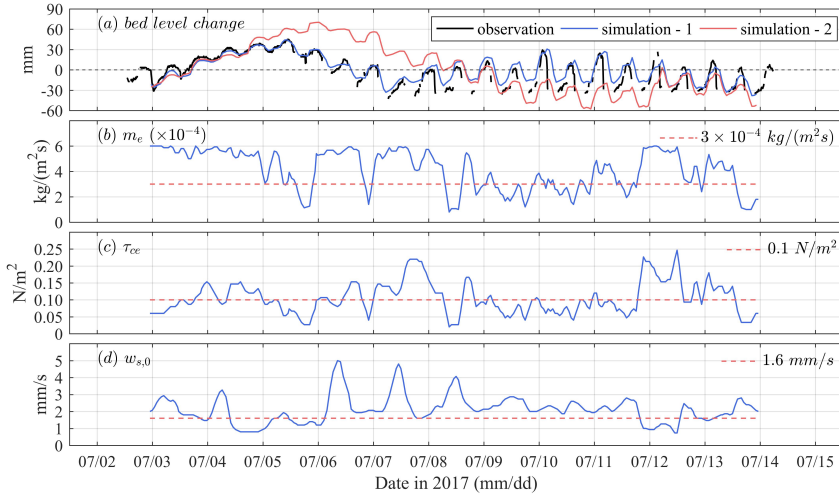
Figure 4.8: (a) Comparison between measured RBL in 2017 (ADV-1) and simulated RBL using time-varying (blue) and constant (red) parameters, and time-varying and constant m_e, τ_{ce}, and $w_{s,0}$ (b, c, d). Parameters presented here are smoothed using the MATLAB smooth function (moving average, span = 3) and the RBL (blue) is reproduced with these smoothed parameters.

that needs to be addressed in greater detail is how the various input parameters are interrelated, moreover, how many constant parameter sets for bed level prediction exist. This will be addressed in the following section.

4.3.4. Constant Parameters in the K-P Model

The erosion flux is composed of the erosion parameter m_e and the critical erosion shear stress τ_{ce} and, within a given distribution of bed shear stress, the same integrated erosion flux can be achieved with multiple combinations of m_e and τ_{ce}. Similarly, the erosion flux balances the deposition flux, where again within a given distribution of the bed shear stress, sediment concentration and settling velocity, multiple sets of m_e, τ_{ce}, and $w_{s,0}$ exist, leading to a comparable variability in bed levels. Therefore, we propose a tool to evaluate this interdependence in greater detail by linking m_e, τ_{ce}, and $w_{s,0}$.

For every combination of specific (constant) τ_{ce} and m_e, the time-dependent $w_{s,0}$ can be computed with the running window fitting according to the highest R^2. Although for many of the τ_{ce} and m_e combinations, even the best fit $w_{s,0}$ cannot provide an accurate RBL, consequently resulting in a low R^2. However, the fitted $w_{s,0}$ still provides the best result of settling velocity for given combination of τ_{ce} and m_e. The average value of the fitted $w_{s,0}$ is shown in Figure 4.10. The black lines are contour lines of averaged $w_{s,0}$, the red dashed lines are contour lines of time-averaged R^2 (as the R^2 is also time-dependent in the running window fitting). In addition, Root Mean Square Error (RMSE) between the measured and reproduced bed level changes is shown in this figure to double check the reliability of R^2. This diagram reveals that (for instance) using a τ_{ce} of 0.1 N/m^2 requires m_e around 0.6,
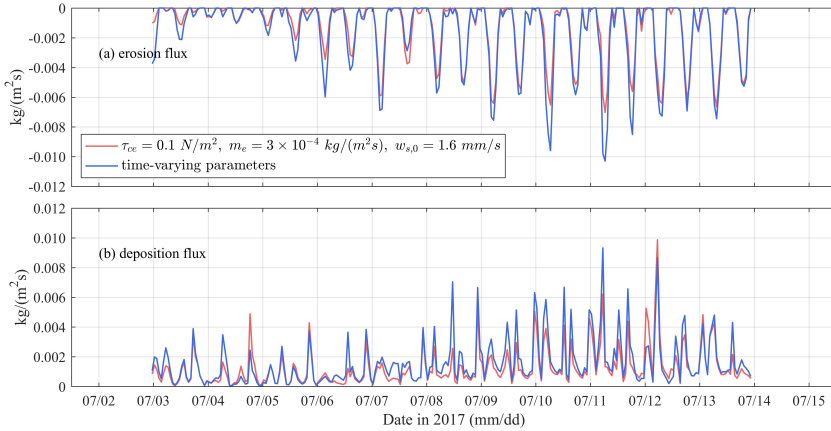
Figure 4.9: (a) Erosion flux (a) and deposition flux (b) using the settings of Figure 4.8.

1.8, 2.8, and 3.8 $\times 10^{-4}$ kg / $(m^2 s)$ when applying a settling velocity of 0.5, 1.0, 1.5, and 2.0 mm/s, respectively, for the 2017 data set (Figure 4.10a). Moreover, the contours of R^2 provides a parameter space including more possible parameter sets that can well reproduce the RBL (between the 0.65 red dashed contours of R^2). A constant $w_{s,0}$ between 1.5 and 2 mm/s can lead to best result (averaged R^2 around 0.65). Note that the lowest RMSE (8.0 mm) overlaps the highest R^2 (0.65), further proving the reliability of the parameter space. In this parameter space, the minimum constant τ_{ce} is about 0.06 N/m^2, and the minimum constant m_e is about 1.7 $\times 10^{-4}$ kg / $(m^2 s)$. This information is important for the parameterization in numerical models, which provides a realistic range of parameters. The example parameter set presented in the previous section 4.3.3 (Figure 4.8) is also marked in Figure 4.10a with a diamond shape. It is in the range of the parameter space provided by this visualization diagram, indicating the validity and significance of this visualization method.

For the data set in 2018, the largest averaged R^2 is only 0.21 (Figure 4.10b), it is clear that there is no constant parameter set that can well reproduce the observed bed level change in Figure 4.7c. Apparently, constant parameters cannot reflect the variability of bed properties (erodibility). This will be elaborated more in section 4.4.1. Results in Figure 4.10b are also valuable for bed level simulations, as they clearly guide us to analyze what processes are missing in the primitive K-P model, instead of trying to find a constant parameter set which does not exist.

4.4. Discussion

4.4.1. Optimization of the RBL Reproduction

No constant parameter set can well reproduce the RBL of the 2018 data set. In this section, we will elaborate more on the underlying physical mechanisms and potentially improve the performance of K-P model for the 2018 data set. As
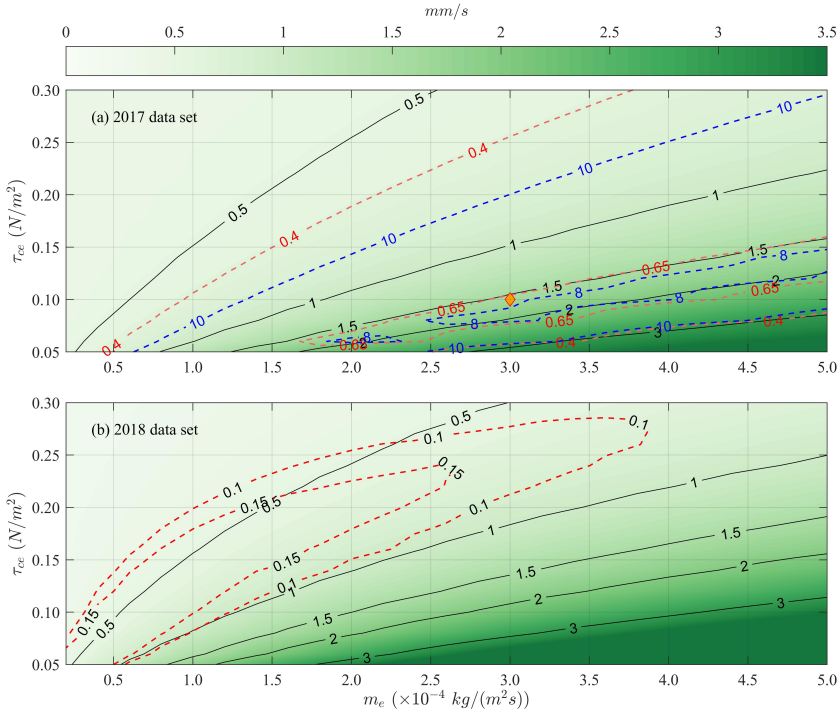
Figure 4.10: Average value of fitted $w_{s,0}$ (black contours) as a function of τ_{ce} and m_e for data sets in 2017 (a) and 2018 (b). The red and blue dashed lines indicate contours of averaged R^2 and RMSE (R^2 and RMSE are time-varying in the running window fitting). The diamond-shape marker denotes an example of parameterized τ_{ce}, m_e, and $w_{s,0}$ (1.6 mm/s). RMSE, Root Mean Square Error (unit: [mm]).

explained in section 4.3.2, the erodibility of the sediment may increase in time, consequently resulting from progressively looser material due to continuous deposition. The resulting hypothesized reduction in sediment density leads to a higher erosion parameter (m_e) and lower erosion threshold (τ_{ce}) according to Whitehouse et al. [2000], introducing equifinality. However, Winterwerp et al. [2012] suggest that the degree of consolidation primarily influences m_e, but not τ_{ce}. To avoid equifinality issues, we follow Winterwerp's approach, i.e. keeping τ_{ce} constant.

Rapid deposition leads to slower consolidation rates, as consolidation time scales with the square thickness of the consolidating layer (as in the diffusion term in the Gibson et al. [1967] consolidation equation). It can therefore be hypothesized that the erodibility of the sediment scales with the deposition process. The m_e in turn scales with the degree of consolidation while the degree of consolidation can be reflected by thickness of the deposited layer, especially in a continuous net deposition period (Figure 4.7c). To test this hypothesis, m_e was correlated to the available amount of sediment for erosion. Available sediment was represented by H ($H = RBL - \overline{RBL}$) which can indicate whether the surface layer is newly deposited or not. The m_e was derived from the running window fitting with constant τ_{ce}

and $w_{s,0}$. The values of τ_{ce} and $w_{s,0}$ were indicated by Figure 4.10b. The high R^2 concentrated at the left-bottom corner, therefore, we used $\tau_{ce} = 0.1\ kg/(m^2 s)$ and $w_{s,0} = 0.8$ mm/s to obtain the time-dependent m_e.

The free fitted m_e is correlated with H, represented by an exponential relationship (Figure 4.11a). This relationship suggests that m_e increases with the bed level, at least during the observational period characterized by continuous deposition. The acquired relation for m_e can subsequently be used to improve the bed level prediction, by generating a constructed time-varying m_e as H increases during deposition. Time-series values of fitted and predicted m_e are shown in Figure 4.11b.
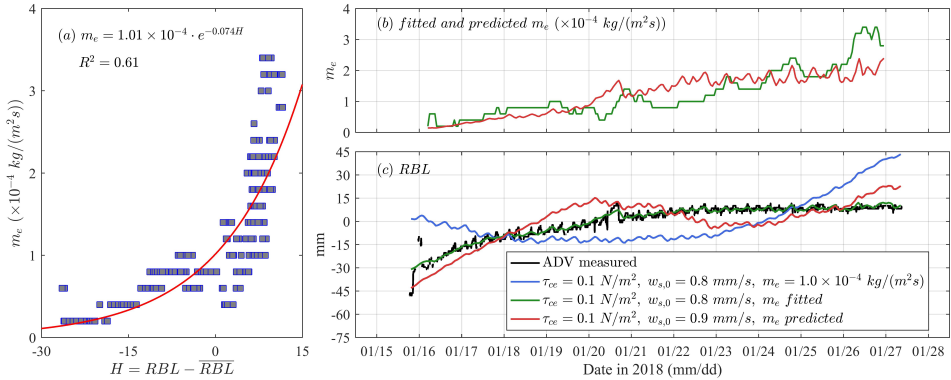
Figure 4.11: (a) Exponential relationship between the fitted m_e ($\tau_{ce} = 0.1\ kg/(m^2 s)$, $w_{s,0} = 0.8$ mm/s) and H, (b) fitted (same as m_e in (a)) and predicted m_e (according to the exponential relationship in (a)), (c) RBL in different scenarios.

In Figure 4.11c, results of measured and reproduced RBL are presented. The blue line shows one example of the relatively good RBL predictions using constant parameters inspired by Figure 4.10b. Note that the combination of τ_{ce} and $w_{s,0}$ was also used to fit the time-varying m_e in Figure 4.11b. The predicted RBL (blue line) shows a large difference compared to the measured RBL, especially in terms of net deposition rate. The fitted time-varying m_e resulted in well predicted RBL (green line) which is close to measured values. The result of RBL using a constructed m_e with a slightly adjusted $w_{s,0}$ (red line) significantly improved the bed level prediction compared to the constant m_e (although for obvious reasons less accurate than the fitted time-varying m_e).

By correlating m_e and H, we obtained a time-series of m_e which can reflect the variability of sediment erodibility. It also explains why we could not find a constant parameter set for the 2018 data set and provides implication for how we could improve the K-P model for such a continuous deposition period. Note that here we do not provide a detailed and concrete method that is coded into a numerical model. Our findings provide an example to show the importance of changeable erodibility. Quantitatively describing details in the sediment bed requires the use of a consolidation model (with as a drawback that more input parameters are needed

for such a model).

4.4.2. Limitations of the Fitting Method

The sediment concentration in estuaries such as the Changjiang Estuary is determined by local resuspension and advection processes. Advection can give rise to lag effect between local shear stress and the SSC, resulting in discrepancy between the real bottom sediment concentration and the calculated value (if advection-diffusion is not included in the calculation). However, the K-P model describes local water-bed exchange processes at the interface between sediment and water. Therefore, caution should be taken when apply the K-P framework in estuaries where advection plays a crucial role. In this study, we applied the observed SSC which actually included effects of advection, therefore the lag effect between SSC and local shear stress was minimized. Even though, it would be an important improvement on our understanding of water-bed dynamics if we can further distinguish effects of advection and resuspension on sedimentation. A possible next step is to split the observed SSC signal into advection-related and resuspension-related parts using multiple methods, for example, the harmonic analysis [Krivtsov *et al.*, 2008; Nayak *et al.*, 1999; Weeks *et al.*, 1993].

A second limitation of the current fitting and estimating method is that we used suspended sediment concentration (at about 0.9 mab) as the bottom sediment concentration. Although there is often a relationship between the near-bottom SSC and the real bottom sediment concentration (described with the Rouse concentration profile), there is a systematic deviation. In the future, this deviation could be decreased by deploying the turbidity sensor at a lower position to obtain a more accurate bottom sediment concentration.

A third limitation is the assumption of a single fraction. In our study areas, the sea bed is mainly composed of fine cohesive sediments with spatial and temporal variability in sediment compositions and properties. Due to this background, the advection can cause a complex mixing and interaction between advected and locally suspended sediment, resulting in a spatially and temporally changing mixture of sediment particles and therefore changing settling velocity. However,studying on a single sediment fraction provides fundamental information and is of great practical values. A potential future improvement could be to account for multiple sediment fractions by introducing extra variability in settling velocities. This can be jointly improved by applying observation instrument that can measure sediment fractions (particle sizes), for example, a LISST.

4.4.3. Implications for Numerical Models

The previous discussion focuses more on water-bed dynamics and parameterization of the K-P model. The methodology and findings in this study also have implications for numerical modelling. Firstly, the method for determining parameters can be directly used in a 1DV model to better understand local erosion and deposition processes. Secondly, for 2D/3D models with a large domain, our method can evaluate the validity of constant parameters in the model. For example, for the 2018 data set, it is unrealistic to reproduce bed level changes for any numerical

model incorporating a primitive K-P model framework with constant erosion and deposition parameters. This indicates that for such a situation where the change of erodibility is significant, a consolidation model is necessary (or at least relationships such as that in Figure 4.11 need to be established) to reflect the variation of erodibility. For the 2017 data set, multiple sets of constant parameters can lead to equifinal results. Figure 4.10 shows a method of visualizing all constant parameter sets. The parameter space indicates all possible choices that can be used in numerical models. This is instructive for model application. However, not all of them are physically reasonable. To reduce the uncertainty, the current method should be combined with more accurate in-situ observations, for example, using the in-situ measured settling velocity can further improve our understanding of erosion threshold (τ_{ce}) and efficient (m_e).

We have discussed the limitation of constant parameters under some conditions. On the other hand, spatial variability of sediment properties is also significant. With the fitting and visualization methods, we can deploy tripods at key locations in the model domain to calibrate erosion and deposition parameters. Therefore, the proposed method can provide a first indication of required processes and boundary conditions before applying a complex 2D/3D model. The method can subsequently provide a parameter space supported by reasonable water-bed dynamics. This is an important improvement for the application of numerical models.

4.5. Conclusions

In-situ observations for bed level changes of the North Passage (the main outlet of the Changjiang Estuary) in 2017 reveal erosion rates of about 5 - 10 mm/hour and deposition rates of about 7 - 15 mm/hour. Bed level changes showed piecewise characteristics superimposed on intratidal variation. Within the whole observational period, the relative bed level showed characteristics of overall deposition, overall erosion, and great intratidal variation with little net change. In-situ observations in 2018 obtained data of hydrodynamics and bed level changes in the South Passage. In the South Passage, the bed level changes showed a continuous net deposition in the dry season. Different variation patterns reflected by these two observations were reproduced with the classic K-P model. The K-P model was driven by measured SSC and bed shear stress, with m_e, τ_{ce}, and $w_{s,0}$ to be determined. With a least-squares fitting method using a running window, time-varying and constant (depending on the length of the running window) parameter sets were obtained. These parameters were further used to estimate the erosion and deposition fluxes. Constant and time-varying parameters could lead to large differences in reproduced peak fluxes, although main patterns of erosion and deposition fluxes in these two cases were similar. However, the bed level prediction can be greatly influenced by peak fluxes, indicating that we should be careful with erosion and deposition parameters for bed level prediction in the timescale of tidal cycles.

The method was further used to determine all possible parameter sets used to predict the bed level variation. Together with the correlation coefficient, these results are graphically presented to directly show the mutual dependence and accuracy of parameters. In terms of model application, this visualization is helpful as it

can provide a parameter space instead of one parameter set, improving our understanding and efficiency of parameter setting of the K-P model. However, more field observations and research are needed to reduce uncertainty in the current methods, obtaining more accurate variations of sediment properties and minimizing the effect of equifinality. For the 2018 data set, there was no constant parameter set that could well reproduce the measured bed level changes. One significant reason could be that the constant erosion parameter could not reflect the change of erodibility (resulting in an R^2 below 0.21) while this was particularly important in this continuous deposition period. The model fit was significantly improved, however, by introducing physically reasonable relations (reflected by parameter dependencies), such as that between the erosion parameter and cumulative deposition.

4

5

Groyne-Induced Effects on Channel-Shoal Exchange and saltwater intrusion

Existing knowledge about groyne-induced effects is primarily based on riverine or coastal environments where salinity gradients are absent or limited. However, in estuaries, salinity gradients drive physical processes such as longitudinal and lateral residual flows. Combined with salinity gradients, the effect of groynes is much more complex as they can modulate channel hydrodynamics and directly affect lateral salinity gradients. In this study, an idealized model is applied to investigate the effects of groyne layouts in estuarine environments, including effects on (1) channel hydrodynamics, (2) lateral water exchange, (3) Coriolis effects, and (4) saltwater intrusion. Model results show that the aspect ratio (the width of groyne fields to the length of groynes) of groyne fields plays an important role. Compared to a channel without groynes, along-channel current velocities in the main channel are significantly enhanced by groynes. Groynes also induce asymmetry of lateral flows, for example, increasing near-bottom shoal-to-channel flows during low water slack. The aspect ratio has opposite effects on horizontal and vertical components of water exchange. A large aspect ratio strengthens horizontal exchange and weakens density-driven currents. For a large-scale groyne field (several kilometers), Coriolis effects introduce a substantial difference in exchange mechanisms along the north and south banks. A medium range of aspect ratio (2.0 - 3.0) leads to the strongest saltwater intrusion during both neap and spring tides.

5

5.1. Introduction

D ikes and groynes have been widely used around the world to regulate and modify hydrodynamics, sediment dynamics, and morphodynamics in rivers, estuaries and coasts. In riverine and estuarine environments, dikes are usually long structures parallel to flow direction while groynes are perpendicular to flow direction and have a relative shorter length compared to the dikes.

Groynes are mostly used in rivers and coastal zones. In river channels, they are mainly used to narrow the channel and increase the flow velocity, thereby increasing the sediment transport capacity, and consequently improve the channel navigability. In coastal zones, they are usually constructed perpendicular to shorelines, functioning as a protection for coasts and beaches from being eroded by alongshore wave-driven currents. Up to now, the effects of groynes was primarily investigated in the context of (1) two-dimensional (2-D) hydrodynamic exchange mechanisms, e.g. horizontal eddy [Sukhodolov et al., 2002], turbulence and shear [Uijttewaal, 2005], water exchange [Uijttewaal et al., 2001], (2) sediment related issues, e.g. sediment exchange [McCoy et al., 2007; Yossef and de Vriend, 2010], sedimentation and morphodynamics [Sukhodolov et al., 2002; Glas et al., 2018], and (3) 3-D flow patterns within the groyne fields [Ouillon and Dartus, 1997; Biron et al., 2005]. As groynes are more and more used in estuaries, one aspect of groynes that has not been systematically investigated is the role of salinity-driven exchange flows.

Groynes are also applied in estuaries to modulate hydrodynamics and alleviate sediment siltation problem, for example, the Changjiang estuary, the Ems estuary, and the Weser estuary [Hu et al., 2009; van Maren et al., 2015; Hesse et al., 2019]. An important difference in estuarine environments compared to coastal and riverine environments is the existence of a salinity gradient in both longitudinal and lateral directions. The longitudinal salinity gradient is important for gravitational circulation and is closely related to saltwater intrusion. Construction of groynes influences the geometry of the main channel, for example, the equivalent width or depth, which impacts channel hydrodynamics and possibly the degree of saltwater intrusion. Additionally, the salinity gradient complicates hydrodynamics in and around groyne fields, strengthening lateral flows and influencing sediment transport patterns [Zhou et al., 2019, 2021]. Temporary storage of salt in the groyne fields during high water generates a salinity gradient between the groyne fields and the main channel which drives a near-bed flow towards the channel during low water slack. Our understanding of groyne effects in estuarine environments needs to be expanded because of the baroclinic processes.

The Changjiang Estuary provides an example of dikes and groynes within the transition zone between fresh and salt water. Two 50-km long dikes were constructed along both banks of the main navigation channel of the Changjiang Estuary (the North Passage), together with 1 ∼ 2-km long groynes about every 5 km. The impact of the groynes on hydrodynamics and sediment transport was investigated by Zhou et al. [2019, 2021] using a realistic 3-D numerical model. However, due to the bathymetric complexities, channel bends, and longitudinal variability of groyne size it is difficult to identify the contribution of specific aspects of the groyne fields

(length, width, depth, aspect ratio, etc.) in those studies. In this study, we aim to unravel the effects induced by groynes on (1) lateral exchange between groyne fields and the main channel and (2) saltwater intrusion. To do this, we set up an idealized hydrodynamic model in which we can systematically modify channel and groyne dimensions.

5.2. Method

5.2.1. Numerical Model

An idealized model is developed using the Finite-Volume Community Ocean Model (FVCOM). FVCOM is a 3-D primitive equation coastal ocean model with unstructured gird. It has been extensively used for hydrodynamics, sediment dynamics, and biogeochemistry studies in both complex geometries [Ge et al., 2015, 2014; Guo et al., 2018a] and schematized environments [Ge et al., 2012; Wu et al., 2011]. In this study, an idealized model is developed to investigate the effect of groynes on hydrodynamics, especially on lateral flow and salinity transport, in a schematized tidal channel-shoal system (Figure 5.1). The schematization of the geometry and hydrodynamic characteristics in the model are based on those of the North Passage, the main navigation route of the Changjiang Estuary.
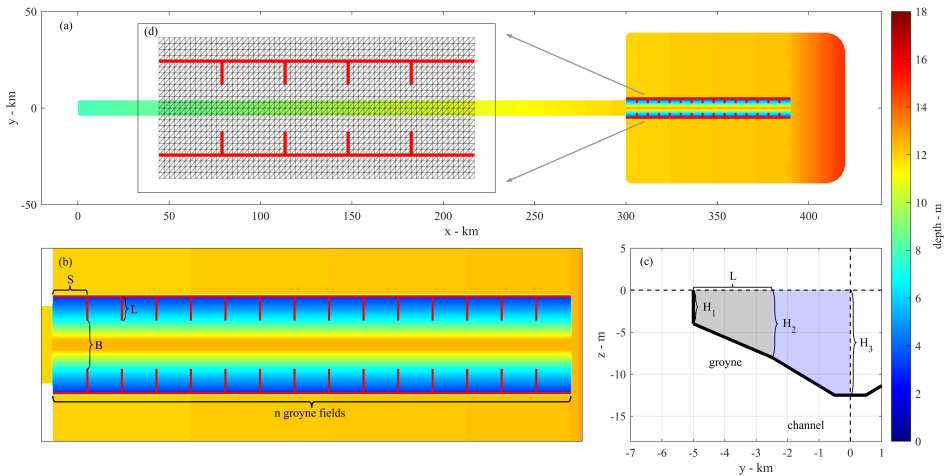
Figure 5.1: (a) Model domain and bathymetry setting of case 0 (a standard case), (b) zoom-in view of the main channel with construction of dikes and groynes, (c) bathymetry of cross-transect in the main channel, and (d) diagram of grid used in the centric area. Note that panel (d) does not include the colored part (only overlapping).

The model domain includes a 300-km river channel and a 120×78-km^2 sea which includes a 90-km main channel with groyne fields on both sides (Figure 5.1a). Here the main channel is defined as the area between north and south groyne tips, while the deep channel means the deepest flat part in the middle of the main channel. Two series of groynes with two long dikes are constructed in the model (Figure 5.1b) with a lateral depth gradient in the groyne fields (Figure 5.1c). The

main channel width (B) remains constant in this study (5 km) with a constant 1-km deep channel. The length of groyne (L) can be adjusted. At the most upstream (x = 300 km) and downstream (x = 390 km) location, there is no groyne.

The model uses an unstructured grid in horizontal directions including 63,546 grid cells and 10 uniform sigma layers in the vertical direction. A constant river discharge of 3,000 m^3/s is applied at the river boundary, and eight major astronomical tidal constituents are specified at the open sea boundary. The amplitudes and phases of the tidal constituents are derived from a tidal analysis based on model results of a well validated FVCOM model, which has been extensively used for research on the Changjiang Estuary [Zhou *et al.*, 2019, 2021; Ge *et al.*, 2020]. A semi-implicit scheme is applied in this model using a time step of 12 seconds.

The bed level in the river channel is from -8 m (x = 0 km) to -12 m (x = 300 km). The bathymetry in the coastal area (x > 300 km) becomes steeper along two gradients, (1) a 0.5 m increase of water depth in the groyne field area (from x = 300 km to x = 390 km), and (2) a 2.5 m increase in the offshore (between x = 390 km to the open boundary at x = 420 km). The depth of the deep channel (-12.5 m in standard Case 0) can be adjusted by changing the slope from the groyne tip to the edge of the deep channel. The definition of model dimensions and relevant notations are summarized in Table 6. The dimensions of the groyne fields and the main channel of the standard case (Case 0) is shown in Figure 5.1c. The idealized

Table 6: Dimension definition and notations in the model.

Notations	Definition
S	length of groyne field
L	length of groyne
B	width of the main channel (between two opposite groynes)
n	number of groyne fields
H_1	depth of groyne (at the groyne root)
H_2	depth of groyne (at the groyne tip)
H_3	depth of the deep channel

model is developed with the aim to study effects of groyne fields on hydrodynamics in the channel-shoal system. Therefore, the dimensions of the groyne fields and the main channel are systematically adjusted for different scenarios. Within the centric area (x from 300 km to 390 km, y from -8 km to 8 km), a right triangle composed rectangular grid (Figure 5.1d) with a resolution of 250 m is used. Outside the centric area the domain is discretized using varying triangle mesh, with a resolution varying from about 1,200 m to 250 m in the river channel, and from about 250 m to 6,500 m from the end of main channel to the open sea boundary.

5.2.2. Scenario Description

The effect of groynes is systematically investigated through 9 model scenarios summarized in Table 7. Case 0 provides a reference case, which best represents

the present-day North Passage of the Changjiang Estuary. Case 1 is set up to quantify the effect of salinity-driven exchange flows. Case 2 to 7 have different distances between groynes while sharing the same length of groynes, providing a comparison on the effect of different aspect ratios of the groyne field. In this study, the aspect ratio is defined as S/L (ratio of the distance between adjacent groynes to the groyne length). Case 8 considers Coriolis force (using 31°N the latitude of the Changjiang Estuary).

Table 7: Scenario summary. In all scenarios, the main channel width (B) remains 5 km. Other notations are defined in Table 6

Name	S (km)	L (km)	S/L	$H_1 - H_2$ (m)	H_3 (m)	Compared to Case 0
Case 0	6.0	2.5	2.4	4 - 8	12.5	
Case 1	6.0	2.5	2.4	4 - 8	12.5	barotropic
Case 2	1.0	2.5	0.4	4 - 8	12.5	
Case 3	2.5	2.5	1.0	4 - 8	12.5	
Case 4	5.0	2.5	2.0	4 - 8	12.5	aspect ratio of groyne fields (number of groynes)
Case 5	7.5	2.5	3.0	4 - 8	12.5	
Case 6	10.0	2.5	4.0	4 - 8	12.5	
Case 7	infinitely large	zero	infinitely large	4 - 8	12.5	
Case 8	6.0	2.5	2.4	4 - 8	12.5	(with) Coriolis force

5.2.3. Water Flux Decomposition

To quantify water exchange between the groyne field and the main channel, a decomposition method is used in this study. The gross exchange is decomposed using the method of Vanlede and Dujardin [2014] which was originally developed to quantify the exchange of water (and sediments) between a harbor basin and an estuary. This requires the definition of an interface between the groyne field and main channel. The area of this interface is determined by the water depth along this transect. The cross-transect velocity (perpendicular to the defined interface, i.e. v component in model output) can be decomposed as:

$$v(x, z, t) = v_{tidal} + v_{hor} + v_{ver} + v_{res} \tag{5.1}$$

where the four terms on the right represent tidal filling and emptying, horizontal exchange, vertical exchange, and a residual component, respectively. v_{tidal} is defined as:

$$v_{tidal} = \frac{\iint_A v \, \mathrm{d}A}{A} \tag{5.2}$$

where A denotes the defined interface:

$$A = \int_S H(x, t) \, \mathrm{d}x \tag{5.3}$$

where H is the water depth and S is the interval between groynes.

The vertical component v_{ver} is computed as:

$$v_{ver}(z,t) = \frac{\int_S v'(x,z,t)\mathrm{d}x}{S} \tag{5.4}$$

where v' is the fluctuation term calculated by subtracting v_{tidal} from v, i.e.,

$$v' = v - v_{tidal} \tag{5.5}$$

and the horizontal component v_{hor} is calculated as:

$$v_{hor}(x,t) = \frac{\int_H v'(x,z,t)\mathrm{d}z}{H} \tag{5.6}$$

Among four terms on the right side of Equation 5.1, v_{ver} represents vertical exchange currents, v_{hor} denotes exchange currents related to horizontal circulation cells. The total water flux due to vertical exchange currents is calculated from v_{ver} and the cross-sectional area as:

$$F_{ver} = \iint_A v_{ver}\mathrm{d}A \tag{5.7}$$

Note that F_{ver} represents a net effect of water exchange due to vertical exchange. The gross exchange is, however, more relevant for studies on lateral flows and their potential effects on sediment transport, and therefore exchange fluxes into and out of the groyne field are computed by splitting v_{ver} into a positive and negative component:

$$v_{ver} = max\{0, v_{ver}\} + min\{0, v_{ver}\} \tag{5.8}$$

subsequently, a positive or negative F_{ver} can be calculated separately. The horizontal water flux F_{hor} is computed following a similar methodology.

5.3. Results

5.3.1. Results of Reference Case

Water Level, Salinity, and Along-Channel Current Velocity

An idealized model cannot be directly calibrated or validated against observational data. Since our model is based on the North Passage in the Changjiang Estuary, we compare results from our idealized model (reference case 0) to the main hydrodynamic characteristics of the North Passage using observational data and a well-validated process-based model [Zhou *et al.*, 2019].

The water levels in the main channel reveal a clear neap-spring tide variation (Figure 5.2a) with a period of about 14 days. The maximum tidal range is about 2.6 m during spring tides. The tidal form factor ($F = (K_1 + O_1)/(M_2 + S_2)$) calculated along a longitudinal transect in the channel is 0.26 - 0.29, indicating mixed, mainly semi-diurnal tides, in agreement with the semi-diurnal tides in the North Passage.
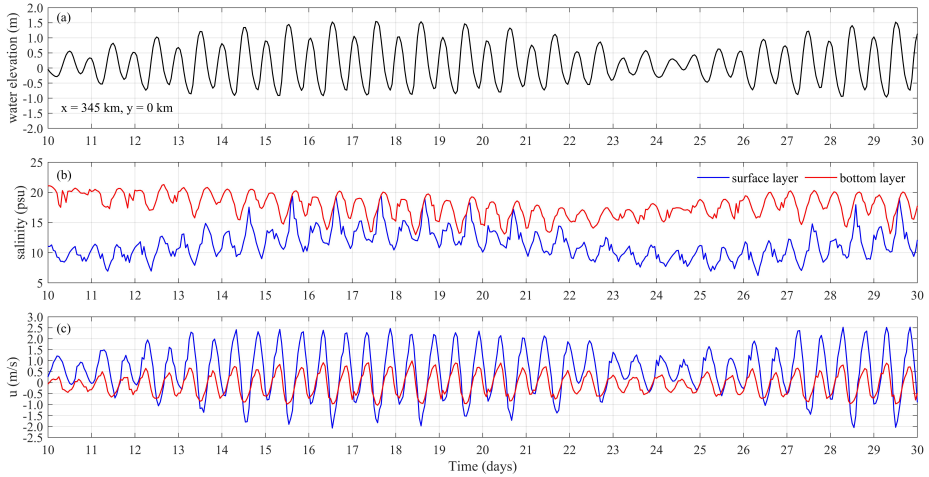
Figure 5.2: (a) Water elevations and (b) surface and bottom salinity and (c) current velocity at the middle of the main channel (x = 345 km, y = 0 km) in Case 0.

Due to a constant river discharge (3,000 m^3/s), the salinity variation is in dynamic equilibrium, varying over the tidal cycle and over the spring-neap cycle but without an apparent decreasing/increasing trend. Over the spring-neap cycle, the salinity varies between 8 - 20 psu in the surface layer, and 13 - 22 psu in the bottom layer (Figure 5.2b). During neap tides (Day 10 - 12, Day 24 - 26), the salinity variation is relatively small compared to other periods. Moreover, the difference of salinity between surface and bottom layers is also much larger during neap tides. These stratified neap tidal conditions reflect stronger saltwater intrusion during neap tides, in agreement with the situation in the North Passage.

The computed bottom along-channel velocity is in the range of -1.2 - 1.2 m/s (Figure 5.2c), which agrees with the typical along-channel velocity in the North Passage [Lin *et al.*, 2021; Zhou *et al.*, 2021]. The surface along-channel velocity is ebb-dominant while the bottom along-channel velocity is slightly flood-dominant. The vertical variation of current velocity results from salinity-driven gravitational circulation.

Stratification

A bulk Richardson number (R_{ib}) is used to quantify stratifying and mixing conditions. A high R_{ib} ($\log_{10}(R_{ib}/0.25) > 0$) indicates strong stratification (and lower values indicate mixing). During high water slack (HWS), the whole channel is strongly stratified, and stratification is more pronounced in the deep channel and around groyne tips (Figure 5.3a). The main channel becomes well-mixed during peak ebb, while the groyne fields remain highly stratified (Figure 5.3b). During low water slack (LWS), the groyne fields are vertically well-mixed, except at the interface between the groyne fields and the main channel (Figure 5.3c). The strong stratification along the interface is induced by salinity-induced shoal-to-channel (STC)

lateral flow (with salt water from the groyne field being transported to the main channel as a near-bed density current). In the main channel, there is a transition between mixing and stratifying conditions from upstream to downstream. During peak flood, the main pattern of stratification is similar to that during peak ebb (Figure 5.3d), although mixing in the main channel is weaker and stratification in the groyne fields is stronger compared to peak ebb. The patterns of stratification in Figure 5.3 show high similarity with the stratification distribution in the North Passage reported in Zhou *et al.* [2021] in the following aspects: (1) the order of magnitude of R_{ib}, (2) the spatial patterns of R_{ib} (especially the difference between the groyne fields and the main channel) at characteristic time periods, (3) the strong stratification around the groyne tips during low water slack (LWS). These similarities further suggest the idealized model captures the most important characteristics of the Changjiang Estuary's North Passage.
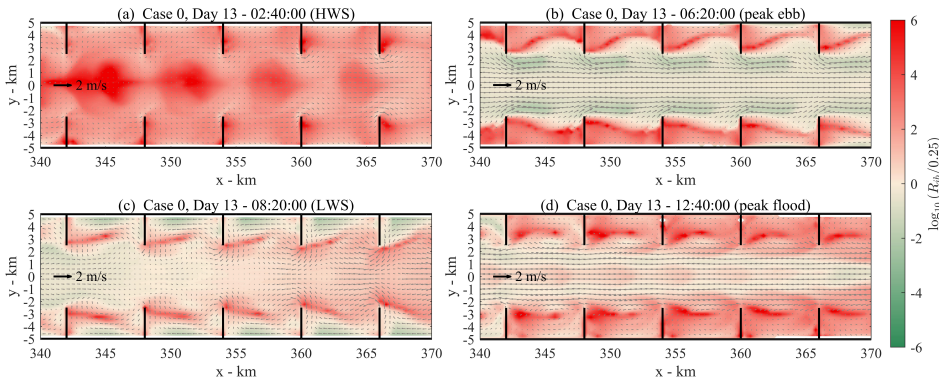

Figure 5.3: Distribution of bulk Richardson number ($\log_{10} (R_{ib}/0.25)$) and velocity vectors in the channel for high (a) water and low (c) water slack (HWS and LWS, respectively), peak ebb (b) and peak flood (d) currents. High and low water slack conditions are based on flow velocity reversal, not exactly corresponding to the time of high water and low water, respectively. Results are from Case 0.

Lateral Flow and Effects of Salinity

During moderate and the following spring tides, the retention of salt water in groyne fields during ebb leads to pronounced lateral flows during low water slacks. Shoal-to-channel density-induced lateral flows may occur or be enhanced, especially in the bottom layer of water column. Since the sediment concentration is usually much higher in the bottom layer, this lateral flow pattern constitutes an important sediment transport from groyne fields to the main channel. To further investigate lateral flow and potential effects on mass exchange between groyne fields and the main channel, results of bottom lateral current velocities from Case 0 during moderate tide at four characteristic time periods are shown in Figure 5.4. The lateral velocities are presented in a converging direction, i.e. positive for shoal-to-channel (STC) currents and negative for channel-to-shoal (CTS) currents. For results of neap and spring tides, see Appendix A.3.
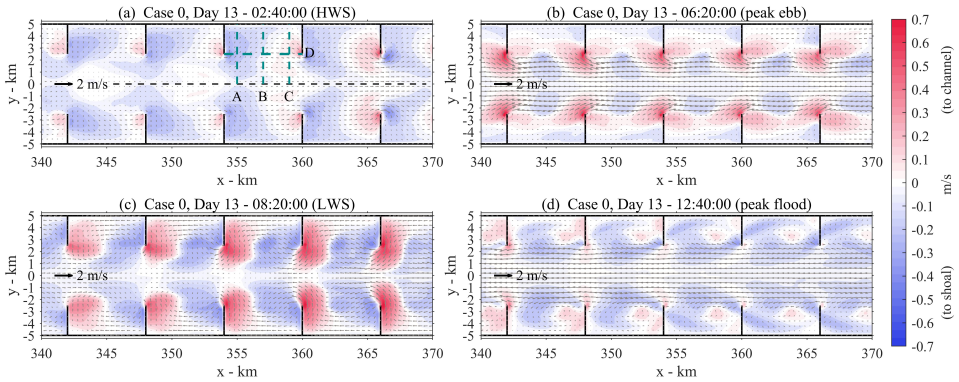
Figure 5.4: Bottom lateral current velocities and velocity vectors at (a) HWS, (b) ebb maximum, (c) LWS, and (d) flood maximum. Positive value indicates a direction from groyne fields to the main channel (STC, from both sides). These results are from Case 0 in moderate tidal conditions. Three cross-channel and one along-channel transects are marked with cyan dashed lines for the following analysis. HWS, high water slack, LWS, low water slack.

In this section, we use the north groyne filed between x = 354 to 360 km to illustrate lateral flows in the bottom layer. During HWS, STC lateral currents with a velocity between 0.1 - 0.2 m/s occur upstream of the groynes, while other parts are dominated by channel-to-shoal (CTS) currents (Figure 5.4a). For the weak hydrodynamic conditions characteristic for HWS, these transverse flows are relatively small. During peak ebb currents, stronger lateral flows (0.2 - 0.4 m/s) exist both landward and seaward of the groynes, and CTS currents exist in the main channel (Figure 5.4b). During LWS, significant bottom STC currents occur seaward of the groynes, with a maximum velocity exceeding 0.7 m/s (Figure 5.4c). This result agrees with findings by Zhou *et al.* [2019, 2021]. Effects of salinity gradient joint with existence of groynes result in asymmetric lateral flows during HWS and LWS. During peak flood currents (Figure 5.4d), the lateral flows are relatively weak, similar to the period with peak ebb currents. Figure 5.4 indicates an obvious difference of bottom lateral flows related to the relative position in groyne fields to groynes. Therefore, lateral flows on three cross-channel transects in the groyne field at different positions (1 km downstream to a groyne, at the middle of a groyne field, and 1 km upstream to a groyne) are shown in Figure 5.5 (see Figure 5.4a for plan view position of the transects).

During HWS, a STC pattern is observed in the groyne field at the surface layer, with a progressive increase in magnitude (from 0.05 to 0.4 m/s) (Figure 5.5a, 5.5e and 5.5i). CTS currents occur at greater depths and in most areas in the main channel. During the following ebb maximum, STC currents (0.1 - 0.2 m/s) dominate in the groyne field in transect A (whole water column, see Figure 5.5b), while transect B is mainly characterized by CTS currents (Figure 5.5f) and a lateral circulation structure can be found in transect C (Figure 5.5j). During LWS, the groyne field and the low water column in the main channel have strong STC currents (up to 0.4 m/s) in transect A (Figure 5.5c). In transects B and C, CTS currents dominate
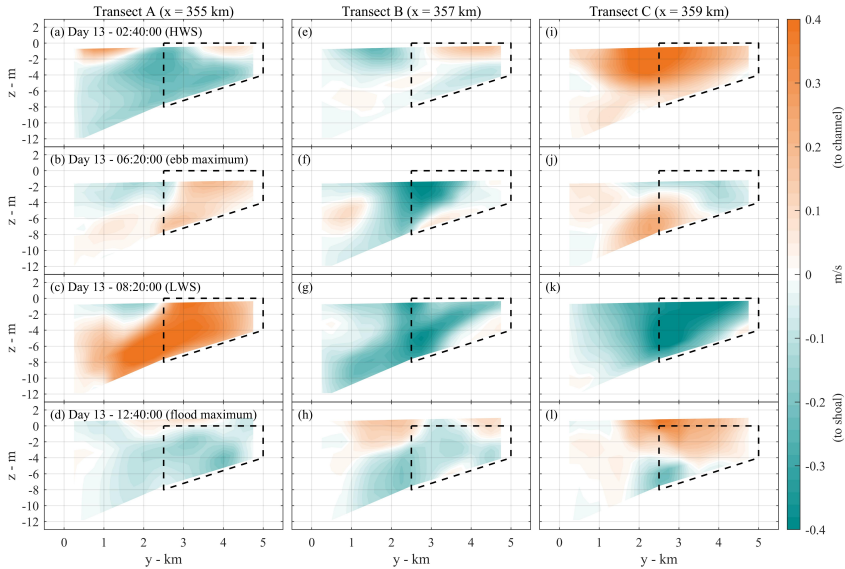
Figure 5.5: Lateral flows on three cross-channel transects in Case 0, i.e., (a) - (d) transect A at x = 355 km (1 km downstream to a groyne), (e) - (h) transect B at x = 357 km (at the middle of a groyne field), and (i) - (l) transect C at x = 359 km (1 km upstream to a groyne), at HWS (first row), ebb maximum (second row), LWS (third row), and flood maximum (fourth row). The four time periods are identical to those in Figure 5.4. Black dashed lines indicate cross-channel extension of groynes. See Figure 5.4a for plan view position of the transects.

(Figure 5.5g and 5.5k). During peak flood currents, transects A and B have weak CTS currents with a magnitude below 0.2 m/s (Figure 5.5d and 5.5h), while STC currents occur in transect C (Figure 5.5l). The pattern of lateral flows during flood maximum shows a consistency with the pattern of HWS.

The lateral flows and channel-shoal water exchange are strongly influenced by groyne fields and salinity gradients. Effects of salinity gradients are shown in Figure 5.6. During the ebb period, salt is kept in the groyne fields due to retention effects of groynes (Figure 5.6a and 5.6b). Then the salinity gradient between the groyne fields and the main channel drives the lateral flow during LWS (Figure 5.6c). Figure 5.6d shows the transport of salt into the groyne fields. In the barotropic case (Case 1), the lateral flow during LWS is much lower compared to Case 0 (not shown here).

Horizontal Eddy Structure

The idealized model reflects the formation and breakdown of a horizontal eddy structure. Here we take the bottom layer as an example, see Appendix A.4 for the horizontal eddy structure in the surface layer. At 02:40 (HWS), the streamlines indicate that weak ebb currents enter the groyne field but flow out of the groyne field without the development of a pronounced eddy structure (Figure 5.7a). A pronounced eddy develops in the groyne field at 07:00 during max ebb (Figure 5.7b). Near the end of the ebb period, the streamlines show similarity with those
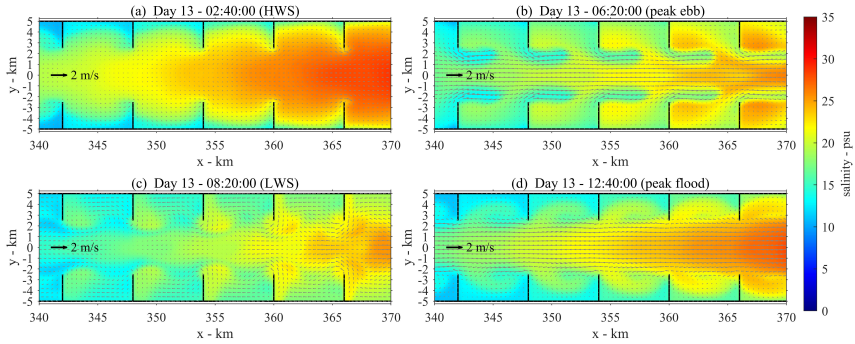
Figure 5.6: Bottom salinity distribution in Case 0 at four moments corresponding to time periods in Figure 5.4, i.e., HWS, peak ebb, LWS, and peak flood, respectively.

during HWS (Figure 5.7c). Figure 5.7d to 5.7f illustrate a process of formation, extension, and breakdown of an eddy during the flood period. The streamlines pattern is periodic, and after 14:40 (Figure 5.7f), a new cycle starts with an eddy similar to that during HWS (Figure 5.7a).
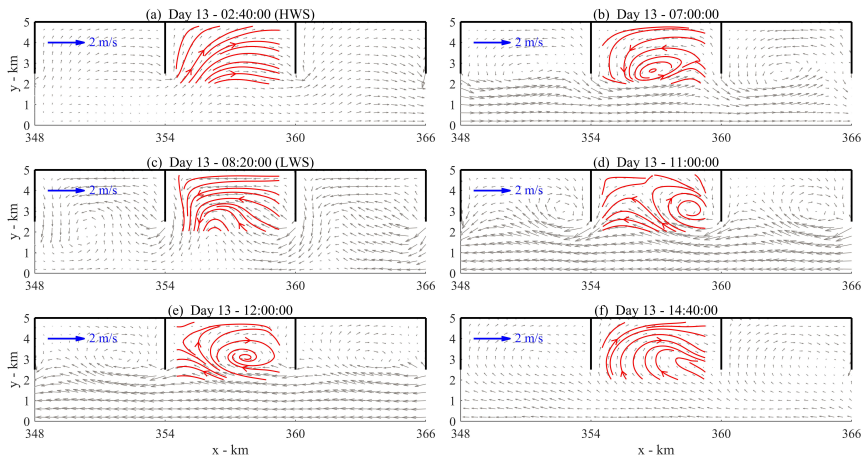
Figure 5.7: Velocity vectors (grey arrows) in the main channel and streamlines (red lines) in the groyne field during moderate tides, blue arrows are length scales for velocity vectors. Velocity data is from the bottom layer of Case 0.

The eddy structure in the groyne field is featured with a primary eddy and dynamic eddy near the groyne tip. The dynamic eddy mainly occurs at the beginning of ebb and flood processes, not shown in Figure 5.7. The eddy structure presented here is not the same as that in the laboratory experiments of Uijttewaal et al. [2001], lacking a secondary eddy. The main reason for this difference is the effect of roughness in the groyne field. In laboratory experiments, the water depth in shoal areas are much smaller than the setting in our idealized model (and in the

groyne fields in the Changjiang Estuary) and therefore, frictional effects in the laboratory experiments are larger than that in our idealized model. Another important influencing factor for horizontal eddy is horizontal eddy viscosity. In this model, the horizontal eddy viscosity is calculated with the Mellor-Yamada level 2.5 turbulent closure scheme [Mellor and Yamada, 1982].

5.3.2. Scenario Comparison

Tidal Propagation

Construction and different layouts of groynes are expected to influence tidal propagation. These tidal modulations by groyne field layouts need to be known to understand more detailed hydrodynamics within the channel such as channel-shoal exchange processes. The effects of groynes on tidal propagation are therefore investigated using Case 2 to Case 7 (and the reference Case 0).

The major velocity of the M_2 tide (computed using the T-Tide toolbox [Pawlowicz et al., 2002]) just seaward of the main channel is about 1.1 m/s. As tides enter the channel (at about x = 390 km), the tidal velocity decreases, albeit differently for the various scenarios (Figure 5.8). The M_2 maxium velocity decreases progressively for Case 2 to Case 6. Halfway the main channel (350 - 360 km) the M_2 velocity amplitude increases again for scenarios with a small groyne field aspect ratio. The fluctuation in Case 4 to Case 6 is directly related to the aspect ratio, i.e. at locations where groynes are constructed there is an increase of velocity as the channel is locally narrowed by groynes.
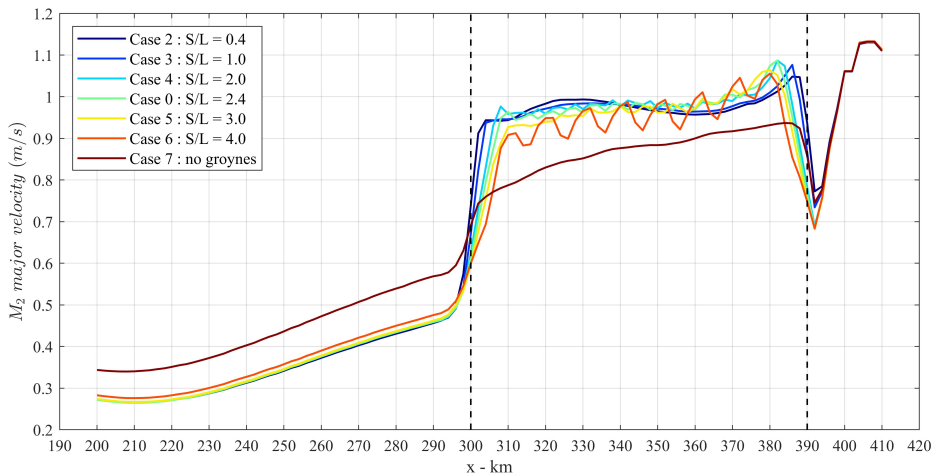
Figure 5.8: Longitudinal distribution of major velocity of M_2 tide in scenarios with different numbers of groynes, by harmonic analysis for depth-averaged longitudinal velocity. Two black dashed lines indicate the upstream and downstream boundaries of the channel.

Case 7 is an extreme case without any groyne in the channel, which essentially corresponds to a widened channel and a situation before construction of groynes. This results in a smaller tidal velocity in the channel, but a larger velocity in the
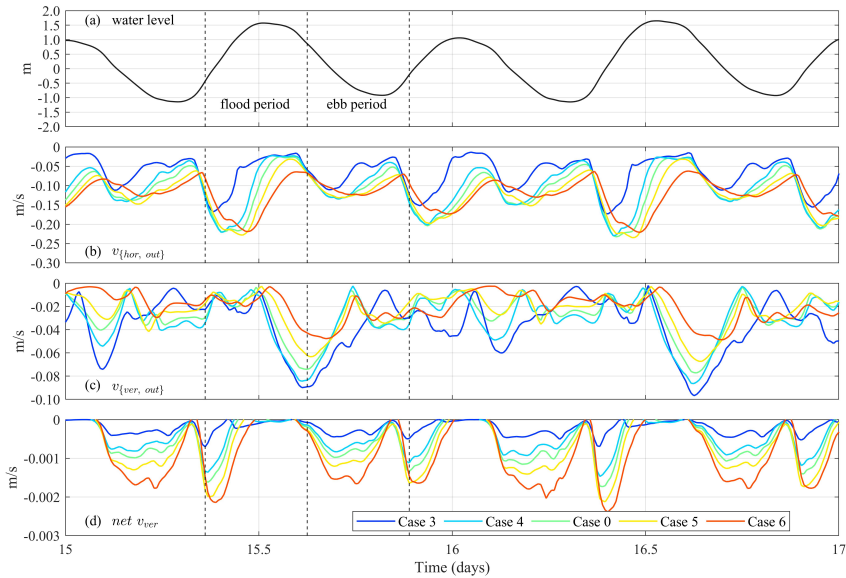
Figure 5.9: (a) Water level in Case 0 averaged on an along-channel transect (transect D in Figure 5.4a); (b) horizontal component of exchange velocity, outflowing from a groyne field to the main channel in different scenarios; (c) vertical component, similar to panel (b); (d) net vertical component of exchange velocity across the interface between a groyne field and the main channel.

up-estuary tidal river (Figure 5.8). Case 7 demonstrates that the construction of groynes modulates the velocity distribution in the whole system, including the velocity in the main channel. This agrees with the common designing purpose of groynes in a navigational channel, i.e. to maintain channel depth by increasing the current velocity.

Effects of Aspect Ratio

Using the method introduced in section 5.2.3, the exchange velocity and water flux can be decomposed. These parameters reflect the channel-shoal exchange mechanisms in response to groyne field dimensions. The aspect ratio can affect the eddy structure in groyne fields [Uijttewaal *et al.*, 2001; Sukhodolov *et al.*, 2002; Uijttewaal, 2005] and determine the amount of salt that can be transported into and stored in groyne fields. Therefore, the aspect ratio may have a considerable impact on channel-shoal exchange, from both vertical and horizontal perspectives. For different aspect ratios, the cross-sectional areas where exchange between a groyne field and the main channel take place differ in size and therefore the total exchange flux cannot be used for a scenario comparison. Therefore, v_{ver} and v_{hor} in Equation 5.4 and 5.6 are used to discuss effects of aspect ratio on lateral exchange. For each scenario, which groyne field to conduct the calculation is determined by the averaged salinity in the groyne field from Day 10 to Day 25 (averaged over both time and volume).

The water level is provided in Figure 5.9a for reference to the tidal cycle. $v_{\{hor,out\}}$

Table 8: Average value of outflowing horizontal component, outflowing vertical component, and net vertical component of exchange velocity on the flood and ebb period, respectively.

Case name	Aspect ratio	outflowing v_{hor} (m/s)		outflowing v_{ver} (m/s)		net v_{ver} ($\times 10^{-4}$ m/s)	
		flood	ebb	flood	ebb	flood	ebb
Case 3	1.0	-0.066	-0.067	-0.036	-0.044	-1.15	-2.75
Case 4	2.0	-0.106	-0.092	-0.034	-0.039	-2.23	-5.17
Case 0	2.4	-0.120	-0.099	-0.029	-0.037	-2.73	-6.39
Case 5	3.0	-0.136	-0.106	-0.021	-0.035	-3.88	-7.99
Case 6	4.0	-0.145	-0.103	-0.017	-0.033	-5.73	-9.61

and $v_{\{ver,out\}}$ represent the outflowing v_{hor} and v_{ver} from the groyne field to the main channel. $v_{\{hor,out\}}$ is stronger for a larger aspect ratio (Figure 5.9b). The maximum $v_{\{hor,out\}}$ is about 0.23 m/s in all scenarios. In particular, $v_{\{hor,out\}}$ is obviously smaller (about 0.17 m/s) for the smallest aspect ratio (Case 3) compared to other scenarios. The positive correlation between the aspect ratio and $v_{\{hor,out\}}$ is also reflected in the time-averaged value (Table 8). During both flood and ebb periods, $v_{\{hor,out\}}$ decreases as the aspect ratio decreases, indicating a smaller aspect ratio can constrain the horizontal exchange.

For the vertical component v_{ver}, $v_{\{ver,out\}}$ and the net v_{ver} show opposite patterns compared to v_{hor} (Figure 5.9c and 5.9d). A smaller aspect ratio can lead to a larger peak of $v_{\{ver,out\}}$ (about 0.09 m/s) at the end of flood tide (Figure 5.9c). However, the net v_{ver} is smaller compared to other scenarios (Figure 5.9d), indicating that a smaller aspect ratio can lead to stronger cross-channel vertical circulation, i.e. inflowing (in the surface layer) and outflowing (in the bottom layer) currents are all stronger with a smaller aspect ratio. This is also evident from values of v_{ver} averaged over the flood and ebb period (Table 8): a smaller aspect ratio strengthens gravitational circulation in the lateral direction. This inverse influence of the aspect ratio on v_{ver} and v_{hor} is probably related to the impact of v_{hor} on residence times. With a large aspect ratio, the horizontal flow component is large and salt water is flushed out of the groyne field by horizontal flows. This weakens the transverse salinity gradient between the main channel and the groyne fields, and consequently the salinity-driven vertical exchange flows. For smaller aspect ratios, salt water needs to be flushed out by gravitational currents.

In summary, aspect ratio can cause opposite effects on horizontal exchange and gravitational circulation. A small aspect ratio can enhance gravitational circulation while prohibit horizontal exchange. Although horizontal component is usually much larger than the vertical component (Figure 5.9 and Table 8), the vertical effects may be amplified when calculating the transport of materials which have vertical gradient of concentrations, for example, the suspended sediment. More investigation is needed and caution should be taken when designing the aspect ratio.
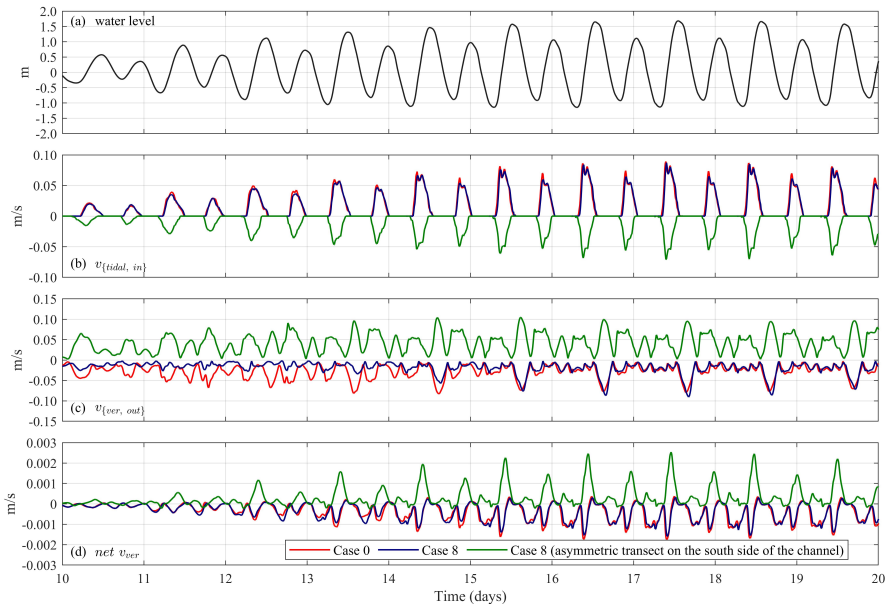
Figure 5.10: (a) Water level in Case 0 averaged on an along-channel transect (transect D in Figure 5.4a); (b) tidal filling component of exchange velocity, inflowing from the main channel to groyne fields; (c) vertical component of exchange velocity outflowing from groyne fields to the main channel; (d) net vertical component of exchange velocity.

Effects of Coriolis Force

Coriolis force can influence salinity transport and lateral exchange in the channel-shoal system. The influence is from two aspects, first, the difference caused by Coriolis force particularly in the north groyne field compared to the standard case, and second, the asymmetry induced by Coriolis force between the north and south groyne fields. Therefore, a groyne field on the north side in Case 0 and two symmetric groyne fields in Case 8 (with Coriolis force) are compared in terms of tidal filling induced exchange velocity and vertical component of exchange velocity (the horizontal component is mainly determined by the aspect ratio and effects of Coriolis force are limited from both aspects mentioned above). Note that for groyne fields on the north side, a positive value of the exchange velocity represents inflowing velocity while for groyne field on the south side (green lines in Figure 5.10), it represents outflowing velocity.

In Case 8, the Coriolis force causes stronger inflowing velocity induced by tidal filling on the north groyne field compared to the south groyne field (Figure 5.10b). However, for Case 0 and Case 8, the Coriolis force shows negligible effect on the north side groyne field. The Coriolis force obviously decreases $v_{\{ver,out\}}$ in the north groyne field, especially during neap tides (Figure 5.10c). However, the Coriolis force results in a larger $v_{\{ver,out\}}$ on the south side, forming a significant asymmetry between the north and south sides. This asymmetry is more significant during

Table 9: Average value of inflowing tidal filling component, outflowing vertical component, and net vertical component of exchange velocity during neap tides (Day 11 - 12) and spring tides (Day 15 - 16), respectively.

Case name	location	inflowing v_{tidal} (m/s)		outflowing v_{ver} (m/s)		net v_{ver} ($\times 10^{-4}$ m/s)	
		neap	spring	neap	spring	neap	spring
Case 0	north	0.009	0.018	-0.032	-0.029	-1.61	-5.09
Case 8	north	0.009	0.017	-0.012	-0.022	-1.82	-4.81
Case 8	south	-0.007	-0.012	0.037	0.046	1.14	4.02

neap tides, the daily averaged $v_{\{ver,out\}}$ is about twice as large on the south side than on the north side (Table 9). For the net v_{ver}, the difference between Case 0 and Case 8 is relatively small (Figure 9d). Although the highest values of the net v_{ver} is larger in the southern groyne field, the second peak (during ebb tide) is much smaller, resulting in a smaller day-averaged net v_{ver} (Table 9). These findings illustrate that for large-scale groyne fields (several kilometers), such as those in the Changjiang Estuary, Coriolis force introduces a substantial difference in exchange mechanisms along the south and north banks.

5

saltwater intrusion

As groynes strongly influence channel hydrodynamics, they also influence saltwater intrusion. In this section, we compare saltwater intrusion for scenarios with different groyne configurations (Case 2 to Case 7, including Case 0). The degree of saltwater intrusion is represented with the 1-psu contour line in Figure 5.11. From top to bottom (Figure 5.11a through 5.11g; Figure 5.11h through 5.11n), the amount of groynes decreases. The saltwater intrusion first increases with a decreasing amount of groynes (Figure 5.11a to 5.11c and Figure 5.11h to 5.11j), but decreases again when the amount of groynes further decreases (Figure 5.11d to 5.11g and Figure 5.11k to 5.11n); in both neap and spring tidal conditions. These results indicate that (1) the amount of groynes has a non-linear effect on saltwater intrusion and that (2) a specific number of groynes exist for which saltwater intrusion is maximal.
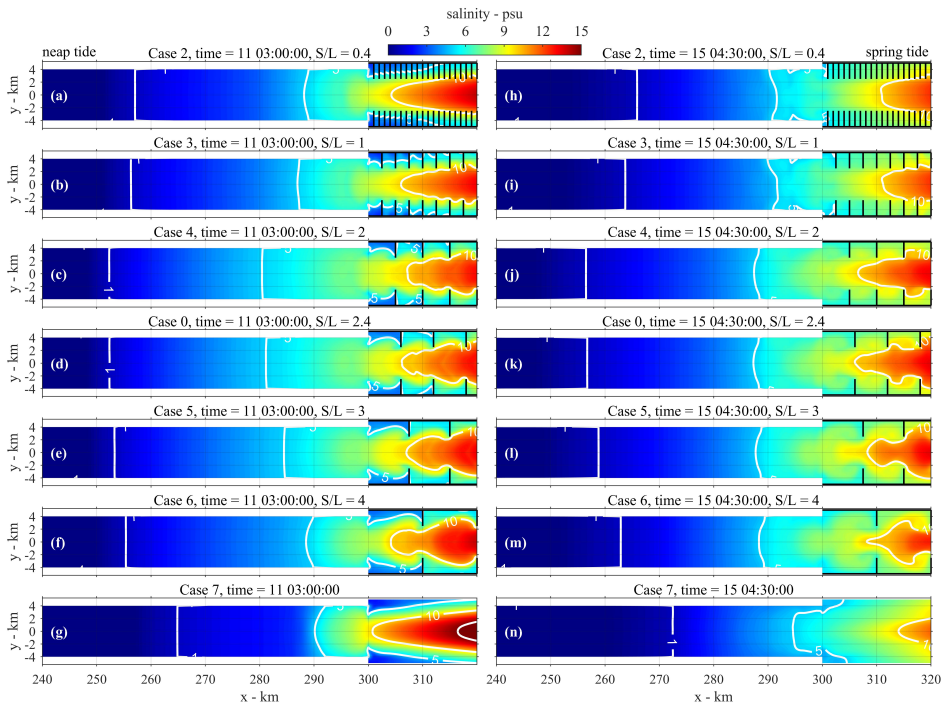
Figure 5.11: Saltwater intrusion in different scenarios during neap (left column) tide and spring (right column) tide. Contour lines of 1, 5, 10, 15 psu are shown with white lines.

The difference of saltwater intrusion between neap tides and spring tides is reflected most clearly by high-salinity contour lines (Figure 5.11). During neap tides, the 10-psu contour lines show an opposite pattern compared to the 1-psu contour lines (minimal intrusion for intermediate aspect ratios). However, during spring tides, the 1-psu and 10-psu contour lines are more consistent in terms of intrusion distance. This is illustrated more clearly in Figure 5.12. The most significant

saltwater intrusion occurs when 12 - 18 groynes are constructed on each side of the channel, corresponding to aspect ratio about 2.0 - 3.0. This is opposite for the 10-psu and 15-psu salinity contour lines computed during neap tides (Figure 5.12).

Summarizing, it is demonstrated that groynes influence the saltwater intrusion. Groynes may enhance saltwater intrusion with 12.8 km to 16.0 km (for neap to spring tides) compared to Case 7 (without any groyne). This will be discussed in more detail in section 5.4.1.
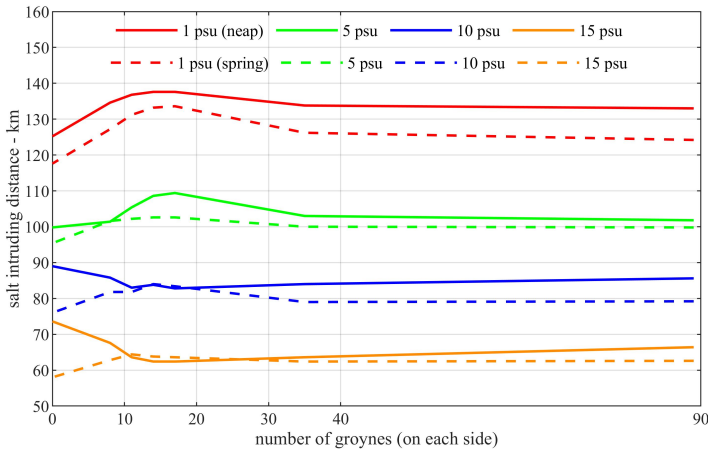
Figure 5.12: Intruding distance of different salinity contour lines in conditions of different groyne number. Intruding distance is the distance from the seaward end of the channel (x = 390 km) to the position of each contour line.

5.4. Discussion
5.4.1. Effects of Groynes on Saltwater Intrusion

Groyne layout substantially influences saltwater intrusion (see the previous section), and in this section we analyze the underlying physical mechanisms. The effects of groynes on saltwater intrusion are discussed from two aspects, (1) impact on channel hydrodynamics, i.e. modifications of tidal propagation due to groynes, and (2) impact on mixing conditions which influence the density-driven circulation and the saltwater intrusion limit.

Tidal Dynamics

The effects of groynes on tidal propagation is evaluated for the M_2 and S_2 tides. Groynes substantially increase tidal velocities in the channel, compared to the non-groyne case (Figure 5.13a and 5.13b). The aspect ratio (also the number of groynes) non-linearly influences the degree of velocity increase, in agreement with the non-linear effects on saltwater intrusion shown in Figure 5.12. The S_2 tide is most strongly influenced by the aspect ratio in Case 4, Case 0, and Case 5 (aspect ratio = 2.0, 2.4, 3.0, respectively). The major velocities of the S_2 tide increase more

strongly (relative to the non-groyne case) than that of the M_2 tide (Figure 5.13).
The combinations of the M_2 and S_2 tides therefore introduce a dependence of tidal
propagation during neap and spring tides on the aspect ratio. During neap tides,
intermediate aspect ratios (2.0 - 3.0) result in the lowest velocities, whereas during
spring tides, intermediate aspect ratios lead to the highest velocities (Figure 5.13c).
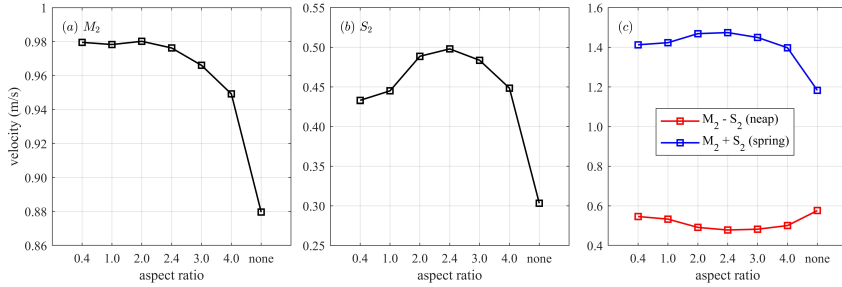
Figure 5.13: Averaged major velocity of M_2 (a), S_2 (b), subtraction and summation of M_2 and S_2 (c)
from x = 310 km to 390 km. Results of M_2 are the same with results in Figure 5.8, results of S_2 are
obtained with the same method for M_2 tide.

The saltwater intrusion on the seaward side can be represented by a high-
salinity contour line (10- to 20-psu) and the saltwater intrusion limit by a lower-
salinity contour line (1-psu). Saltwater intrusion on the seaward side (Figure 5.11
and Figure 5.12) scales with tidal velocities (Figure 5.13c). During neap tides, the
intermediate aspect ratios result in lowest tidal velocities (Figure 5.13c) and the
10-psu (and 15-psu) contour line is located seaward (Figure 5.12). During spring
tides, intermediate aspect ratios result in the highest tidal velocities and the 10-psu
(and 15-psu) contour line is located maximally landward.

However, intermediate aspect ratios lead to the strongest saltwater intrusion
limit during both neap and spring tides (Figure 5.11 and Figure 5.12). Therefore,
the effects of groynes on tidal propagation and salt transport on the seaward side
can affect but cannot fully determine the saltwater intrusion limit. During the neap
tides, landward limits of 1-psu and 10-psu contour lines show opposite correlations
with the aspect ratio (Figure 5.12), indicating other mechanisms are functioning in
addition to the tidal propagation.

Mixing and Stratification
In the North Passage, due to the increased vertical velocity shear, saltwater in-
trusion (and hence the salinity-induced stratification) is most pronounced dur-
ing neap tides [Song et al., 2013]. In this study, the idealized model also shows
stronger saltwater intrusion during neap tides (see 1-psu contour lines in Figure
5.11 and Figure 5.12). As salinity distribution is closely related to mixing and strat-
ification in the channel, we further analyze the stability of the water column. For
this purpose the logarithmic bulk Richardson number ($\log_{10}(R_{ib}/0.25)$) is spatially
averaged for each part of the channel-shoal system to show an overall level of strat-
ification in the river, the main channel, and the groyne fields, respectively (Figure
5.14).
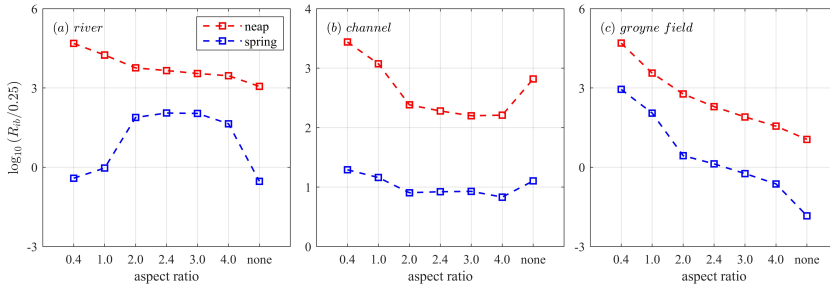
Figure 5.14: Spatially averaged $\log_{10}\left(R_{ib}/0.25\right)$ in the river (a), main channel (b), and the groyne field (c).

During neap tides, the whole system is more strongly stratified than during spring tides (Figure 5.14). Vertical mixing in the main channel is most pronounced for aspect ratios from 2.0 to 4.0, corresponding to more pronounced saltwater intrusion as well (Figure 5.14b). This indicates that during neap tides, saltwater intrusion scales with vertical mixing rates in the main channel (and not to flow velocities, which are lowest during these conditions). During spring tides, mixing rates are higher (compared to the neap tides) but are also less depending on the aspect ratio (Figure 5.14b).

The effects of groyne layout on the vertical mixing are illustrated with the longitudinal salinity distribution in Figure 5.15. In Case 2, 3, and 7 (with low or high aspect ratios), the stratification in the main channel is the strongest (Figure 5.14b), also indicated by 15- and 20-psu contour lines in Figure 5.15a, 5.15b, and 5.15g, which are relatively flat. While in other scenarios, stratification is reduced and the 10- and 20-psu contour lines are steeper (more vertical) with pronounced periodic variations (Figure 5.15c to 5.15f). These variations represent enhanced mixing conditions, with saline near-bed water masses mixing with less saline near-surface waters. This enhanced mixing corresponds to the aspect ratio of groyne fields, i.e. well-mixed conditions occur between every two contiguous groynes. For intermediate aspect ratios, this mixing enhancement appears to be the most significant for the channel section as a whole: for a high aspect ratio periods of mixing enhancement are very infrequent whereas for a low aspect ratio mixing enhancement is less intense.

The channel is more stratified with very weak tidal forcing during neap tides. For cases of intermediate aspect ratios, relatively stronger mixing conditions and groyne-induced mixing enhancement can result in a greater density-driven circulation near the end of the flood tide, strongly impacting on salt intrusion. During spring tides, between-groyne mixing enhancement is even more pronounced (right column of Figure 5.15) compared to neap tides. However, as the spring tides are mixing dominated (Figure 5.14) and much less influenced by the aspect ratio, the relative importance of groyne-related local mixing enhancement is limited. Therefore, the saltwater intrusion limit during spring tides is mainly determined by tidal dynamics (with maximal flow velocities at intermediate aspect ratio), rather than
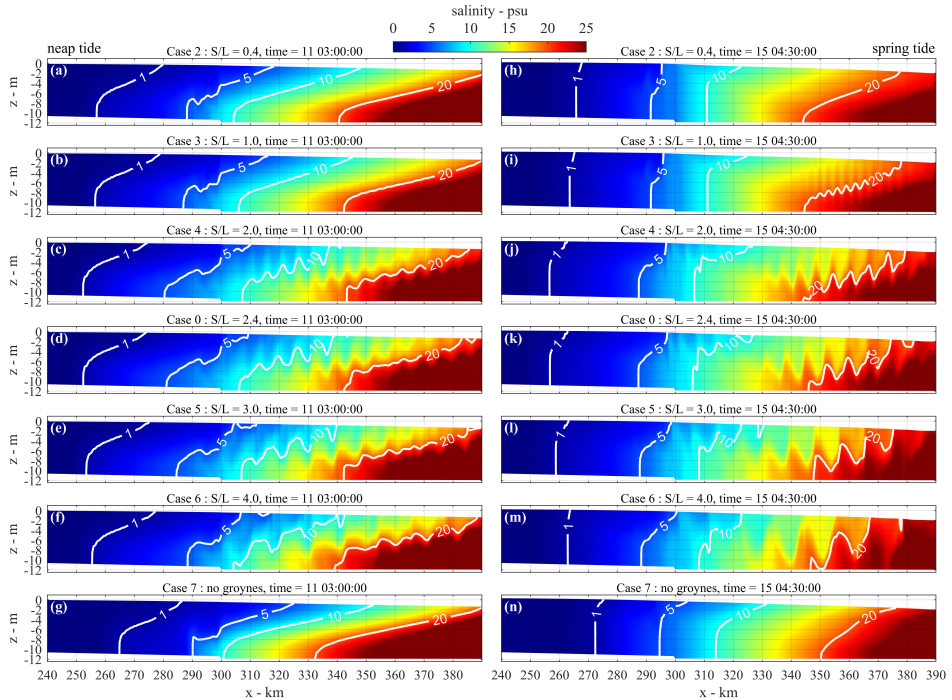
Figure 5.15: Longitudinal salinity distribution on the vertical profile in scenarios with different aspect ratios, at the maximum saltwater intrusion during neap tides (the left column) and spring tides (the right column).

variability in mixing and stratification.

A Synthesis: Horizontal and Vertical Mixing Processes

The HWS salt intrusion has been broadly investigated in the literature [Kuijper and Van Rijn, 2011; Savenije, 1989, 1993; Shaha *et al.*, 2011], using a one-dimensional steady-state advection-dispersion equation and a tidally-averaged dispersion coefficient. This study reveals that groyne layout significantly influences salt intrusion, thereby influencing the dispersion processes. As already concluded by Fischer *et al.* [1979], lateral shear dispersion (longitudinal dispersion due to lateral variations in longitudinal currents) substantially contribute to the overall dispersion coefficient. This so-called tidal dispersion is especially pronounced in estuaries with abrupt topographic changes, with length scales of the major bathymetric features smaller than the tidal excursion [Geyer and Signell, 1992]. The groyne fields in the North Passage provide such pronounced topographic changes, hence significantly contributing to tidal shear dispersion. The mechanisms regulating dispersion may vary over the spring-neap tidal cycle. Based on a dye study in the Hudson River, Geyer *et al.* [2008] observed that tidal dispersion is mainly regulated by vertical shear dispersion during neap tides, but by lateral shear dispersion during spring tides. This spring-neap variation in mixing processes is consistent with our findings
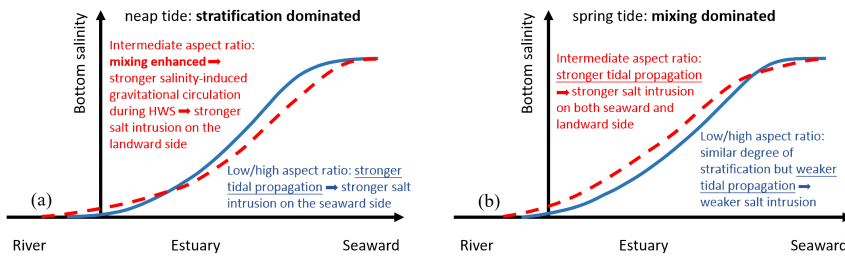
Figure 5.16: Sketch map of saltwater intrusion during neap and spring tides. The x-axis denotes the distance from the river end in seaward direction, and the y-axis is the bottom salinity. The red dashed lines represent scenarios with intermediate aspect ratios.

in the North passage. The exchange between the main channel and the groyne fields is much greater during spring tides than during neap tides (Figure 5.10), indicating a stronger influence on longitudinal currents (hence a larger lateral gradient of longitudinal current velocities). This is also reflected by cases of intermediate aspect ratios in Figure 5.11, the 5-psu salinity contour lines are more landward at the middle of the channel (compared to two sides of the main channel) during spring tides, suggesting greater lateral variations of current velocities hence the greater lateral shear dispersion. During neap tides, for cases of low and high aspect ratios, the water column is more stratified (Figure 5.14) with a greater vertical gradient of longitudinal current velocities, resulting in stronger vertical shear dispersion and stronger saltwater intrusion on the seaward side (Figure 5.15). However, the more pronounced mixing enhancement leads to stronger gravitational circulation during HWS which determines the stronger saltwater intrusion limit on the landward side.

The physical mechanisms for the groynes' effects on saltwater intrusion are summarized in Figure 5.16. Groyne layouts influence both tidal dynamics (and therefore horizontal dispersion) and vertical mixing, which combined determine the saltwater intrusion limit. During neap tides, intermediate aspect ratios lead to weakest vertical shear dispersion but strongest groyne-induced vertical mixing, therefore, resulting in weaker salt intrusion on the seaward side but stronger saltwater intrusion on the landward side. During spring tides, when the channel is vertically well-mixed, salt intrusion is regulated by lateral shear dispersion in response to larger lateral gradient of flow velocities at intermediate aspect ratios. Under these conditions higher flow velocities and larger lateral shear dispersion lead to more pronounced salt intrusion not only on the seaward side but also on the landward side (Figure 5.16b).

5.4.2. Notes on Groynes in Estuaries

Effects of groynes have been widely investigated in the literature. Yossef and de Vriend [2011] designed a laboratory experiment based on the Dutch River Waal, investigating the hydrodynamics near the groyne field. They found that the fluctuating lateral velocity component have significant effects on sediment trans-

port direction and the phase difference between velocity fluctuations is important for sediment budget. Yossef and de Vriend [2010] analyzed the mechanism for sediment exchange and found a net sediment transport into the groyne fields. These findings demonstrate the importance of lateral velocities on mass exchange but have a huge difference with our research, i.e. the salinity-driven current in estuaries. The salinity gradient can induce more complexities in lateral flow and lateral exchange, including asymmetric lateral flows during ebb and flood processes, enhancement of lateral flow at some specific periods, etc. Therefore, in estuarine environments, groyne-affected lateral flows have different and more complex influences on lateral sediment transport, detailed effects should be discussed with consideration for vertical concentration profile. Aforementioned studies also showed difference between emerged and submerged groynes. However, in our idealized model, the groynes are all emerged. The effect of submerged groynes could also be investigated in the future to optimize groyne design.

Typical salinity gradient in estuarine environments also leads to another problem when designing groynes, i.e. saltwater intrusion. This study reveals that groyne layouts can impact both channel hydrodynamics and local mixing conditions, both of which can affect the saltwater intrusion. For design of groynes, caution should be taken that the aim of increasing flow velocity and alleviating sediment siltation may conflict with the need for reducing saltwater intrusion. However, there is not much research on effects of groynes on saltwater intrusion. Therefore, further investigation is necessary for optimizing application of groynes in estuarine environments.

5.4.3. Features of the North Passage

It should be noted that the size of groynes in the North Passage ($\sim$ 2 km) is much larger compared to most of the groyne applications in other systems (typically hundreds of meters at most), for example, about 80 - 150 m in Dutch River Waal [Uijttewaal et al., 2001; Yossef and de Vriend, 2011]. The large dimension brings differences of physical processes compared to other systems. For example, frictional effects in the North Passage may be much smaller than a shallow-water system, as a result, the horizontal eddy could be different from results obtained in laboratory experiments. The large dimension also enhances the influence of Coriolis effects. Therefore, a prototype-based idealized model can be a good tool to investigate effects of groynes.

The Changjiang Estuary has four outlets and the North Passage is one of them. There are mutual impacts between these outlets, which can be reflected by, for example, diversion ratios of water flux and sediment flux. For a large engineering project such as the Deepwater Navigation Channel project in the North Passage, it has large-scale effects on the estuary, modulating the balance between multiple outlets. However, in this study, we pay more attention to direct effects of groynes on the lateral exchange and channel hydrodynamics which can be easily misled by the large-scale effects on the multi-outlet system. Consequently, we use a single-channel idealized model to focus on the relative local but more direct effects induced by groynes. Results presented in this study give insight into deeper understanding of a certain aspect of groynes' effects, and form an important background for further

discussion on the large-scale effects on the whole estuary.

5.5. Conclusions

This study set out to explore the effects of groynes constructed in estuarine environments on hydrodynamics, channel-shoal exchange, and salt intrusion. An idealized model was developed to evaluate the impact of different groyne field scenarios. This idealized model captures the main characteristics of the North Passage in the Changjiang Estuary, in which an extensive groyne field exists.

Firstly, construction of groynes modulate tidal propagation and maintain a high tidal velocity within the main channel. This agrees with the intention of groyne application in navigational channels, i.e. increasing flow velocity and alleviating sediment siltation in the channel. Except for this influence which is from a longitudinal perspective, secondly, groynes in estuaries also affect lateral flow and channel-shoal exchange. For example, due to the retention effect of groynes on salt water during the early ebb, higher salinity in groyne fields will increase density driven lateral flows from groyne fields to the main channel (or reduce flows from the main channel to the groyne fields in other transects) during the late ebb. Combined with high mass concentration (for example, suspended sediment) near the sea bed, the potential effect on mass transport is considerable. These cross-channel exchange flows are primarily driven by baroclinic processes. The salinity gradient causes an asymmetry of lateral currents during ebb and flood periods, for example, enhancing lateral flow during low water slack and weakening that during high water slack. These results indicate that lateral mass transport in such a channel-shoal system is more complicated in estuarine environments compared to riverine environments. Thirdly, groynes influence salt intrusion. Results presented in this study reveal that salt intrusion does not linearly scale with the numbers of groynes (or aspect ratio of the groyne field). Groynes impact both tidal dynamics (influencing horizontal dispersion) and vertical mixing (influencing vertical dispersion and density-driven flows), which jointly determine the degree of salt intrusion in the channel-shoal system. Horizontal dispersion is more dominant during spring tidal conditions, whereas vertical dispersion is more important during neap tidal conditions.

The effects of groynes discussed above are influenced by their specific layout, such as the aspect ratio of groyne fields, bathymetry in the groyne fields, the length of groynes, etc. This study reveals that a smaller aspect ratio constrains horizontal exchange by eddies but enhances lateral gravitational circulation; the opposite is observed for a large aspect ratio. Salt intrusion is maximal for intermediate aspect ratios, which is the result of an optimum in vertical mixing during neap tides, and an optimum in horizontal shear dispersion during spring tides. The Coriolis force can introduce substantial variability in exchange mechanisms on the south and north banks of the channel on the scale of a system such as the North Passage.

To the authors' knowledge, research on effects of groynes in estuarine environments is relatively scarce, however, the demand for groyne application in estuaries is important. This study improves the understanding about groyne application, and provides more perspectives to evaluate designs of groynes. This study also reveals

aspects that need to be addressed in further detail as part of future work, such as the different response of the S_2 and M_2 tides to groyne field layouts and the role of the aspect ratio on tidal dispersion. We also recommend to evaluate the impact of groyne fields on residual sediment transport.

5

6

Concluding Remarks

6.1. General Conclusions

The overarching aim of this thesis is to quantify salt and sediment dynamics in a heavily engineered estuary, and identify the effect of groynes thereon. This aim is pursued with three research questions.

Question 1: How do lateral processes contribute to salt and sediment exchange between the main channel and shoal areas in a tidal channel-shoal system?

Lateral processes impact the salt and sediment exchange mainly by (1) direct advective transport in the lateral direction and (2) the interaction with longitudinal and vertical processes. The direct advective transport of salt and sediment in the lateral direction is influenced by multiple factors such as the salinity-induced baroclinic pressure gradient, channel curvature and other bathymetric features, and the Coriolis effect. Both salt and sediment transported from the shoal areas into the main channel may influence longitudinal transport, resulting in a broader effect of lateral processes on, for example, sediment re-distribution in the system.

Vertical processes (e.g. the settling of sediment) further enhance the importance of lateral processes. The vertical distribution of the sediment concentration and flow velocity induces significant difference of mass transport in the surface and the bottom layers. As a result, sediment exchange between the main channel and shoal areas is considerable despite negligible tidally-averaged residual flow. Of particular importance is a pronounced shoal-to-channel current near the bed occurring around low water slack. This salinity-driven current transports sediment deposited on the shoals towards the main channel.

Lateral processes are also relevant for Question 3, i.e. the effects of groyne fields. The lateral processes mentioned above are influenced by the construction of groynes, and become progressively more important with smaller width-length ratios of the groyne fields. Two aspects are emphasized here. Firstly, the groynes directly impact channel hydrodynamics in both longitudinal and lateral directions (as elaborated above). Secondly, groyne-sheltered areas are low-energy environments in comparison with the main channel, promoting sediment deposition in the groyne fields but also further enhancing the vertical gradient of the mass concentration.

Question 2: What is the temporal variability in water-bed exchange processes, and (how) can this variability be parameterized?

Due to complex sediment-related processes such as flocculation, consolidation, and armoring, the erodibility of sediment is time-varying. Assuming conditions with continuous net deposition, the newly deposited sediment is more easily eroded than the consolidated sediments underneath. This introduces a temporal variability of sediment properties during erosion and deposition processes. The most widely applied erosion and sedimentation model is the K-P model, using a limited number of user-defined input parameters. These input parameters are typically considered constant in time, whereas erosion and sedimentation fluxes may exhibit a temporal variability requiring time-varying input parameters.

In this research, an observation-based running-window fitting method is proposed which can be used to compute time-varying erosion and deposition parameters simultaneously from standard near-bed observations of velocity and the sediment concentration and bed levels. These time-varying parameters can subsequently be analyzed to (1) distinguish whether the time-varying parameters can be equivalently replaced by constant parameters and (2) when (1) applies, provide more realistic combinations of input parameters. For some cases, the measured bed level changes cannot be reproduced using constant parameters, requiring the use of more detailed processes such as consolidation. For conditions where the assumption of constant parameters is valid, the method in this dissertation provides a parameter space that includes all realistic combinations of erosion and deposition parameters, as well as their accuracy.

The newly developed method has three main advantages over conventional methodologies to obtain settling and erosion parameters (such as cameras for settling, laboratory experiments on bed samples for erosion properties). Firstly, the erosion and deposition parameters are continuous (rather than snapshot observations). Secondly, erosion and deposition parameters are coupled. The value of erosion parameters is related to settling parameters, as these occur simultaneously. And thirdly, this new method is much less labor-intensive (both in the field and laboratory) and therefore less costly.

Question 3: How does the impact of groynes in estuarine environments differ from barotropic equivalents, and how do they influence saltwater intrusion?

Groyne fields can store water masses and this storage can introduce a phase lag between water masses in the groyne fields and the main channel, i.e., the retention effects of groynes. For estuarine environments where there is important tidal salinity variation, a significant lateral salinity gradient between the main channel and the groyne fields may occur due to groynes. The lateral gradient drives transverse flows which in turn influence the salt and sediment dynamics in the longitudinal and lateral directions. The groyne-affected salinity-driven lateral processes are the main differences compared to barotropic environments.

Groynes also impact saltwater intrusion in estuaries due to its impact on tidal propagation and on mixing rates in the channel. During neap tide, the channel is stratified, so the enhancement of mixing due to groynes is most important. During spring tide, the channel is vertically well mixed, and in these conditions the effect of groynes on tidal propagation is more important. These effects are influenced by the width-length aspect ratio of groyne fields. Salinity intrusion is highest for conditions with intermediate aspect ratio, and lower for either very high or lower aspect ratios.

These processes are evaluated in this thesis with a schematized single-outlet model. It should be noted that the effects of groynes on saltwater intrusion are more complex for an estuary with multiple outlets. For example, the construction of dikes and groynes in the North Passage greatly impacts the diversion ratio of water flux between outlets. The impact of the aspect ratio of groyne fields in the

North Passage may be less pronounced than our idealized model suggests because (1) saltwater intrusion in the North Passage is weaker than in some of the other outlets, and (2) the balance between multiple channels may impact the role of groyne layouts on saltwater intrusion. The results based on the single-channel idealized model explain the direct effects of groynes and provide a good foundation for further research on the effects of groynes in more complicated systems. It is also important to realize that the groyne field geometry influences the salt and sediment balance, and therefore needs to be considered during the groyne design period. Especially the effect of groynes on saltwater intrusion should be carefully evaluated, given its impact on ecology and freshwater availability near drinking water intakes.

6.2. Recommendations for Further Research

The work presented here suggests that lateral flows and sediment transport are important for a tidal channel-shoal system and can be greatly impacted by engineering constructions such as groynes. These results are obtained with process-based hydrodynamic and suspended sediment transport models. A first recommendation is to extend current models into a morphodynamic model to more vigorously investigate the effects of lateral processes and groynes on channel siltation.

Upscaling the morpho-static sediment transport computations to (long-term) bed level changes requires assumption on sediment properties determining the exchange of particles between the bed and the water column. In-situ observations reveal that these sediment properties are strongly varying over time and are not constant, as many numerical models assume. A second recommendation is to better connect numerical models with the complex reality, by (1) improving near-bed observations (closer to the bed, and including direct observations of the settling velocity), (2) developing simple parameterizations relating bed properties to the available mass of sediment. This may be facilitated with state-of-the-art techniques such as machine learning.

It is concluded that the configuration of groynes (aspect ratio) influences salt-water intrusion. This has not yet been sufficiently investigated in a realistic scenario involving geometric and bathymetric complexities and multiple outlets. A third recommendation is therefore to investigate in more detail the role of groyne layout on saltwater intrusion in a complex configuration, including the effect of flow redistribution over multiple outlets. Moreover, the contribution of groynes to sediment transport and morphodynamics has not yet been sufficiently assessed.

A

Appendix

A.1. Calculation for Bed Shear Stress (In Chapter 4)

In K-P model, bed shear stress (τ) is key input information. Here we used two methods to calculate the bed shear stress. The first method is the Grant-Madsen model [Madsen, 1994]. The current induced bed shear stress (τ_c) is calculated as:

$$\tau_c = \rho_w (u_{*c})^2 \tag{A.1}$$

where ρ_w is the water density, u_{*c} is the current friction velocity. u_{*c} can be solved iteratively with the following equation - see Madsen [1994] for details:

$$u_{*c} = \frac{u_{*r}}{2} \frac{\ln(z_r/\delta_{wc})}{\ln(\delta_{wc}/z_0)} \left(-1 + \sqrt{1 + \frac{4\kappa \ln(\delta_{wc}/z_0)}{(\ln(z_r/\delta_{wc}))^2} \frac{u_{cr}}{u_{*r}}} \right) \tag{A.2}$$

where u_{*r} is the wave-current combined friction vlocity; δ_{wc} is the height of the wave boundary layer; z_0 is the characteristic roughness length which can be derived from $z_0 = k_N/30$, k_N is the equivalent Nikuradse sand grain roughness of the bottom which is related to the median grain size of suspended particles (d_{50}) using $k_N = 2.5 \cdot d_{50}$; $\kappa = 0.4$ is the von-Karman constant; u_{cr} is the current velocity at the height z_r.

The wave-related bed shear stress τ_w is calculated with:

$$\tau_w = \rho_w (u_{*wm})^2 \tag{A.3}$$

where u_{*wm} is the maximum wave friction velocity. The wave-current combined shear stress (τ_{cw}) is calculated as:

$$\tau_{cw} = \sqrt{(\tau_w + \tau_c |\cos\phi_{cw}|)^2 + (\tau_c \sin\phi_{cw})^2} \tag{A.4}$$

where ϕ_{cw} is the angle between the current and the wave. Note that the water depth exceeds 10 meters in the main channel of the NP. However, the observed significant wave height was below 0.3 m, and therefore the effect of waves on the bed shear stress can be omitted (see Figure A.1). For the K-P model in this study, τ_c was therefore used as τ.

An assumption in the method for computing τ_c is that the flow velocity profile is logarithmic, which is valid only for steady flows [Cheng *et al.*, 1999]. Therefore, we also used another method based on turbulent kinetic energy (TKE):

$$TKE = \frac{1}{2}\rho \left(\overline{u'^2} + \overline{v'^2} + \overline{w'^2} \right) \tag{A.5}$$

where u^2, v^2, w^2 are fluctuating velocity components in the XYZ coordinate which can be acquired by ADV, the overbar denotes time-averaging values. Then TKE-based bed shear stress can be calculated with the equation:

$$\tau = C \cdot TKE \tag{A.6}$$

where C is a proportionality constant which equals to 0.19 [Soulsby, 1983] or 0.20 [Soulsby and Dyer, 1981]. We applied $C = 0.19$ in this study.
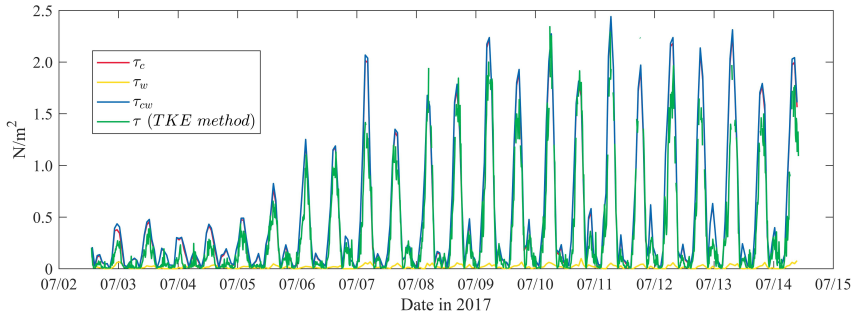
Figure A.1: Calculation of bed shear stress, comparison between Grant-Madsen method and the TKE method. The red and blue line largely overlap because the wave-induced shear stress (yellow line) is very small.

Two methods for calculating bed shear stress showed good agreement (Figure A.1) suggesting both methods can therefore be applied to our data. The TKE-method does not require an assumption for the bed roughness (z_0). It only requires the velocity fluctuation (from the ADV) and density (acquired with the OBS), and these two instruments can form the simplest setting that satisfies the needs of observational data used in this study. However, during our observations the ADV regularly measured blanks (see the green line in Figure A.1) for reasons not fully understood, but possibly related to hard reflections from the bed. With the ADCP measuring complete timeseries, for our application the Grant Madsen approach was more applicable for computation of the bed shear stress.

A.2. ADV Raw Data (In Chapter 4)

Relative bed level (unit: [mm]), correlation (non-dimensional), and noise amplitude (unit: [counts]) are normalized ($X = (X - X_{min})/(X_{max} - X_{min})$) and shown in Figure A.2. For each period of blank RBL, the noise amplitude is high and the correlation is low, supporting our hypothesis of a hard, non-erodible layer.
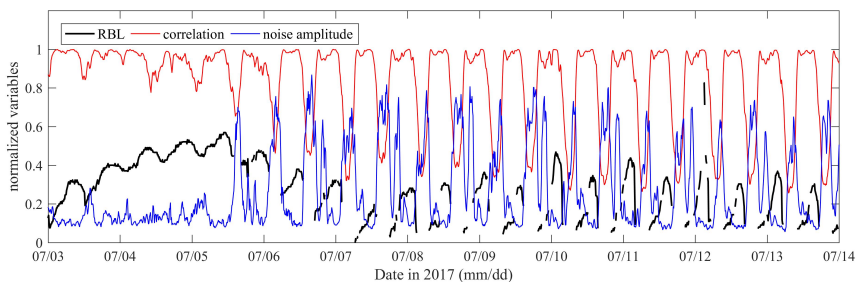

Figure A.2: Calculation of bed shear stress, comparison between Grant-Madsen method and the TKE method. The red and blue line largely overlap because the wave-induced shear stress (yellow line) is very small.

A

A.3. Lateral Flow During Neap and Spring Tides (In Chapter 5)
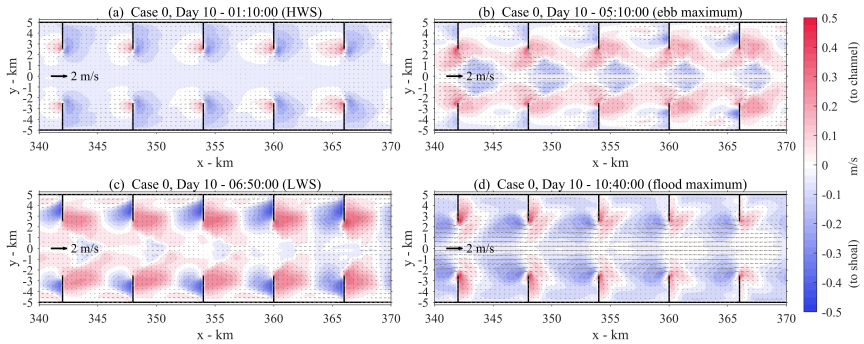
Figure A.3: Bottom lateral current velocities and velocity vectors at (a) HWS, (b) ebb maximum, (c) LWS, and (d) flood maximum. Positive value indicates a direction from groyne fields to the main channel (from both sides). These results are from Case 0 in neap conditions. Three cross-channel and one along-channel transects are marked with cyan dashed lines for the following analysis. HWS, high water slack, LWS, low water slack.
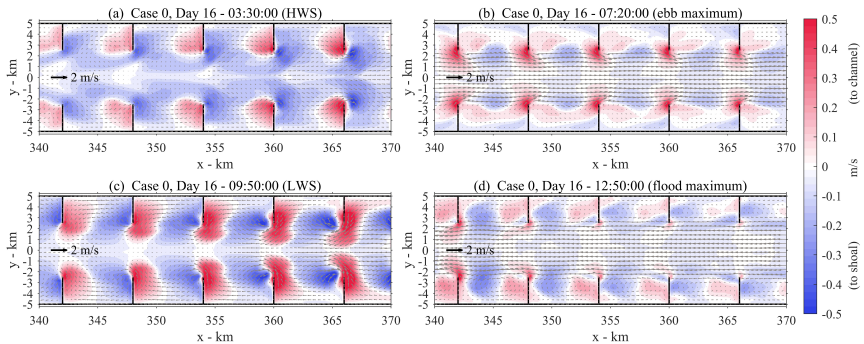

Figure A.4: Bottom lateral current velocities and velocity vectors at (a) HWS, (b) ebb maximum, (c) LWS, and (d) flood maximum. Positive value indicates a direction from groyne fields to the main channel (from both sides). These results are from Case 0 in spring conditions. Three cross-channel and one along-channel transects are marked with cyan dashed lines for the following analysis. HWS, high water slack, LWS, low water slack.

A.4. Horizontal Circulation Cells at the Surface Layer (In Chapter 5)
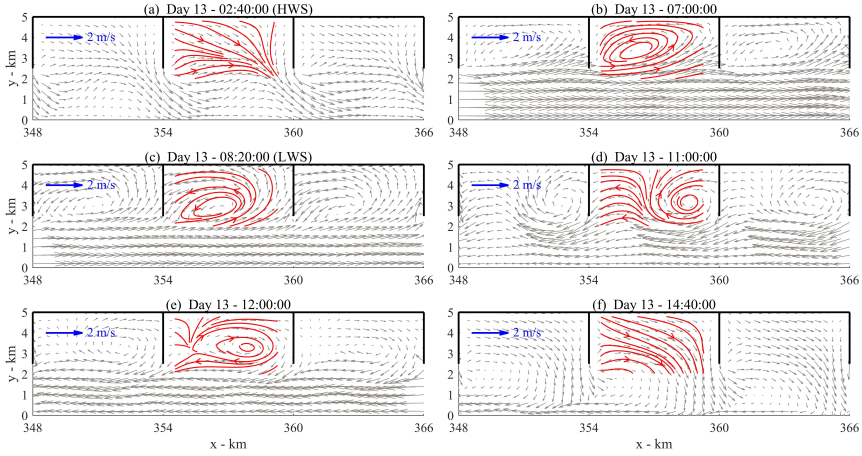
Figure A.5: Velocity vectors (grey arrows) in the main channel and streamlines (red lines) in the groyne field during moderate tides, blue arrows are length scales for velocity vectors. Velocity data is from the surface layer of Case 0.

References

D. A. Ross, *Introduction to oceanography* (HarperCollins College Publishers, New York, NY, 1995).

S. L. Yang, K. H. Xu, J. D. Milliman, H. F. Yang, and C. S. Wu, *Decline of Yangtze River water and sediment discharge: Impact from natural and anthropogenic changes,* Scientific Reports **5**, 1 (2015).

J. Ge, Z. Zhou, W. Yang, P. Ding, C. Chen, Z. B. Wang, and J. Gu, *Formation of Concentrated Benthic Suspension in a Time-Dependent Salt Wedge Estuary,* Journal of Geophysical Research: Oceans **123**, 8581 (2018).

J. Lin, B. C. van Prooijen, L. Guo, C. Zhu, Q. He, and Z. B. Wang, *Regime shifts in the Changjiang (Yangtze River) Estuary: The role of concentrated benthic suspensions,* Marine Geology **433**, 106403 (2021).

K. Hu and P. Ding, *The effect of deep waterway constructions on hydrodynamics and salinities in Yangtze Estuary, China,* Journal of Coastal Research **II**, 961 (2009).

J. A. Stallins, *Geomorphology and ecology: Unifying themes for complex systems in biogeomorphology,* Geomorphology **77**, 207 (2006).

N. S. Haussmann, *Biogeomorphology: Understanding different research approaches,* Earth Surface Processes and Landforms **36**, 136 (2011).

L. A. Naylor, *The contributions of biogeomorphology to the emerging field of geobiology,* in *Geobiology: Objectives, Concepts, Perspectives* (Elsevier, 2005) pp. 35–51.

B. C. Van Prooijen, F. Montserrat, and P. M. Herman, *A process-based model for erosion of Macoma balthica-affected mud beds,* Continental Shelf Research **31**, 527 (2011).

C. R. Ariathurai, *A finite element model for sediment transport in estuaries* (University of California, Davis., 1974).

R. B. Krone, B. H. E. L. University of California, and B. S. E. R. L. University of California, *Flume Studies of the Transport of Sediment in Estuarial Shoaling Processes: Final Report* (Hydraulic Engineering Laboratory and Sanitary Engineering Research Laboratory, University of California, 1962).

E. A. Partheniades, *Erosion and Deposition of Cohesive Soils,* Jour of the Hydraulics Div **1**, 190 (1965).

J. C. Winterwerp and W. G. M. van Kesteren, *Developments in sedimentology* (Elsevier, Amsterdam, Netherlands, 2004) p. 576.

Z. Zhou, J. Ge, Z. B. Wang, D. S. Maren, J. Ma, and P. Ding, *Study of Lateral Flow in a Stratified Tidal Channel - Shoal System: The Importance of Intratidal Salinity Variation,* Journal of Geophysical Research: Oceans **124**, 6702 (2019).

Z. Zhou, J. Ge, D. S. van Maren, Z. B. Wang, Y. Kuai, and P. Ding, *Study of Sediment Transport in a Tidal Channel - shoal System: Lateral Effects and Slack□Water Dynamics,* Journal of Geophysical Research: Oceans **126** (2021), 10.1029/2020JC016334.

C. D. Woodroffe, R. J. Nicholls, Y. Saito, Z. Chen, and S. L. Goodbred, *Landscape variability and the response of Asian megadeltas to environmental change,* in *Global change and integrated coastal management* (Springer, 2006) pp. 277–314.

H. Postma, *Sediment transport and sedimentation in the estuarine environment,* in *Estuaries*, edited by G. Lauff (American Association for the Advancement of Science, Washington DC, 1967) pp. 158–179.

K. R. Dyer, *Coastal and Estuarine Sediment Dynamics* (John Wiley and Sons, CHICHESTER, SUSSEX (UK), 1986) p. 358.

A. Dube, G. Jayaraman, and R. Rani, *Modelling the effects of variable salinity on the temporal distribution of plankton in shallow coastal lagoons,* Journal of Hydro-Environment Research **4**, 199 (2010), arXiv:1211.6954 [astro-ph.CO] .

M. M. Bowen, *Salt transport and the time-dependent salt balance of a partially stratified estuary,* Journal of Geophysical Research **108**, 3158 (2003).

H. B. Fischer, *Mixing and Dispersion in Estuaries,* Annual Review of Fluid Mechanics **8**, 107 (1976).

J. H. Simpson, J. Brown, J. Matthews, and G. Allen, *Tidal Straining, Density Currents, and Stirring in the Control of Estuarine Stratification,* Estuaries **13**, 125 (1990).

J. A. Lerczak and W. Rockwell Geyer, *Modeling the Lateral Circulation in Straight, Stratified Estuaries*,* Journal of Physical Oceanography **34**, 1410 (2004).

K. M. Huijts, H. M. Schuttelaars, H. E. de Swart, and A. Valle-Levinson, *Lateral entrapment of sediment in tidal estuaries: An idealized model study,* Journal of Geophysical Research: Oceans **111**, 1 (2006).

D. C. Fugate, C. T. Friedrichs, and L. P. Sanford, *Lateral dynamics and associated transport of sediment in the upper reaches of a partially mixed estuary, Chesapeake Bay, USA,* Continental Shelf Research **27**, 679 (2007).

A

L. Zhu, Q. He, and J. Shen, *Modeling lateral circulation and its influence on the along-channel flow in a branched estuary,* Ocean Dynamics **68**, 177 (2018).

Z. Wang, D. Van Maren, P. Ding, S. Yang, B. Van Prooijen, P. De Vet, J. Winterwerp, H. De Vriend, M. Stive, and Q. He, *Human impacts on morphodynamic thresholds in estuarine systems,* Continental Shelf Research **111**, 174 (2015).

W. Chen and H. E. de Swart, *Longitudinal variation in lateral trapping of fine sediment in tidal estuaries: observations and a 3D exploratory model,* Ocean Dynamics **68**, 309 (2018).

J. Ge, F. Shen, W. Guo, C. Chen, and P. Ding, *Estimation of critical shear stress for erosion in the Changjiang Estuary: A synergy research of observation, GOCI sensing and modeling,* Journal of Geophysical Research: Oceans **120**, 8439 (2015), arXiv:arXiv:1402.6991v1 .

G. Liu, J. Zhu, Y. Wang, H. Wu, and J. Wu, *Tripod measured residual currents and sediment flux: Impacts on the silting of the Deepwater Navigation Channel in the Changjiang Estuary,* Estuarine, Coastal and Shelf Science **93**, 192 (2011).

J. Ge, C. Chen, J. Qi, P. Ding, and R. C. Beardsley, *A dike–groyne algorithm in a terrain-following coordinate ocean model (FVCOM): Development, validation and application,* Ocean Modelling **47**, 26 (2012).

J. Wu, J. T. Liu, and X. Wang, *Sediment trapping of turbidity maxima in the Changjiang Estuary,* Marine Geology **303-306**, 14 (2012).

J. Ge, P. Ding, C. Chen, S. Hu, G. Fu, and L. Wu, *An integrated East China Sea-Changjiang Estuary model system with aim at resolving multi-scale regional-shelf-estuarine dynamics,* Ocean Dynamics **63**, 881 (2013).

Z. Lai, C. Chen, G. W. Cowles, and R. C. Beardsley, *A nonhydrostatic version of FVCOM: 1. Validation experiments,* Journal of Geophysical Research: Oceans **115** (2010), 10.1029/2009JC005525.

G. D. Egbert and S. Y. Erofeeva, *Efficient Inverse Modeling of Barotropic Ocean Tides,* Journal of Atmospheric and Oceanic Technology **19**, 183 (2002), arXiv:1520-0426(2002)019<0183:EIMOBO>2.0.CO;2 [10.1175] .

C. Chen, H. Liu, and R. C. Beardsley, *An unstructured grid, finite-volume, three-dimensional, primitive equations ocean model: Application to coastal ocean and estuaries,* Journal of Atmospheric and Oceanic Technology **20**, 159 (2003).

B. Galperin, L. H. Kantha, S. Hassid, and A. Rosati, *A Quasi-equilibrium Turbulent Energy Model for Geophysical Flows,* Journal of the Atmospheric Sciences **45**, 55 (1988).

G. L. Mellor and T. Yamada, *Development of a turbulence closure model for geophysical fluid problems,* Reviews of Geophysics **20**, 851 (1982), arXiv:82/002R-0808 [0034-6853] .

A

C. Chen, R. Beardsley, G. Cowles, J. Qi, Z. Lai, G. Gao, D. Stuebe, Q. Xu, P. Xue, J. Ge, S. Hu, and Ji, *An unstructured grid, Finite-Volume Coastal Ocean Model FVCOM – User Manual,* Tech. Rep., SMAST/UMASSD-13-0701, Sch. for Mar. Sci. and Technol., Univ. of Mass. Dartmouth, New Bedford. **C**, 416 pp (2013), arXiv:arXiv:1011.1669v3 .

J. Ge, P. Ding, and C. Chen, *Low-salinity plume detachment under non-uniform summer wind off the Changjiang Estuary,* Estuarine, Coastal and Shelf Science **156**, 61 (2014).

W. Guo, X. H. Wang, P. Ding, J. Ge, and D. Song, *A system shift in tidal choking due to the construction of Yangshan Harbour, Shanghai, China,* Estuarine, Coastal and Shelf Science **206**, 49 (2018a).

R. J. Chant, *Estuarine secondary circulation,* in *Contemporary Issues in Estuarine Physics*, edited by A. Valle-Levinson (Cambridge University Press, Cambridge, 2010) pp. 100–124.

Y. H. Kim and G. Voulgaris, *Lateral circulation and suspended sediment transport in a curved estuarine channel: Winyah Bay, SC, USA,* Journal of Geophysical Research: Oceans **113**, 1 (2008).

J. R. Lacy and C. R. Sherwood, *Accuracy of a pulse-coherent acoustic Doppler profiler in a wave-dominated flow,* Journal of Atmospheric and Oceanic Technology **21**, 1448 (2004).

N. J. Nidzieko, J. L. Hench, and S. G. Monismith, *Lateral Circulation in Well-Mixed and Stratified Estuarine Flows with Curvature,* Journal of Physical Oceanography **39**, 831 (2009).

A. J. Hoitink, D. S. van Maren, and P. Hoekstra, *Mixing and stratification in a tropical tidal embayment subject to a distributed freshwater source,* Journal of Marine Systems **88**, 34 (2011).

R. Lewis, *Dispersion in Estuaries and Coastal Waters*, Theory and Interpretation of (Wiley, 1997).

W. Brevis, M. García-Villalba, and Y. Niño, *Experimental and large eddy simulation study of the flow developed by a sequence of lateral obstacles,* Environmental Fluid Mechanics **14**, 873 (2014).

A. McCoy, G. Constantinescu, and L. J. Weber, *Numerical Investigation of Flow Hydrodynamics in a Channel with a Series of Groynes,* Journal of Hydraulic Engineering **134**, 157 (2008).

A. N. Sukhodolov, *Hydrodynamics of groyne fields in a straight river reach: Insight from field experiments,* Journal of Hydraulic Research **52**, 105 (2014).

A. McCoy, G. Constantinescu, and L. Weber, *A numerical investigation of coherent structures and mass exchange processes in channel flow with two lateral submerged groynes,* Water Resources Research **43**, 1 (2007).

W. S. J. Uijttewaal, D. Lehmann, and A. van Mazijk, *Exchange processes between a river and its groyne fields: Model experiments,* Journal of Hydraulic Engineering **127**, 928 (2001).

V. Weitbrecht, S. A. Socolofsky, and G. H. Jirka, *Experiments on Mass Exchange between Groin Fields and Main Stream in Rivers,* Journal of Hydraulic Engineering **134**, 173 (2008).

D. Song, X. H. Wang, Z. Cao, and W. Guan, *Suspended sediment transport in the Deepwater Navigation Channel, Yangtze River Estuary, China, in the dry season 2009: 1. Observations over spring and neap tidal cycles,* Journal of Geophysical Research: Oceans **118**, 5555 (2013).

D. K. Ralston, W. R. Geyer, and J. C. Warner, *Bathymetric controls on sediment transport in the Hudson River estuary: Lateral asymmetry and frontal trapping,* Journal of Geophysical Research: Oceans **117**, n/a (2012).

P. J. Wood, *Biological Effects of Fine Sediment in the Lotic Environment,* Environmental Management **21**, 203 (1997).

L. Guo, N. Su, C. Zhu, and Q. He, *How have the river discharges and sediment loads changed in the Changjiang River basin downstream of the Three Gorges Dam?* Journal of Hydrology **560**, 259 (2018b).

J. P. M. Syvitski, *Impact of Humans on the Flux of Terrestrial Sediment to the Global Coastal Ocean,* Science **308**, 376 (2005).

D. E. Walling and D. Fang, *Recent trends in the suspended sediment loads of the world's rivers,* Global and Planetary Change **39**, 111 (2003).

K. R. Dyer, *Fine Sediment Particle Transport in Estuaries,* in *Physical Processes in Estuaries* (Springer Berlin Heidelberg, Berlin, Heidelberg, 1988) pp. 295–310.

C. B. Officer, *Physical dynamics of estuarine suspended sediments,* Marine Geology **40**, 1 (1981).

D. A. Jay and J. D. Musiak, *Particle trapping in estuarine tidal flows,* Journal of Geophysical Research **99**, 20445 (1994).

H. Postma, *Transport and accumulation of suspended matter in the Dutch Wadden Sea,* Netherlands Journal of Sea Research **1**, 148 (1961).

M. A. de Nijs and J. D. Pietrzak, *Saltwater intrusion and ETM dynamics in a tidally-energetic stratified estuary,* Ocean Modelling **49-50**, 60 (2012).

A

A

J. M. McSweeney, R. J. Chant, and C. K. Sommerfield, *Lateral variability of sediment transport in the Delaware Estuary,* Journal of Geophysical Research: Oceans **121**, 725 (2016).

H. Burchard, H. M. Schuttelaars, and D. K. Ralston, *Sediment Trapping in Estuaries,* Annual Review of Marine Science **10**, 371 (2018).

J. Dronkers, *The influence of buoyancy on transverse circulation and on estuarine dynamics,* Coastal and Estuarine Studies , 341 (1996).

S. N. Chen, L. P. Sanford, and D. K. Ralston, *Lateral circulation and sediment transport driven by axial winds in an idealized, partially mixed estuary,* Journal of Geophysical Research: Oceans **114**, 1 (2009).

S. E. Kristensen, N. Drønen, R. Deigaard, and J. Fredsoe, *Impact of groyne fields on the littoral drift: A hybrid morphological modelling study,* Coastal Engineering **111**, 13 (2016).

T. Scott, M. Austin, G. Masselink, and P. Russell, *Dynamics of rip currents associated with groynes - field measurements, modelling and implications for beach safety,* Coastal Engineering **107**, 53 (2016).

S. Ouillon and D. Dartus, *Three-Dimensional Computation of Flow around Groyne,* Journal of Hydraulic Engineering **123**, 962 (1997).

H. L. Luan, P. X. Ding, Z. B. Wang, S. L. Yang, and J. Y. Lu, *Morphodynamic impacts of large-scale engineering projects in the Yangtze River delta,* Coastal Engineering **141**, 1 (2018).

L. Guo and Q. He, *Freshwater flocculation of suspended sediments in the Yangtze River, China,* Ocean Dynamics **61**, 371 (2011).

H. L. Luan, P. X. Ding, Z. B. Wang, J. Z. Ge, and S. L. Yang, *Decadal morphological evolution of the Yangtze Estuary in response to river input changes and estuarine engineering projects,* Geomorphology **265**, 12 (2016).

S. L. Yang, J. D. Milliman, K. H. Xu, B. Deng, X. Y. Zhang, and X. X. Luo, *Downstream sedimentary and geomorphic impacts of the Three Gorges Dam on the Yangtze River,* Earth-Science Reviews **138**, 469 (2014a).

L. Wu, C. Chen, P. Guo, M. Shi, J. Qi, and J. Ge, *A FVCOM-based unstructured grid wave, current, sediment transport model, I. Model description and validation,* Journal of Ocean University of China **10**, 1 (2011).

L. Zheng, C. Chen, M. Alber, and H. Liu, *A modeling study of the Satilla River estuary, Georgia. II: Suspended sediment,* Estuaries **26**, 670 (2003).

R. Uncles, R. Elliott, and S. Weston, *Lateral Distributions of Water, Salt and Sediment Transport in a Partly Mixed Estuary,* in *Coastal Engineering 1984* (American Society of Civil Engineers, New York, NY, 1985) pp. 3067–3077.

M. Fettweis, F. Francken, V. Pison, and D. Van den Eynde, *Suspended particulate matter dynamics and aggregate sizes in a high turbidity area,* Marine Geology **235**, 63 (2006).

K. Hu, P. Ding, Z. Wang, and S. Yang, *A 2D/3D hydrodynamic and sediment transport model for the Yangtze Estuary, China,* Journal of Marine Systems **77**, 114 (2009).

D. J. Nowacki and N. K. Ganju, *Storm impacts on hydrodynamics and suspended-sediment fluxes in a microtidal back-barrier estuary,* Marine Geology **404**, 1 (2018).

J. C. Winterwerp, *Stratification effects by cohesive and noncohesive sediment,* Journal of Geophysical Research: Oceans **106**, 22559 (2001).

J. C. Winterwerp, *Stratification effects by fine suspended sediment at low, medium, and very high concentrations,* Journal of Geophysical Research **111**, C05012 (2006).

R. Uncles, R. Elliott, and S. Weston, *Observed fluxes of water, salt and suspended sediment in a partly mixed estuary,* Estuarine, Coastal and Shelf Science **20**, 147 (1985b).

L. Chen, W. Gong, H. Zhang, L. Zhu, and W. Cheng, *Lateral Circulation and Associated Sediment Transport in a Convergent Estuary,* Journal of Geophysical Research: Oceans **125**, 1 (2020).

Z. Yang, H. E. de Swart, H. Cheng, C. Jiang, and A. Valle-Levinson, *Modelling lateral entrapment of suspended sediment in estuaries: The role of spatial lags in settling and M4 tidal flow,* Continental Shelf Research **85**, 126 (2014b).

P. J. T. Dankers and J. C. Winterwerp, *Hindered settling of mud flocs: Theory and validation,* Continental Shelf Research **27**, 1893 (2007).

W. R. Geyer, R. Signell, and G. Kineke, *Lateral trapping of sediment in a partially mixed estuary,* in *Physics of Estuaries and Coastal Seas: Proceedings of the 8th International Biennial Conference on Physics of Estuaries and Coastal Seas*, edited by J. Dronkers and M. Scheffers (Balkema, 1998) pp. 115–124.

D. S. van Maren, T. van Kessel, K. Cronin, and L. Sittoni, *The impact of channel deepening and dredging on estuarine sediment concentration,* Continental Shelf Research **95**, 1 (2015).

R. F. Hesse, A. Zorndt, and P. Fröhle, *Modelling dynamics of the estuarine turbidity maximum and local net deposition,* Ocean Dynamics **69**, 489 (2019).

L. P. Sanford and J. P. Halka, *Assessing the paradigm of mutually exclusive erosion and deposition of mud, with examples from upper Chesapeake Bay,* Marine Geology **114**, 37 (1993).

A

A

J. Winterwerp, *Proceedings in Marine Science*, Vol. 8 (Elsevier B.V., 2007) pp. 209–226.

U. Lumborg, *Modelling the deposition, erosion, and flux of cohesive sediment through Øresund*, Journal of Marine Systems **56**, 179 (2005).

Q. Zhu, S. Yang, and Y. Ma, *Intra-tidal sedimentary processes associated with combined wave-current action on an exposed, erosional mudflat, southeastern Yangtze River Delta, China*, Marine Geology **347**, 95 (2014).

Q. Zhu, B. van Prooijen, Z. Wang, and S. Yang, *Bed-level changes on intertidal wetland in response to waves and tides: A case study from the Yangtze River Delta*, Marine Geology **385**, 160 (2017).

Y. M. Dijkstra, H. M. Schuttelaars, G. P. Schramkowski, and R. L. Brouwer, *Modeling the Transition to High Sediment Concentrations as a Response to Channel Deepening in the Ems River Estuary*, Journal of Geophysical Research: Oceans **124**, 1578 (2019).

D. S. van Maren, J. C. Winterwerp, B. S. Wu, and J. J. Zhou, *Modelling hyperconcentrated flow in the Yellow River*, Earth Surface Processes and Landforms **34**, 596 (2009).

L. P. Sanford, *Modeling a dynamically varying mixed sediment bed with erosion, deposition, bioturbation, consolidation, and armoring*, Computers and Geosciences **34**, 1263 (2008).

J. C. Winterwerp, Z. Zhou, G. Battista, T. Van Kessel, H. R. A. Jagers, D. S. Van Maren, and M. Van Der Wegen, *Efficient Consolidation Model for Morphodynamic Simulations in Low-SPM Environments*, Journal of Hydraulic Engineering **144**, 04018055 (2018).

Z. Zhou, M. van der Wegen, B. Jagers, and G. Coco, *Modelling the role of self-weight consolidation on the morphodynamics of accretional mudflats*, Environmental Modelling and Software **76**, 167 (2016).

K. Dyer, J. Cornelisse, M. Dearnaley, M. Fennessy, S. Jones, J. Kappenberg, I. McCave, M. Pejrup, W. Puls, W. Van Leussen, and K. Wolfstein, *A comparison of in situ techniques for estuarine floc settling velocity measurements*, Journal of Sea Research **36**, 15 (1996).

S. E. Jones and C. F. Jago, *Determination of settling velocity in the Elbe estuary using Quisset tubes*, Journal of Sea Research **36**, 63 (1996).

J. P. Maa and J. I. Kwon, *Using ADV for cohesive sediment settling velocity measurements*, Estuarine, Coastal and Shelf Science **73**, 351 (2007).

D. C. Fugate and C. T. Friedrichs, *Determining concentration and fall velocity of estuarine particle populations using adv, obs and lisst*, Continental Shelf Research **22**, 1867 (2002).

N. Williams, D. Walling, and G. Leeks, *The settling behaviour of fine sediment particles: some preliminary results from LISST instruments,* Sediment Transfer througlt the Fluvial System , 283 (2004).

M. J. Fennessy, K. R. Dyer, and D. A. Huntley, *inssev: An instrument to measure the size and settling velocity of flocs in situ,* Marine Geology **117**, 107 (1994).

A. Manning and K. Dyer, *A laboratory examination of floc characteristics with regard to turbulent shearing,* Marine Geology **160**, 147 (1999).

R. Sternberg, A. Ogston, and R. Johnson, *A video system for in situ measurement of size and settling velocity of suspended particulates,* Journal of Sea Research **36**, 127 (1996).

W. van Leussen and J. M. Cornelisse, *The underwater video system VIS,* Journal of Sea Research **36**, 77 (1996).

N. S. Cheng, *Comparison of formulas for drag coefficient and settling velocity of spherical particles,* Powder Technology **189**, 395 (2009).

K. She, L. Trim, and D. Pope, *Fall velocities of natural sediment particles: A simple mathematical presentation of the fall velocity law,* Journal of Hydraulic Research **43**, 189 (2005).

J. P. Ahrens, *A Fall-Velocity Equation,* Journal of Waterway, Port, Coastal, and Ocean Engineering **126**, 99 (2000).

H. J. Nasiha and P. Shanmugam, *Estimation of settling velocity of sediment particles in estuarine and coastal waters,* Estuarine, Coastal and Shelf Science **203**, 59 (2018).

J. C. Winterwerp, *Fine sediment transport by tidal asymmetry in the high-concentrated Ems River: Indications for a regime shift in response to channel deepening,* Ocean Dynamics **61**, 203 (2011).

B. Shi, Y. P. Wang, L. H. Wang, P. Li, J. Gao, F. Xing, and J. D. Chen, *Great differences in the critical erosion threshold between surface and subsurface sediments: A field investigation of an intertidal mudflat, Jiangsu, China,* Estuarine, Coastal and Shelf Science **206**, 76 (2018).

K. Taki, *Critical shear stress for cohesive sediment transport,* in *Proceedings in Marine Science*, Vol. 3 (Elsevier, 2000) pp. 53–61.

D. S. van Maren and K. Cronin, *Uncertainty in complex three-dimensional sediment transport models: equifinality in a model application of the Ems Estuary, the Netherlands,* Ocean Dynamics **66**, 1665 (2016).

S. B. Dai and X. X. Lu, *Sediment load change in the Yangtze River (Changjiang): A review,* Geomorphology **215**, 60 (2014).

A

J. Ge, C. Chen, Z. B. Wang, K. Ke, J. Yi, and P. Ding, *Dynamic Response of the Fluid Mud to a Tropical Storm,* Journal of Geophysical Research: Oceans **125**, 1 (2020).

R. Whitehouse, R. Soulsby, W. Roberts, and H. Mitchener, *Dynamics of estuarine muds* (Thomas Telford Publishing, 2000).

O. S. Madsen, *Spectral Wave-Current Bottom Boundary Layer Flows,* in *Coastal Engineering 1994* (American Society of Civil Engineers, New York, NY, 1994) pp. 384–398.

P. Dankers, J. Winterwerp, and W. van Kesteren, *A preliminary study on the hindered settling of kaolinite flocs,* in *Proceedings in Marine Science*, Vol. 8 (Elsevier B.V., 2007) pp. 227–241.

J. D. Milliman, S. Huang-ting, Y. Zuo-sheng, and R. H. Mead, *Transport and deposition of river sediment in the Changjiang estuary and adjacent continental shelf,* Continental Shelf Research **4**, 37 (1985).

G. Jiang, Y. Yao, and Z. Tang, *Analysis for influencing factors of fine sediment flocculation in the Changjiang Estuary,* Acta Oceanologica Sinica **21**, 385 (2002).

Y. Wan, H. Wu, D. Roelvink, and F. Gu, *Experimental study on fall velocity of fine sediment in the Yangtze Estuary, China,* Ocean Engineering **103**, 180 (2015).

J. C. Winterwerp, W. G. M. van Kesteren, B. van Prooijen, and W. Jacobs, *A conceptual framework for shear flow-induced erosion of soft cohesive sediment beds,* Journal of Geophysical Research: Oceans **117**, n/a (2012).

R. E. Gibson, G. L. England, and M. J. L. Hussey, *The Theory of One-Dimensional Consolidation of Saturated Clays,* Géotechnique **17**, 261 (1967).

V. Krivtsov, J. Gascoigne, and S. Jones, *Harmonic analysis of suspended particulate matter in the Menai Strait (UK),* Ecological Modelling **212**, 53 (2008).

M. R. Nayak, W. J. Emery, and R. E. Thomson, *Data Analysis Methods in Physical Oceanography,* Estuaries **22**, 728 (1999).

A. R. Weeks, J. H. Simpson, and D. Bowers, *The relationship between concentrations of suspended particulate material and tidal processes in the Irish Sea,* Continental Shelf Research **13**, 1325 (1993).

A. Sukhodolov, W. S. Uijttewaal, and C. Engelhardt, *On the correspondence between morphological and hydrodynamical patterns of groyne fields,* Earth Surface Processes and Landforms **27**, 289 (2002).

W. S. Uijttewaal, *Effects of groyne layout on the flow in groyne fields: Laboratory experiments,* Journal of Hydraulic Engineering **131**, 782 (2005).

M. F. M. Yossef and H. J. de Vriend, *Sediment Exchange between a River and Its Groyne Fields: Mobile-Bed Experiment,* Journal of Hydraulic Engineering **136**, 610 (2010).

M. Glas, K. Glock, M. Tritthart, M. Liedermann, and H. Habersack, *Hydrodynamic and morphodynamic sensitivity of a river's main channel to groyne geometry,* Journal of Hydraulic Research **56**, 714 (2018).

P. M. Biron, C. Robson, M. F. Lapointe, and S. J. Gaskin, *Three-dimensional flow dynamics around deflectors,* River Research and Applications **21**, 961 (2005).

J. Vanlede and A. Dujardin, *A geometric method to study water and sediment exchange in tidal harbors,* Ocean Dynamics **64**, 1631 (2014).

R. Pawlowicz, B. Beardsley, and S. Lentz, *Classical tidal harmonic analysis including error estimates in matlab using t_tide,* Computers & Geosciences **28**, 929 (2002).

K. Kuijper and L. C. Van Rijn, *Analytical and numerical analysis of tides and salinities in estuaries; Part II: Salinity distributions in prismatic and convergent tidal channels,* Ocean Dynamics **61**, 1743 (2011).

H. H. Savenije, *Salt intrusion model for high-water slack, low-water slack, and mean tide on spread sheet,* Journal of Hydrology **107**, 9 (1989).

H. H. Savenije, *Predictive model for salt intrusion in estuaries,* Journal of Hydrology **148**, 203 (1993).

D. C. Shaha, Y. K. Cho, M. T. Kwak, S. R. Kundu, and K. T. Jung, *Spatial variation of the longitudinal dispersion coefficient in an estuary,* Hydrology and Earth System Sciences **15**, 3679 (2011).

H. B. Fischer, E. J. List, R. C. Koh, J. Imberger, and N. H. Brooks, *Mixing in inland and coastal waters* (Academic press, 1979).

W. R. Geyer and R. P. Signell, *A Reassessment of the Role of Tidal Dispersion in Estuaries and Bays,* Estuaries **15**, 97 (1992).

W. R. Geyer, R. Chant, and R. Houghton, *Tidal and spring-neap variations in horizontal dispersion in a partially mixed estuary,* Journal of Geophysical Research **113**, C07023 (2008).

M. F. Yossef and H. J. de Vriend, *Flow details near river groynes: Experimental investigation,* Journal of Hydraulic Engineering **137**, 504 (2011).

R. T. Cheng, C.-H. Ling, J. W. Gartner, and P. F. Wang, *Estimates of bottom roughness length and bottom shear stress in South San Francisco Bay, California,* Journal of Geophysical Research: Oceans **104**, 7715 (1999).

R. Soulsby, *The Bottom Boundary Layer of Shelf Seas,* in *Physical Oceanography of Coastal and Shelf Seas*, Vol. 35, edited by B. Johns (Elsevier, Amsterdam, 1983) Chap. 5, pp. 189–266.

A

A R. L. Soulsby and K. R. Dyer, *The form of the near-bed velocity profile in a tidally accelerating flow,* Journal of Geophysical Research **86**, 8067 (1981).

Acknowledgements

My PhD trajectory not officially, but actually started on 10th, June 2015, the day that I received the first e-mail from Prof. Ding, my promotor. I was a bachelor student at that time, trying to find an opportunity to pursue a master degree. Then I first met Prof. Pingxing Ding at his office during the summer school held by SKLEC. I can hardly remember details of our talk, but Prof. Ding suggested that a direct PhD program which takes 5 years could also be a good option. I was irrationally interested in this idea and finally decided to do so as suggested. Importantly, Prof. Ding mentioned the collaboration with TuDelft during our first talk, as well as the dual degree program. I never thought it becomes such an important part of my past 6 years and finally comes true at this moment. I should thank Prof. Ding for his encouragement at the beginning. Since I began my PhD trajectory, I am quite often impressed by Prof. Ding's insightful opinion on research questions, he can always capture the core and essence of a question. Another unforgettable moment that I share with Prof. Ding is our last talk before I left for Delft. We had a very long talk, covering my research work, tips for living abroad, and expectations on me from a perspective broader than research work. Heartfelt thanks for giving me feelings of chatting with an amiable family member.

I have lots of wonderful experiences in Delft, of which having Prof. Zheng Bing Wang and Prof. D.S. van Maren as my promotors is the luckiest. Prof. Wang offers me a lot of help on both work and life in Delft. A sincere appreciation to Prof. Wang for his patient, effective supervision throughout my whole research, and constructive comments on my work. Prof. Wang shows me how can I grow into a real scholar from every aspect, especially the rigorous attitude towards science. Except for knowledge and the pursuit for high standard learned from Prof. Wang, I also received his warm encouragement when I am frustrated at some moments during my research. This is important for me to get through those setbacks and accomplish the thesis.

I want to express my gratitude to Prof. D.S. van Maren. Bas, you are always there when I have difficulties in research. When I was in TuDelft and there was no trouble of COVID 19, we met every week. During our meeting, you really taught me a lot. Many of these teaching-learning processes started from a question like 'By the way, do you know...?' After I came back to China, we discuss online. In the last year of the PhD trajectory I am quite anxious, and our weekly meeting has been my biggest hope every week for a long time. Many thanks.

Special thanks should be given to Prof. Jianzhong Ge. Dr. Ge, although you are not my official promotor but helps me no less than a promotor. I learn all my model skills from you and all data used in this thesis are collected by your support. Beyond that, we communicate everything in my research work. I appreciate your constructive comments on all of my manuscripts. I treasure the time we spend

A

together during field observations. Without your support, I cannot imagine how harder it would be to get to this moment.

I want to thank my family members. Thanks to my parents for their unconditional support for all my decisions. You two show many good qualities of a decent person. Moreover, you are the best example from who I can learn how to be a good parent in the future, although I never agree this in front of you. I kind of feel fortunate that you cannot read English. But I will tell you someday. Thanks to my wife and the only one who forces me to revise the acknowledgements, Zihan Wang, for her support for my pursuit of the doctoral degree. The distance between China and the Netherlands and living apart for two years have never weakened this support. During the past few years, your support, motivation, encouragement, and love are the most important things that I have.

I would like to thank my friends and colleagues in both Shanghai and Delft. Jianfei Ma, thanks for your help with my scripts, you are such a nice big brother and a talented programmer. Hualong Luan, you share lots of experience of research with me which is extremely important and really impacts me. Zhangliang Ding, we shared a room for two years, thanks for bearing me staying up late. I want to thank colleagues in my research team, Wenyun Guo, Fuhai Dao, Wanlun Yang, Weiqi Li, Jingting Zhang, Shenyang Shi, Jiayu Lu, Tianyang Yan, Jinxu Yi, Jingsi Zhang, Fucang Zhou, Xiangqian Zhou, Anqi Liu, Mengyuan Wu, we have a good time together. Thanks to all my friends in Delft. Yu Kuai, Jianwei Sun, we spent a lot of time together. Both of you are great cookers and good cookers never lack friends, thank you for making friends with me. I want to thank Chunyan Zhu, Jianliang Lin, Yuning Zhang, Rong Zhang, Yang Zhou, Sien Liu, Zhilin Zhang, Lian Liu, Runxiang Li, Yujian Zhan, and Dineng Zhao. You are great friends and we share enjoyable memories.

Zaiyang Zhou
Shanghai, July 2021

Curriculum Vitæ

Zaiyang ZHOU

29-04-1994   Born in Yangzhou, China.

Education

2012–2016   BS. Science in Port Channel and Coastal Engineering
Ocean University of China
Qingdao, China

2016–2021   PhD Student. Coastal Engineering (TUD) &
Estuarine and Coastal Science (ECNU)
Delft University of Technology, the Netherlands &
East China Normal University, China
Thesis: Lateral Flows and Sediment Dynamics in a Large
Engineered Estuary
Promotor: Prof.dr.ir. Zheng Bing Wang
Promotor: Prof.dr. Ping Xing Ding
Promotor: Prof.dr. D.S. van Maren

Awards

2020   Outstanding Student of East China Normal University
2019   National Scholarship for Doctoral Students, China
2018   The 15th China Post-Graduate Mathematical Contest in Modeling, Second Prize
2017   Excellent Student Cadre of East China Normal University

List of Publications

4. **Zhou, Z**., Ge, J., van Maren, D.S., Wang, Z.B., Kuai, Y., Ding, P. *Study of Sediment Transport in a Tidal Channel-Shoal System: Lateral Effects and Slack-Water Dynamics*, J. Geophys. Res. Ocean. **126**, (2021). (Chapter 3)

3. **Zhou, Z**., Ge, J., Wang, Z.B., van Maren, D.S., Ma, J., Ding, P. *Study of Lateral Flow in a Stratified Tidal Channel-Shoal System: The Importance of Intratidal Salinity Variation*, J. Geophys. Res. Ocean. **124**, 6702-6719 (2019). (Chapter 2)

2. Kuai, Y., Tao, J., **Zhou, Z**., Aarninkhof, S., Wang, Z.B. *Sediment Characteristics and Intertidal Beach Slopes along the Jiangsu Coast, China.*, J. Mar. Sci. Eng. **9**, 347 (2021).

1. Ge, J., **Zhou, Z**., Yang, W., Ding, P., Chen, C., Wang, Z.B., Gu, J. *Formation of Concentrated Benthic Suspension in a Time-Dependent Salt Wedge Estuary*, J. Geophys. Res. Ocean. **123**, 8581–8607 (2018).

Submitted and prepared:

2. **Zhou, Z**., Ge J., van Maren, D.S., Liu, X., Gu, J., Ding, P., Wang, Z.B. *A parameter space diagram for erosion and deposition of cohesive sediments*. (Chapter 4)

1. **Zhou, Z**., Ge J., van Maren, D.S., Kuai, Y., Ding, P., Wang, Z.B. *Groyne-Induced Effects on Channel-Shoal Exchange and Saltwater intrusion in Estuarine Environments*. (Chapter 5)